A Thesis Submitted for the Degree of PhD at the University of Warwick

Permanent WRAP URL:

http://wrap.warwick.ac.uk/108616

Copyright and reuse:

This thesis is made available online and is protected by original copyright.

Please scroll down to view the document itself.

Please refer to the repository record for this item for information to help you to cite it.

Our policy information is available from the repository home page.

For more information, please contact the WRAP Team at: wrap@warwick.ac.uk

COMPTON SCATTERING AND PHOTO-ABSORPTION STUDIES
OF CHARGE AND SPIN DENSITY

by

Abdelbaki BRAHMIA

A thesis submitted for the degree of

Doctor of Philosophy of the University of Warwick

Department of Physics

University of Warwick

April 1991

THE BRITISH LIBRARY DOCUMENT SUPPLY CENTRE

BRITISH THESES
N O T I C E

Dedicated to my wife Akila and my son Wassim

Abstract

Directional Compton profiles of zinc and $Fe_{0.25}Ni_{0.75}$ have been measured with 60 keV and 412 keV gamma-rays, and the results compared with the self consistent Korringe-Kohn-Rostoker Coherent-Potential Approximation (KKR-CPA) for the iron nickel alloy. The other investigations reported all involve the use of the synchrotron radiation; the polarisation of synchrotron radiation has been established for the SRS W9.4 line, for energies of the order of 50-65 keV, and good agreements with the theoretical calculations were obtained. The isotropic spin dependent Compton profile of gadolinium and directional spin dependent Compton profile of nickel have been measured for the first time using the inclined view method of extracting circular polarisation of synchrotron radiation. The existence of the spin dependent photoabsorption terms in the absorption coefficient have been established experimentally for iron and nickel, and compared with the first principles spin polarised band calculation.

MEMORANDUM

This thesis has been submitted to the University of Warwick in support of my application for the admission to the degree of Doctor of Philosophy. It contains an account of my own independent research except where acknowledged in the text. The work has been performed in the Department of Physics under the supervision of Prof. M. J. Cooper during the period from October 1986 to September 1989. Details of research to which I have contributed may be found in the following publications.

1-The magnetic Compton profiles of iron and cobalt, J. Phys. F18, L57, (1988).

2-Magnetic anisotropy in the electron momentum density of iron, Nature, 333, 151, (1988).

3-Spin dependent Compton profile of gadolinium, J. Phys.:Condens. Matter 1, 3879, (1988).

4-Majority- and minority-spin-band directional Compton profiles in iron, J. Phys.: Condens. Matter 1. 9009, (1989).

5-Magnetic near-edge structure in iron. J. Phys.: Condens. Matter 1, 323, (1989).

6-Spin dependent anisotropy in the momentum density of ferromagnetic nickel metal, J. Phys.: condens. Matter 2, 3427, (1990).

7-Gamma-ray Compton profile of iron nickel alloy. to be published.

ACKNOWLEDGMENTS

Units

The system of units adopted in this work is that of "atomic units" i.e. $\hbar = 1$, $m = 1$ and $c = 137.036$. The atomic units have the following relation to SI units;

$$1 a.u. momentum = \frac{mc}{137.036} = 1.9929 \times 10^{-24} kgms^{-1}$$

$$1 a.u. energy = \frac{mc^2}{137.036} = 4.3598 \times 10^{-18} J$$

$$1 a.u. length = \frac{137.036}{mc} = 2.2918 \times 10^{-11} m$$

Chapter 1

COMPTON SCATTERING AND
PHOTON SCATTERING THEORY

1.1 Compton Profile

The ground-state linear momentum distribution of electrons in solids can be investigated, under the fundamental assumption called the impulse approximation (IA), by determining the Compton profile.

The Compton profile, $J(p_z)$, is defined by integrating the three-dimensional electron momentum density, $n(\mathbf{p})$, over a plane perpendicular to the scattering vector ($\mathbf{K} = \mathbf{k} - \mathbf{k}'$) chosen as the z-axis, i.e.

$$J(p_z) = \int\int_{p_x \, p_y} n(\mathbf{p}) dp_x dp_y \tag{1.1}$$

where $\mathbf{k}$ and $\mathbf{k}'$ are respectively the incoming and the outgoing photon wavevectors and p_x, p_y and p_z are the momentum components. For isotropic systems (gases, liquids, glasses, powders etc...), i.e. for a spherically symmetric momentum density, the Compton profile formula may be written as,

$$J(q) = \frac{1}{2} \int_{|q|}^{\infty} \frac{I(\mathbf{p})}{p} d\mathbf{p} \tag{1.2}$$

1

where $I(\mathbf{p}) = 4\pi p^2 \chi^2(\mathbf{p})$ and $\chi(\mathbf{p})$ is the electron wavefunction in the momentum representation.

1.2 Momentum space representation and momentum density

It is well known that the Schroedinger equation in position space can be solved to give the wave function, $\psi(\mathbf{r})$, and hence the charge density, $\rho(\mathbf{r})$. In principle the same equation is solvable in the momentum space to yield electron momentum wavefunction, $\chi(\mathbf{p})$, and hence the electron momentum density, $n(\mathbf{p}) = \sum_i |\chi_i(\mathbf{p})|^2$,

$$(\frac{p^2}{2m} - 2E)\chi(\mathbf{p}) + V(\mathbf{p})\chi(\mathbf{p}) = 0. \tag{1.3}$$

Because the potential energy term present in the momentum space equation is an integral, it is not possible to obtain the electron momentum wavefunction by solving the Schroedinger equation in momentum space,

$$(\frac{p^2}{2m} - 2E)\chi(\mathbf{p}) = \frac{n}{\pi^2} \int \frac{\chi(\mathbf{p}')}{|\mathbf{p} - \mathbf{p}'|^2} d\mathbf{p}'. \tag{1.4}$$

where n is the total number of electrons in the atom.

Apart from simple systems such as the hydrogen atom (solved by Fock 1935), helium and the hydrogen molecular ions solved by McWeeny and Coulson (1949), it is practically impossible to solve complex integral equations. Dirac (1926) pointed out the Fourier transform relationship between $\psi(\mathbf{r})$ and $\chi(\mathbf{p})$ and suggested that it could be used to obtain the latter from the former,

$$\chi(\mathbf{p}) = \left(\frac{1}{hbar}\right)^{3/2} \int \psi(\mathbf{r})e^{(-i\frac{\mathbf{p.r}}{\hbar})}d\mathbf{r}. \tag{1.5}$$

The wavefunction in position space may be separated into R_{nl} and Y_{lm} respectively the radial and the angular parts: Y_{lm} is unchanged by Fourier transformation, i.e. only the radial part needs to be transformed. Dirac transforms were calculated for hydrogenic and Slater type orbitals by Podolsky and Pauling (1929).

1.3 Historical developments of Compton scattering

In 1923 the inelastic photon scattering by a stationary electron, subsequently known as the Compton effect, was discovered by Compton (1923). The broader inelastic line recorded in the spectrum was a mystery at that time and for the next six years until DuMond (1929) pointed out that the scattered photon is Doppler shifted by the momentum of the scattering electron. DuMond and Kirkpatrick (1937) built a focusing multi-crystal spectrometer and measured the momentum distribution of many light elements. Apart from a few subsequent attempts to study Compton scattering (Ross et al 1934 and Kappler 1936) and the theoretical work of Coulson and Duncanson (1941,1942) who showed how the Compton profile could be calculated from the LCAO wavefunctions in C-H, C-C, C=C and C≡C bonds, there followed a long period of inactivity when inelastic scattering was largely overshadowed by the attractions of X-ray diffraction.

The next phase of the Compton scattering era dates from the mid 60's into the 1980s. Cooper et al (1965) were the first to try to analyse the scattered radiation using an X-ray tube and crystal spectrometer. The results of those early days were statistically very poor especially in the tails of the profile mainly because of the high background radiation and low count rates.

As the time went on the technique of Compton scattering was markedly improved by using high energy sources and solid state detectors (see Eisenberger and Reed 1972). The change from the use of low energy X-ray sources ($E_X < 20 keV$) to high energy gamma rays, such as ^{198}Au and ^{241}Am isotopes which provide respectively monochromatic radiation of 412 keV and 59.54 keV, had an important impact on the significant improvement of the statistical accuracy of the data. Furthermore, high energies also overcame the problem of large photo-electric absorption usually obtained even for solids of low atomic number. In the early 1970s the use of gamma rays was made possible in conjunction with high resolution solid state detectors, albeit at the better resolution of the crystal monochromators. Such a technique lead, in short measuring times, to a high statistical precision of the data. A better understanding of the different corrections such as multiple scattering also contributed significantly to a more accurate result.

In the last couple of decades a comprehensive study of the theoretical aspect of this spectroscopy has been well established. As far as the magnetic scattering is concerned (discussed in detail later), Platzman and Tzoar (1965,1970) were the first to point out the way of separating the charge scattering from the magnetic scattering in ferromagnets. Blume (1985), then Lovesey (1988) provided detailed theoretical work investigating the photon scattering cross section involving charge, spin and orbital magnetic contributions.

A well established method for the study of spin dependent Compton scattering was introduced in the late 70s, initially by Cooper et al (1976) and Holt et al (1978), using Circularly Polarised synchrotron radiation (CPSR). The main objective of using circularly polarised radiation is to study the spin density as well as the orbital

contributions to the Compton profile.

1.4 Impulse approximation

The method of obtaining the Compton profile by means of the photon scattering cross section in the relativistic limit is very complex due to the restrictions of the impulse approximation. The impulse approximation is governed by the fact that the probe (i.e. photon) interacts with an individual electron at a time. In other words the remaining electrons do not react completely to the interaction until the scattered photon has escaped completely from the system. Therefore, the potential of the system before and after the scattering process is the same. Principally this condition may be satisfied only when the energy transfer greatly exceeds the electron binding energy. Clearly, this restrictive condition implies that large backscattering angles (i.e. angles close to 180°) and high photon energies are necessary. Furthermore, the impulse approximation is complementary valid when the binding forces between the ejected electron and the other electrons in the system remain constant within the interaction time ($\sim \frac{\hbar}{\Delta\omega}$), i.e. the energy of the recoil electron must largely exceed its energy before the collision.

Although the failure of the impulse approximation mainly occurs at energies which correspond to core states, particularly when high energy gamma rays are used, the study of the electron momentum density distribution may still be possible with the Compton technique since the Compton profile is a sensitive probe of valence electrons.

1.5 The interaction between photons and matter

The interaction of photon with matter is a basic process for probing important information about the microscopic behaviour of materials. The photon-electron interaction is characterised by two important physical quantities (ω) and $(\hbar K)$ defined respectively as the energy transfer and the momentum transfer, and can result in absorption and emission processes, pair production, and X-ray elastic and inelastic scattering. A schematic diagram of the photon scattering process is illustrated in figure 1.1.

The most common inelastic scattering process is Compton scattering which provides information on the momentum distribution of electrons in the ground state. Raman scattering is another common inelastic process which provides information on the behaviour of collective such as relatively high energy excitations like plasmons and individual excitations of inner core electrons. Raman scattering is a very small effect which gets important only when the energy of the incident radiation approaches the energy of the absorption threshold (see Eisenberger et al 1976). In other words, the incident energy is of the same order as the absorbed energy during the transition of the electron from its initial state to an intermediate state which correspond to those where a K-electron is excited virtually above the Fermi level (see Manninen et al 1986).

1.5.1 Elastic scattering and the Thomson mechanism

The elastic scattering between photons and electrons, which gives rise to the well known Bragg reflection in solids, is basically used to study crystal structure and
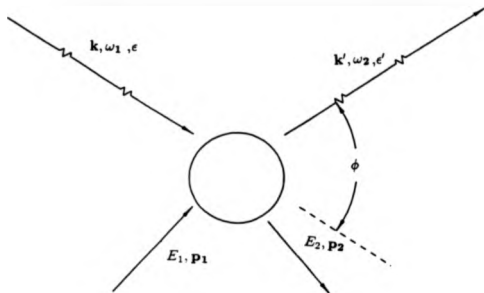
Figure 1.1 Schematic diagram of the Compton scattering interaction between a photon and a free electron of a momentum p_1 and an energy E_1. The incoming photon is characterized by the energy $\hbar\omega_1$, the wavevector $\mathbf{k}$ and the unit polarisation ϵ. The scattered photon is featured by the energy $\hbar\omega_2$, the wavevector $\mathbf{k}'$ and the unit polarisation ϵ'. The recoil electron has a momentum p_2 and an energy E_2.

electron density. It is distinguished by a cross section which is a function only of the momentum transfer. It is well described by the classical Thomson cross section,

$$\left(\frac{d\sigma}{d\omega}\right)_{Th} = \left(\frac{e^2}{mc^2}\right)^2 (\epsilon'.\epsilon) \tag{1.6}$$

where $\left(\frac{e^2}{mc^2}\right)$ is the classical electron radius and ϵ and ϵ' are the polarisation vectors of the incident and the scattered beam respectively. In the case of unpolarised photons, equation 1.6 becomes,

$$\left(\frac{d\sigma}{d\omega}\right)_{Th} = \frac{1}{2} \left(\frac{e^2}{mc^2}\right)^2 (1 + \cos^2 \phi) \tag{1.7}$$

where ϕ is the scattering angle (see figure 1.1).

1.5.2 The Compton effect

The inelastic scattering effect is well established and well described by the familiar equation,

$$\lambda_1 - \lambda_2 = \frac{h}{mc}(1 - \cos \phi) \tag{1.8}$$

This formula is much more useful. as far as the Compton scattering studies reported in this thesis are concerned. when it is written in terms of incident and scattered energies ω_1 and ω_2,

$$\omega_2 = \omega_1 \left[1 + \frac{\omega_1}{mc^2}(1 - \cos \phi)\right]^{-1} \tag{1.9}$$

It is obvious that the Compton effect formula is very sensitive to the scattering angle which determines the energy transfer to the recoil electron.

1.5.3 Compton scattering from a free electron

The derivation of the inelastic scattering cross section from free stationary electrons was derived by Klein and Nishina (1929) using quantum electrodynamics. For un-

polarised photon scattering from free electrons without net spin, the cross section is given by,

$$\left(\frac{d\sigma}{d\omega}\right)_{K-N} = \frac{1}{2}\left(\frac{e^2}{mc^2}\right)^2 \left(\frac{\omega_2}{\omega_1}\right)^2 \left(\frac{\omega_2}{\omega_1} + \frac{\omega_1}{\omega_2} - \sin^2\phi\right) \tag{1.10}$$

where ω_1 and ω_2 are the incident and the scattered energies related to the Compton shift formula (see equation 1.9). For a low incident energy photon ($\omega_1 << m_0c^2$), where the energy transfer is very small ($\omega_1 \sim \omega_2$), the Klein-Nishina cross section reduces to the Thomson cross section (equation 1.7).

1.5.4 Compton scattering from a bound electron

In the early section (1.5.3) the scattering from a free non-relativistic electron was discussed. However, those assumptions are not valid as far as the condensed matter is concerned. It is well known that inner electrons in atoms may be tightly bound and most electrons move with relativistic velocities. Moreover, the outer-most electrons in outer shells may reach speeds approaching relativistic values. The motion of bound electrons in condensed matter with such high velocities contributes markedly in the expansion of Doppler broadening of the Compton scattered beam, i.e. the scattered photon energy is shifted from the usual value obtained from equation 1.9. This is due to the fact that photons are scattered off relativistically moving electrons. A schematic diagram of the interaction process between a photon and a non-relativistically moving free electron is shown in figure 1.2.

For a non-relativistic target electron with momentum **p**, the energy transfer is given by

$$\omega = \omega_1 - \omega_2 = \frac{1}{2m}\left[\mathbf{p} + \hbar(\mathbf{k} - \mathbf{k}')\right]^2 - \frac{p^2}{2m}$$
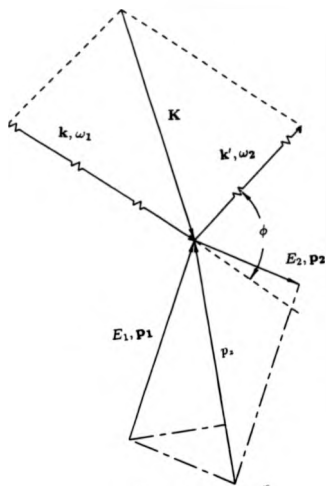
Figure 1.2 Schematic diagram of the kinematics of a photon with an energy $\hbar\omega$ and a wavevector $\mathbf{k}'$ interacting with a free electron with an initial momentum p_1 and an energy E_1. The electron momentum p_s is aligned with the scattering vector $\mathbf{K} = \mathbf{k} - \mathbf{k}'$.

$$= \frac{\hbar^2 |\mathbf{K}|^2}{2m} + \hbar \frac{\mathbf{K}.\mathbf{p}}{m} \tag{1.11}$$

In contrast with equation 1.9, the energy transfer here contains a second term ($\hbar \frac{\mathbf{K}.\mathbf{p}}{m}$) which is linearly dependent upon the momentum of the electron. Assuming that the scattering vector is arbitrarily chosen to be along the z-axis, equation 1.9 becomes

$$p_z = \frac{\omega_1{}^2 - \omega_2{}^2 + \omega_1 \omega_2 (1 - cos\phi)}{(\omega_1^2 + \omega_2^2 - 2\omega_1\omega_2 cos\phi)^{1/2}} \tag{1.12}$$

where p_z is the component of the electron momentum along the scattering vector.

1.6 Photon scattering theory

In this section a detailed derivation of the photon scattering from bound electrons will be presented using relativistic corrections in a non-relativistic time dependent perturbation theory, following Bhatt et al (1983), Gell-mann and Golderberger (1954), Blume (1985) and Lovesey (1988).

1.6.1 The Hamiltonian for an electron in a quantized electromagnetic field.

The non-relativistic Hamiltonian for an electron system in a quantized electromagnetic field is given as,

$$\begin{aligned}
H &= \sum_j \frac{1}{2m} \left[\mathbf{p}_j - \frac{e}{c} \mathbf{A}(\mathbf{r}_j) \right]^2 + \sum_{i,j} V(\mathbf{r}_{ij}) - \frac{e\hbar}{2mc} \sum_j \mathbf{s}_j.\mathbf{B} \\
&\quad - \frac{e\hbar}{2mc} \sum_j \mathbf{s}_j.\mathbf{B}' + \sum_{k,\lambda} \hbar\omega_k \left[C^+(k\lambda)C(k\lambda) + \frac{1}{2} \right]
\end{aligned} \tag{1.13}$$

where $\mathbf{B}$ is the magnetic field of the electromagnetic radiation

$$\mathbf{B} = \nabla \times \mathbf{A}, \tag{1.14}$$

and $\mathbf{B}'$ is the magnetic field created by the moving electron in the electric field of the electromagnetic radiation $\mathbf{E}(\mathbf{r}_j)$,

$$\mathbf{B}' = \frac{1}{mc}\left[\mathbf{p}_j - \frac{e}{c}\mathbf{A}(\mathbf{r}_j)\right] \times \mathbf{E}(\mathbf{r}_j). \tag{1.15}$$

Since the system is treated in the non-relativistic approximation, the Coulomb interaction of the nucleus with each electron existing in the system and the Hamiltonian describing the nucleus in the presence of the electromagnetic radiation are not considered (Grotch et al 1983). This approximation is based on the assumption that the nucleus is treated as infinitely heavy.

The vector potential $\mathbf{A}(\mathbf{r}_j)$ is a linear combination of photon creation and photon annihilation operators respectively $C^+(k\lambda)$ and $C(k\lambda)$,

$$\mathbf{A} = \left(\frac{2\pi\hbar c^2}{V}\right)^{1/2} \sum_{\sigma,q} \frac{1}{\sqrt{\omega_q}} \left[\epsilon_{q\sigma} C_{q\sigma} e^{i(\mathbf{qr}-\omega_q t)} + \epsilon^*_{q\sigma} C^+_{q\sigma} e^{-i(\mathbf{qr}-\omega_q t)}\right] \tag{1.16}$$

where V is the quantized volume principally used for the normalisation. The index $\sigma = (1,2)$ labels the two polarisations of each wave $\mathbf{q}$, i.e. $\mathbf{k}$ and $\mathbf{k}'$.

The electric field in the spin-orbit term is not derived from a static potential, hence it is given by,

$$\mathbf{E} = -\nabla\Phi - \frac{1}{c}\dot{\mathbf{A}}. \tag{1.17}$$

where Φ is the Coulomb potential.

Since the scattering occurs in second order for terms linear in $\mathbf{A}$ and in first order for terms quadratic in $\mathbf{A}$, hence, the spin-orbit term, which is of the order of $\sim (v/c)^2$ is going to be simplified in such a way that the linear terms in $\mathbf{A}$, which become negligible, will be omitted. The quadratic terms as well as those independent of $\mathbf{A}$

were kept in the Hamiltonian (Blume 1985).

$$- \frac{e\hbar}{2(mc)^2} \sum_j \mathbf{s}_j . \mathbf{E}(\mathbf{r}_j) \times \left[\mathbf{p}_j - \frac{e}{c} \mathbf{A}(\mathbf{r}_j) \right] \tag{1.18}$$

$$\Rightarrow - \underbrace{\frac{e\hbar}{2(mc)^2} \left(\sum_j \mathbf{s}_j . (-\nabla\Phi_j \times \mathbf{p}_j)}_{H_1} + \underbrace{\frac{e}{c^2} \sum_j \mathbf{s}_j . \left[\dot{\mathbf{A}}(\mathbf{r}_j) \times \mathbf{A}(\mathbf{r}_j) \right] \right)}_{H_2} \tag{1.19}$$

where the first part, H_1, is the ordinary spin-orbit coupling term for electrons, while the second one, H_2, represents the spin dependent scattering. The resulting expression of the Hamiltonian may be written as.

$$H = H_0 + H' \tag{1.20}$$

where H_0 is the Hamiltonian for the uncoupled photon.

$$\begin{aligned} H_0 &= \sum_j \frac{1}{2m} \mathbf{p}_j^2 + \sum_{i,j} V(\mathbf{r}_{ij}) + \frac{e\hbar}{2(mc)^2} \sum_j \mathbf{s}_j . (\nabla\Phi \times \mathbf{p}_j) \\ &\quad + \sum_{k,\lambda} \hbar\omega_k \left[C^+(k\lambda) C(k\lambda) + \frac{1}{2} \right] \end{aligned} \tag{1.21}$$

and H' is the Hamiltonian for the electron-photon interaction,

$$\begin{aligned} H' &= \underbrace{\frac{e^2}{2mc^2} \sum_j \mathbf{A}^2(\mathbf{r}_j)}_{H'_1} - \underbrace{\frac{e}{mc} \sum_j \mathbf{A}(\mathbf{r}_j) . \mathbf{p}_j}_{H'_2} \\ &\quad - \underbrace{\frac{e\hbar}{mc} \sum_j \mathbf{s}_j . \nabla \times \mathbf{A}(\mathbf{r}_j)}_{H'_3} \\ &\quad - \underbrace{\frac{e\hbar}{2(mc)^2} \frac{e}{c^2} \sum_j \mathbf{s}_j . [\dot{\mathbf{A}}(\mathbf{r}_j) \times \mathbf{A}(\mathbf{r}_j)]}_{H'_4} \end{aligned} \tag{1.22}$$

The scattering events originating from the first two terms, i.e. $\mathbf{A}^2$ and $\mathbf{A}.\mathbf{p}$, are schematically shown in figure 1.3.
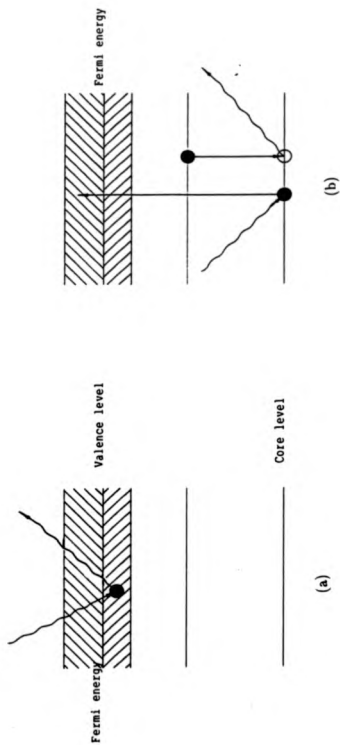
Figure 1.3 Schematic diagram of X-ray scattering; (a) from the A^2 term and (b) from the p·A term.

1.6.2   The Relativistic photon scattering cross section

The derivation of the Compton scattering cross section is governed by the transition rate known otherwise as Fermi's golden rule (equation 5.12) to second order, which describes the photon scattering process as a transition from one state to another,

$$W = \frac{2\pi}{\hbar} \left| < \beta|H'|\alpha > + \sum_\gamma \frac{< \beta|H'|\gamma > < \gamma|H'|\alpha >}{E_\alpha - E_\gamma} \right|^2 \times \delta(E_\alpha - E_\beta), \quad (1.23)$$

where the initial state $|\alpha >$ consists of a bound polarised electron and a single photon characterised by its wavevector $\mathbf{k}$ and a polarisation ϵ. The scattered photon which governed the final state $|\beta >$ is described by a wavevector $\mathbf{k}'$ and a polarisation ϵ'.

Clearly from equation 1.22, only H'_1 and H'_4 will contribute to first order terms in the Golden rule because of their quadratic vector potential dependence. On the other hand H'_2 and H'_3, which are linearly dependent on $\mathbf{A}$ will only contribute to second order terms.

Assuming that only the low lying excitations are considered (which means $\omega_k \sim \omega_{k'}$) and neglecting the relativistic corrections in the denominators, hence, after substituting the expressions of H'_1 and H'_4 in the first order term in equation 1.23, one may obtain,

$$\begin{aligned}
< \beta|H'_1 + H'_4|\alpha > = \frac{2\pi\hbar c^2}{V\omega} \frac{e^2}{mc^2} \times \Bigg(& < \beta|\sum_j e^{i\mathbf{K}.\mathbf{r}_j}|\alpha > \epsilon'.\epsilon \\
& -i\frac{\hbar\omega}{mc^2} < \beta|\sum_j e^{i\mathbf{K}.\mathbf{r}_j}\mathbf{s}_j|\alpha > \epsilon' \times \epsilon \Bigg)
\end{aligned} \quad (1.24)$$

where $\epsilon \equiv \epsilon(\mathbf{k}\lambda)$, $\epsilon' \equiv \epsilon^*(\mathbf{k}'\lambda')$ and $\mathbf{K} = \mathbf{k} - \mathbf{k}'$.

The first term in equation 1.24 originates from the $\mathbf{A}^2$ term and it is commonly known as the Thomson term for non relativistic electrons. The general expression of photon scattering including all terms up to second order may be obtained by

substituting terms linearly dependent on **A** in the second part of equation 1.23 as well (this additional contribution is particularly important at high energy). In doing so, one may obtain the total differential cross section up to second order by multiplying the transition probability, W, by the density of the final states and dividing by the incident flux (see Bhatt et al 1983),

$$\frac{d^2\sigma}{d\Omega d\omega} = W\rho(\omega_f)/I_0, \tag{1.25}$$

where $\rho(\omega_f) = \frac{V}{(2\pi)^3} \cdot \frac{\omega_f^2}{\hbar c^3}$ and $I_0 = \frac{c}{V}$.

Therefore,

$$\frac{d^2\sigma}{d\Omega d\omega} = \left(\frac{e^2}{mc^2}\right)^2 \left| < \beta| \sum_j e^{i\mathbf{K}.\mathbf{r}_j}|\alpha > \epsilon'.\epsilon - i\frac{\hbar\omega}{mc^2} < \beta| \sum_j e^{i\mathbf{K}.\mathbf{r}_j}.\mathbf{s}_j|\alpha > \epsilon' \times \epsilon + \frac{\hbar^4}{m}\sum_\gamma \sum_{i,j} \right.$$

$$\left(\frac{< \beta|[\frac{\epsilon'.\mathbf{p}_i}{\hbar} - i(\mathbf{k}' \times \epsilon').\mathbf{s}_i]e^{-i\mathbf{k}'.\mathbf{r}_i}|\gamma > < \gamma|[\frac{\epsilon.\mathbf{p}_j}{\hbar} + i(\mathbf{k} \times \epsilon).\mathbf{s}_j]e^{i\mathbf{k}.\mathbf{r}_j}|\alpha >}{E_\alpha - E_\gamma + \hbar\omega_k - i\Gamma_\gamma/2}\right.$$

$$\left.\left. + \frac{< \beta|[\frac{\epsilon.\mathbf{p}_i}{\hbar} + i(\mathbf{k} \times \epsilon).\mathbf{s}_j]e^{i\mathbf{k}.\mathbf{r}_j}|\gamma > < \gamma|[\frac{\epsilon'.\mathbf{p}_i}{\hbar} - i(\mathbf{k}' \times \epsilon').\mathbf{s}_j]e^{-i\mathbf{k}'.\mathbf{r}_i}|\alpha >}{E_\alpha - E_\gamma - \hbar\omega_{k'}}\right)\right|^2$$

$$\delta(E_\alpha - E_\beta + \hbar\omega_k - \hbar\omega_{k'}). \tag{1.26}$$

This resulting expression of the double differential cross section accounts for most X-ray scattering phenomena up to second order $(\frac{\hbar\omega}{mc^2})^2$. The term $-i\Gamma_\gamma/2$ which appears in the denominator is included in order to take into consideration the level width which is markedly important very close to resonance $(\hbar\omega_k \sim E_\alpha - E_\gamma)$ where anomalous dispersion effects occur. The derivation of the cross section which is going to be assumed here, applies only to the condition $\omega_k \sim \omega_{k'} \gg \frac{E_\alpha - E_\gamma}{\hbar}$. Hence, using the closure relation $\sum_\gamma |\gamma > < \gamma| = 1$, the final expression of the scattering cross section may be reduced to,

$$\frac{d^2\sigma}{d\Omega d\omega} = \left(\frac{e^2}{mc^2}\right)^2 \left| < \beta| \sum_j e^{i\mathbf{K}.\mathbf{r}_j}|\alpha > \epsilon'.\epsilon - i\frac{\hbar\omega}{mc^2}\left(< \beta| \sum_j e^{i\mathbf{K}.\mathbf{r}_j}.\mathbf{s}_j|\alpha > \epsilon' \times \epsilon \right.\right.$$

$$+ \frac{\hbar^2}{m} \frac{1}{\hbar\omega} \sum_{i,j} < \beta \left| \left[\frac{\epsilon'.\mathbf{p}_i}{\hbar} - i(\mathbf{k}' \times \epsilon').\mathbf{s}_i \right] e^{i\mathbf{k}'.\mathbf{r}_i} \left[\frac{\epsilon.\mathbf{p}_j}{\hbar} + i(\mathbf{k} \times \epsilon).\mathbf{s}_j \right] e^{i\mathbf{k}.\mathbf{r}_j} | \alpha > \right|^2$$

$$\delta(E_\alpha - E_\beta + \hbar\omega_k - \hbar\omega_{k'}).$$ (1.27)

Finally the photon scattering cross section may be deduced after evaluating the commutators in the last two terms of equation 1.27,

$$\frac{d^2\sigma}{d\Omega d\omega} = \left(\frac{e^2}{mc^2} \right)^2 \left| < \beta \left| \sum_j e^{i\mathbf{K}.\mathbf{r}_j} | \alpha > \epsilon'.\epsilon \right. \right.$$
$$\left. -i \frac{\hbar\omega}{mc^2} \left(< \beta \left| \sum_j e^{i\mathbf{K}.\mathbf{r}_j} \left[i \frac{\mathbf{K} \times \mathbf{p}_j}{\hbar k^2} \mathbf{C} + \mathbf{s}_j.\mathbf{B}_1 \right] | \alpha > \right) \right|^2$$
$$\delta(E_\alpha - E_\beta + \hbar\omega_k - \hbar\omega_{k'}).$$ (1.28)

where,

$$\epsilon'.\epsilon = \begin{pmatrix} 1 & 0 \\ 0 & \hat{\mathbf{k}}.\hat{\mathbf{k}}' \end{pmatrix}$$ (1.29)

$$\mathbf{C} = \epsilon' \times \epsilon = \begin{pmatrix} 0 & \hat{\mathbf{k}} \\ -\hat{\mathbf{k}}' & \hat{\mathbf{k}}' \times \hat{\mathbf{k}} \end{pmatrix}$$ (1.30)

and

$$\mathbf{B}_1 = \epsilon' \times \epsilon + (\hat{\mathbf{k}}'.\epsilon)(\hat{\mathbf{k}}' \times \epsilon') - (\hat{\mathbf{k}}' \times \epsilon)(\hat{\mathbf{k}}.\epsilon') - (\hat{\mathbf{k}}' \times \epsilon)') \times (\hat{\mathbf{k}} \times \epsilon)$$
$$= \begin{pmatrix} \hat{\mathbf{k}} \times \hat{\mathbf{k}}' & -2\hat{\mathbf{k}}' \sin^2 o/2 \\ 2\hat{\mathbf{k}} \sin^2 \phi/2 & \hat{\mathbf{k}} \times \hat{\mathbf{k}}' \end{pmatrix}$$ (1.31)

By summing all final states, the differential cross section equation may be written explicitly in terms of the three quantities $n(\mathbf{K})$, $\mathbf{S}(\mathbf{K})$ and $\mathbf{L}(\mathbf{K})$ respectively known as the Fourier transform of the charge density, the spin density and the atomic orbital magnetisation density (Blume et al 1988),

$$\frac{d^2\sigma}{d\Omega d\omega} = \left(\frac{e^2}{mc^2} \right)^2 \left| n(\mathbf{K})\epsilon'.\epsilon - i \frac{\hbar\omega}{mc^2} \left[\frac{1}{2}\mathbf{L}(\mathbf{K})\mathbf{A}_1 + \mathbf{S}(\mathbf{K}).\mathbf{B}_1 \right] \right|^2$$ (1.32)

where,

$$\mathbf{n}(\mathbf{K}) = <\alpha| \sum_{j} e^{i\mathbf{K}\cdot\mathbf{r}_j}|\alpha> \tag{1.33}$$

$$\mathbf{S}(\mathbf{K}) = <\alpha| \sum_{j} e^{i\mathbf{K}\cdot\mathbf{r}_j}\mathbf{s}_j|\alpha>, \tag{1.34}$$

$$\frac{1}{2}\hat{\mathbf{K}} \times (\mathbf{L}(\mathbf{K} \times \hat{\mathbf{K}}) = <\alpha| \sum j e^{i\mathbf{K}\cdot\mathbf{r}_j} \left(\frac{i\mathbf{K} \times \mathbf{P}_j}{K} \right) |\alpha>, \tag{1.35}$$

and $\mathbf{A_1}$ is a 2×2 matrix given as:

$$\begin{aligned}
\mathbf{A_1} &= 2(1 - \hat{\mathbf{k}}\hat{\mathbf{k}}')(\hat{\epsilon}' \times \hat{\epsilon}) - (\hat{\mathbf{k}} \times \hat{\epsilon})(\hat{\mathbf{k}}.\hat{\epsilon}') + (\hat{\mathbf{k}}' \times \hat{\epsilon}')(\hat{\mathbf{k}}'.\hat{\epsilon}) \\
&= \frac{K^2}{2k^2} \begin{pmatrix} 0 & -(\hat{\mathbf{k}} + \hat{\mathbf{k}}') \\ \hat{\mathbf{k}} + \hat{\mathbf{k}}' & 2\hat{\mathbf{k}} \times \hat{\mathbf{k}}' \end{pmatrix}
\end{aligned} \tag{1.36}$$

For further detailed derivation about the atomic orbital magnetisation, the reader is referred to Trammel (1953) and Steinsvoll et al (1967).

Clearly, from equation 1.32 the ratio of the cross section for pure magnetic photon scattering to the charge density scattering is reduced by a factor of $(\frac{\hbar\omega}{mc^2})^2$, i.e. for 60 keV photon energy, the ratio is reduced by a factor of the order of 10^{-2} regardless of the reduction due to the very small magnetic effect usually obtained in magnetic substances. On the other hand the interference scattering cross section is of the order of $(\frac{\hbar\omega}{mc^2})$ i.e. for conventional X-rays the magnetic effect may be experimentally obtained to be around 1% in ferromagnet transition metals. More precisely this effect may only be investigated when circularly polarised radiation is used (complex polarisation vectors).

1.6.3 Polarisation states and the density matrix

The polarisation states for partially polarised photon radiation may be described by the density matrix formalism. For polarised photon beams such as synchrotron

radiation, the polarisation is described by two polarisation states known as the right -hand and the left-hand circular polarisation, $\epsilon^{\pm}$ (see section 3.2.4). In the incident beam coordinates $(\xi \, \eta \, \zeta)$ shown in figure 1.4, with the ζ axis represents the direction of the wavevector $\mathbf{k}$, we have,

$$\epsilon^{\pm} = \frac{1}{\sqrt{2}}(\epsilon_{\eta} \pm i\epsilon_{\xi}). \tag{1.37}$$

The polarisation, P, of the incident beam may be described by Stokes parameters $P_{\xi}, P_{\eta}, P_{\zeta}$ respectively referred to as the 45° linear polarisation, the circular polarisation and finally the linear polarisation (see Blume et al 1988, Lovesey 1988). The expression for the density matrix may be expressed in terms of the unit matrix and the Pauli matrices,

$$\rho = (\mathbf{I} + \mathbf{P}.\sigma) = \begin{pmatrix} 1 + P_{\zeta} & P_{\xi} - iP_{\eta} \\ P_{\xi} + iP_{\eta} & 1 - P_{\zeta} \end{pmatrix} \tag{1.38}$$

where,

$$\sigma_{\xi} = \begin{pmatrix} 0 & 1 \\ 1 & 0 \end{pmatrix}, \sigma_{\eta} = \begin{pmatrix} 0 & -i \\ i & 0 \end{pmatrix}, \sigma_{\zeta} = \begin{pmatrix} 1 & 0 \\ 0 & -1 \end{pmatrix}. \tag{1.39}$$

Hence, the photon scattering cross section may be emphasized by means of the density matrix as follow,

$$\frac{d^2\sigma}{d\Omega d\omega} = \left(\frac{e^2}{mc^2}\right)^2 tr(< M_i > \rho < M_i >^+) \tag{1.40}$$

where $< M_i >$ is the matrix element which represents the amplitude of the photon scattering cross section, and the i indicates the type of the amplitude, i.e. c for charge and m for magnetic.
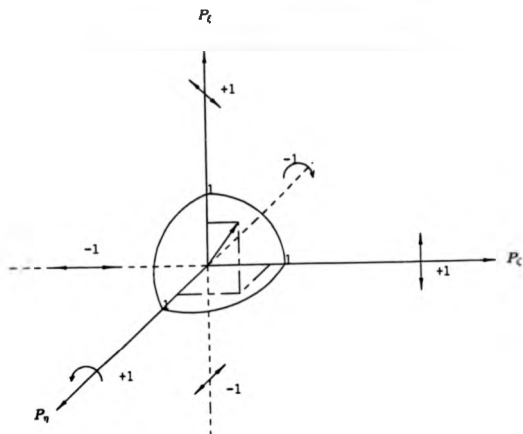
Figure 1.4 Arbitrary Incident polarisation $P = (P_x, P_\eta, P_\zeta)$ in the Poincarré representation.

1.6.4   The charge scattering cross section

As it has been discussed earlier the charge scattering cross section is simply obtained from equation 1.32 by assuming $S(K)$ and $L(K)$ to be zero. the same result may be obtained straightforwardly from equation 1.40. i.e.

$$
\begin{aligned}
\frac{d^2\sigma}{d\Omega d\omega} &= \left(\frac{e^2}{mc^2}\right)^2 tr(< M_c > \rho < M_c >^+) \\
&= \frac{1}{2}\left(\frac{e^2}{mc^2}\right)^2 |\mathbf{n}(\mathbf{K})|^2 \left[(1+\cos^2\phi) + P_\zeta \sin^2\phi\right]
\end{aligned} \tag{1.41}
$$

Clearly the charge scattering cross section is dependent only on the linear component of the incident polarisation. The dominance of the cross section is characterised by photons which are polarised perpendicular to the scattering plane ($P_\zeta = 1$). Whereas for photons polarised in the scattering plane ($P_\zeta = -1$, the cross section is less significant. Ultimately, the Thomson cross section is obtained for unpolarised incident photons (i.e. $P = 0$).

1.6.5   The interference scattering cross section

The existence of magnetic terms in the general expression of the scattering cross section (equation 1.32) is well established. As far as Compton scattering is concerned, the interference term is significantly larger than the purely magnetic term for conventional photon energies (see equation 1.32). The isolation of the interference term is achieved with circularly polarised radiation (i.e the radiation polarisation vectors are of the form given in equation 1.37).

Assuming that only circular polarisation is present in the incident radiation (i.e. $P_\zeta = P_\xi = 0$ in the density matrix). Hence, the interference cross section may be

obtained as

$$
\begin{aligned}
\frac{d^2\sigma_I}{d\Omega d\omega} &= \left(\frac{e^2}{mc^2}\right)^2 tr(<M_m>\rho<M_c>^+ - <M_c>\rho<M_m>^+) \\
&= \frac{1}{2}\mathbf{n(K)}\left(\frac{\hbar\omega}{mc^2}\right)\left(\frac{e^2}{mc^2}\right)^2 P_n \frac{K^2}{2k^2} \\
&\quad \left(\mathbf{S(K)}[\hat{k}' + \hat{k}\cos\phi] + \mathbf{L(K)}[\hat{k} + \hat{k}']\cos^2\phi/2\right)
\end{aligned}
\tag{1.42}
$$

Substituting $\frac{K^2}{2k^2}$ for $(1 - \cos\phi)$, one may obtain,

$$
\begin{aligned}
\frac{d^2\sigma_I}{d\Omega d\omega} &= \frac{1}{2}\mathbf{n(K)}\left(\frac{\hbar\omega}{mc^2}\right)\left(\frac{e^2}{mc^2}\right)^2 P_n(1 - \cos\phi) \\
&\quad \left(\mathbf{S(K)}[\hat{k}' + \hat{k}\cos o] + \mathbf{L(K)}[\hat{k} + \hat{k}']\cos^2\phi/2\right)
\end{aligned}
\tag{1.43}
$$

It is clearly possible to arrange the scattering geometry in order to isolate the atomic and spin magnetisation densities. Recently the first measurements of this kind have been reported by Collins et al (1989). The method consists of predicting the ratio of the spin and orbital magnetisation components in iron and cobalt.

1.7 The theory of charge Compton scattering

The cross section (equation 1.32) describing weakly scattered photons within the Born approximation was clearly derived in section 1.6.2. The cross section is a product of two terms; $(\frac{e^2}{mc^2})^2$ describes the nature of the scattering and a much more complicated term yields information about the target (i.e. charge density, spin and orbital of electron). For unpolarised photons the cross section is taken into consideration up to first order only, i.e.

$$
\frac{d\sigma}{d\omega} = \left(\frac{e^2}{mc^2}\right)^2 \sum_{\alpha\beta} \left| <\beta|\sum_j \mathbf{M}_j|\alpha> \right|^2 \delta(E_\beta - E_\alpha - \omega).
\tag{1.44}
$$

M_j is the matrix element of a scattered single electron at a position r_j with a momentum p.

$$\sum_j M_j = \sum_j e^{i\mathbf{K}.\mathbf{r}_j} \tag{1.45}$$

Within the framework of the impulse approximation, the system is treated as if all electrons are completely unbound. The Fourier transform of the matrix element defined earlier (equation 1.5) gives,

$$\sum_{\alpha\beta} \left| <\beta| \sum_j e^{i\mathbf{K}.\mathbf{r}_j}|\alpha> \right|^2 = \sum_j \left| \int \psi_i(\mathbf{r}_j) e^{-i\mathbf{p}_2 \cdot \mathbf{r}_j} e^{i\mathbf{K}.\mathbf{r}_j} dr_j \right|^2$$
$$= \sum_j \left| \int \psi_i(\mathbf{r}_j) e^{i(\mathbf{K}-\mathbf{p}_2).\mathbf{r}_j} dr_j \right|^2. \tag{1.46}$$

Clearly the final electron state $|\beta>$ has been considered as a plane wave, i.e. in the position space representation we have $|\beta> = e^{+\mathbf{p}_2 \cdot \mathbf{r}_j}$, and the initial electron state is $|\alpha> = \int \psi_i(\mathbf{r}_j) dr_j$. p_2 is the final electron momentum given as $p_2 = \mathbf{K} - p_1$. After substituting p_2 by its new expression, the matrix element may be reduced to,

$$\sum_{\alpha\beta} \left| <\beta| \sum_j e^{i\mathbf{K}.\mathbf{r}_j}|\alpha> \right|^2 = \sum_j \left| \int \psi_i(\mathbf{r}_j) e^{-i\mathbf{p}_1 \cdot \mathbf{r}_j} dr_j \right|^2$$
$$= n(\mathbf{p}) \tag{1.47}$$

The final expression of the matrix element is obtained using equation 1.5. Using the principle of conservation of momentum, the summation over all final states in the plane perpendicular to the scattering vector gives,

$$\left(\frac{d\sigma}{d\omega} \right)_{Th} = \left(\frac{e^2}{mc^2} \right)^2 |\epsilon_i.\epsilon|^2 \int_{p_x} \int_{p_y} n(\mathbf{p}) \delta\left(\omega - \frac{|\mathbf{K}|^2}{2m} - \frac{\mathbf{K}.\mathbf{p}}{m} \right) dp_x dp_y. \tag{1.48}$$

The double integral is commonly referred to as the momentum density distribution or the Compton profile.

1.8 Spin dependent Compton scattering

It is well known that the study of the Compton scattering within the framework of the impulse approximation is restricted by backscattering, i.e. the orbital moment contribution which is insignificant for such arrangement may be neglected from the magnetic part of the total photon cross section. Hence, the interference cross section becomes,

$$\frac{d^2\sigma_I}{d\Omega d\omega} = \frac{1}{2}\mathbf{n}(\mathbf{K})\left(\frac{\hbar\omega}{mc^2}\right)\left(\frac{e^2}{mc^2}\right)^2 P_c(1-\cos o)\mathbf{S}(\mathbf{K})\left[\hat{k}' + \hat{k}\cos\phi\right]. \qquad (1.49)$$

Choosing $\mathbf{k}$ to lie in the z direction (same as η), hence the leading term in $\mathbf{s}_z$ becomes,

$$\mathbf{S}(\mathbf{K})[\hat{k}' + \hat{k}\cos o] = 2\mathbf{s}_z \cos\phi. \qquad (1.50)$$

In reality, if we take into consideration the spin dependent effect, the momentum density distribution, n_p, becomes $(n_p^\uparrow + n_p^\downarrow)$, where $n_p^\uparrow$ and $n_p^\downarrow$ are the momentum density of the electrons for spin up and spin down respectively. By developing the matrix $\mathbf{s}_z$ along the vector polarisation (equation 1.37), and after adopting the same derivation used in the previous section, the differential spin dependent cross section obtained for opposite circular vector polarisation becomes,

$$\left(\frac{d^2\sigma}{d\Omega d\omega}\right)^\Delta = 4\mathbf{n}(\mathbf{K})\left(\frac{\hbar\omega}{mc^2}\right)\left(\frac{e^2}{mc^2}\right)^2 \cos\phi(\cos\phi - 1)$$
$$\int_{p_x}\int_{p_y}(n_p^\uparrow - n_p^\downarrow)\delta(\omega - \frac{|\mathbf{K}|^2}{2m} - \frac{\mathbf{K}.\mathbf{p}}{m})dp_x dp_y. \qquad (1.51)$$

where the integrated part is commonly referred to as the spin dependent Compton profile,

$$J_{mag}(p_z) = \int_{p_x}\int_{p_y}(n_p^\uparrow - n_p^\downarrow)dp_x dp_y. \qquad (1.52)$$

1.9 Band structure theories

Current band structure theories in condensed systems employ generally a single particle approximation. The solution of the Schroedinger equation for a many electron system is not a practical proposition, hence a many particle wave function may be represented as a product of single particle wave functions as stated in the Hartree and the Hartree-Fock approximations. In recent years, density functional theory has been introduced and provided an other variety of effective single particle theory. This method gives correct total energy and charge density of the ground state. This theory which is based on the Local Density Approximation (LDA) is simple to use since exchange and correlation effect are included within the single particle Hamiltonian. The LDA has been very successful in band structure calculations.

In recent years the band structures of transition metal have been treated using a few different theories namely; the Linear Combination of Atomic Orbitals (LCAO), the Combined Interpolation Scheme (CIS), the linear combination of Gaussian type orbitals (LCGTO), the Augmented Plane Wave (APW), the Korringa-Kohn-Rostoker (KKR), and recently the Full Linearised Augmented Plane Wave (FLAPW). A significant disagreement was usually obtained between these theories particularly in describing the majority and minority spin bands below the Fermi level.

The LCAO has not been satisfactory particularly outside core states where the potential is nearly flat and therefore cannot describe accurately the nearly free electron waves in this region. In a solid where orbitals from different atoms overlap, the LCAO consists of treating combined orbitals centred on different atoms. The

degeneracy is split into a band of states governed by the wave function

$$\psi_k(\mathbf{r}) = \sum_{lj} e^{i\mathbf{k}.\mathbf{l}} \beta_j \psi_a^j(\mathbf{r} - \mathbf{l}), \tag{1.53}$$

where $\psi_a^j(\mathbf{r} - \mathbf{l})$ is one of a set of different atomic orbitals on the atom at position $\mathbf{l}$ and β_j are the normalisation coefficients.

Four decades ago Slater and Koster (1954) introduced a new method of studying d-bands in metals. This method consists of an interpolation scheme which is based on the tight-binding approximation. In a solid the orbitals obtained from different atoms overlap into a single band of states. For instance, in transition metals, the d-states of the atom are compact with each core. The combination of those individual d-states are well defined in the d-band and they are usually represented by a wavefunction which is a LCAO. As a consequence the CIS method consists of an interpolation scheme for the d-bands in metals and a description of the s-p components of the band structure is based on a few plane waves. The basis set for the CIS contains five LCAO wavefunctions and four orthogonalised plane waves (see Hodges et al 1966).

In the case of the tight binding method, the wavefunction for a given state of wavevector $\mathbf{k}$ is given as,

$$\psi_k(\mathbf{r}) = \frac{1}{\sqrt{N}} \sum_{lj} e^{i\mathbf{k}.\mathbf{l}} C_j u_j(\mathbf{r} - \mathbf{l}), \tag{1.54}$$

where $u_j(\mathbf{r} - \mathbf{l})$ is a localised function. The wavefunction is constructed of 38 functions u_i. The functions for states other than 3d are linear combination of Gaussian type orbitals (LCGTO). The d-state is described by five radial Gaussian type orbital wavefunctions (GTO) (see Tawil and Callaway 1973).

The APW approximation based on the LDA is the first calculation which gave a reasonably satisfactory picture of transition metal band structure (see Wakoh at al 1977). In a muffin-tin potential which is assumed to be spherically symmetrical about each site and constant in the interstitial regions, the plane waves describe the system correctly within each sphere as well as the region between the spheres. The wavefunctions are given as

$$\psi_{\mathbf{k}}(\mathbf{r}) = e^{i\mathbf{k}\cdot\mathbf{l}}\psi_{\mathbf{k}}(\mathbf{r} - \mathbf{l}) \tag{1.55}$$

This wavefunction does however describe the whole potential of the lattice, hence the final wavefunction is constructed by the Bloch theorem. In principle the KKR is similar to the APW method although they look different. The KKR method is treated by means of Green's function (see Appendix A).

The APW method has been extended to the FLAPW method which is capable of treating the extreme limits of the isolated molecule (see Wimmer at al 1981). This method consists of solving Poisson's equation for the general potential and by including the Hamiltonian matrix elements due to the nonspherical terms of the potential operator inside the muffin-tin spheres. In order to treat the region inside the muffin-tin spheres correctly, the potential outside the muffin-tin spheres was approximated in such a way to that it does not depend on the the actual shape of the charge density inside the spheres but depends upon the multipole moments of this charge density.

Chapter 2

GAMMA-RAY COMPTON PROFILE
OF ZINC AND IRON-NICKEL ALLOY

2.1 Introduction

The study of gamma-ray Compton profile is a well established method which reveals
important information about the ground states of electron momentum density. This
technique is very sensitive to valence electrons which are responsible for bonding in
solids. Hence, it is very effective for the study of the electronic structure of solids
(see Williams 1977 and Cooper 1985).

2.1.1 Momentum density distributions in free atoms

The Compton profile of a given free atom is simply obtained from the summation
of distributions for electrons in the different shells of the free atom. Figure 2.1
illustrates the momentum distribution of zinc ($1s^2 2s^2 2p^6 3s^2 3p^6 4s^2 3d^{10}$) calculated
numerically, within the framework of the non-relativistic Hartree-Fock approxima-
tion, from a basis set of independent wavefunctions by Biggs et al (1975). Clearly
from the figure, the contribution from the most inner shells (i.e. core electrons),
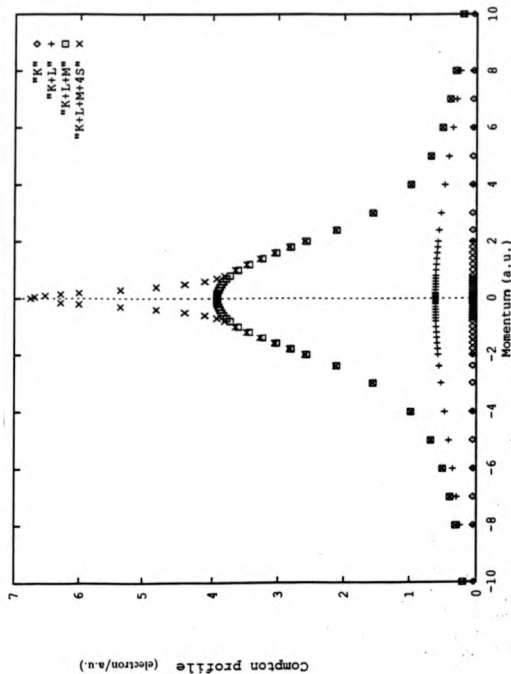
Figure 2.1 The free atom Compton profile of zinc ($1s^2 2s^2 2p^6 3p^6 4s^2 3d^{10}$) calculated numerically from Biggs et al (1975) within the non-relativistic Hartree-Fock approximation. Also shown are the contributions from the individual electron shells.

gives a flatter profile, whereas most outer electrons (i.e the valence electrons), give a localised contribution featured by a peaked profile centred around the origin; this is simply related to the velocity of electrons. Apart from inert gases (Eisenberger et al 1972), the free atom model is far from being valid because of the significance of the different effects arising from Coulomb interactions as well as the electron correlations and the exchange energy. These effects affect mainly conduction electrons which are responsible for bonds between atoms in solids. However, this model is accurate enough for the core electron and therefore, it is good for normalisation.

2.1.2 Momentum density distribution in simple metals

There exist some simple metals for which the theoretical treatment of their band structures is very simple. The simplest of all metals are those whose conduction electrons behave as in a non-interacting homogeneous free-electron gas, i.e. the electron correlation has a negligible influence on the core electron distribution. For such metals, the ground states of the conduction electrons in momentum space are included in a Fermi sphere of radius, $p_F = \hbar k_F$, known as the Fermi momentum. States outside the Fermi sphere are completely unoccupied and the Compton profile is an inverted parabola,

$$J(p_z) = \begin{cases} (\frac{3n}{4})\frac{p_F^2 - p_z^2}{p_F^3} & if \ p_z \leq p_F \\ 0 & otherwise \end{cases} \tag{2.1}$$

where n is the total number of conduction electrons existing within the Fermi sphere.

This simple model was applied successfully to alkali metals (Li and Na) as well as light metals such as Al and Mg, (see Phillips et al 1968 and Cooper et al 1974). The lineshape of the aluminum Compton profile obtained from that simple model is illus-

trated in figure 2.2. The Compton profile obtained from such a model overestimates the real contribution below the Fermi momentum, mainly because the Coulomb interactions within the conduction gas are neglected (see figure 2.3). Those interactions promote some electrons to the momentum states above the Fermi level and consequently increase the core distribution and decrease the peak height.

In real metals the conduction electrons must be affected by the periodic potential of the ion core lattice. Due to the periodic nature of the crystal potential, the valence electron wavefunctions obtained from the solution of the Schroedinger equation have the following form,

$$\psi_{\mathbf{k}}(\mathbf{r}) = U_{\mathbf{k}}(\mathbf{r})e^{i\mathbf{k}\cdot\mathbf{r}} \tag{2.2}$$

where $U_{\mathbf{k}}(\mathbf{r})$ are Bloch functions,

$$U_{\mathbf{k}}(\mathbf{r}) = \sum_{\mathbf{G}} a_{\mathbf{G}}(\mathbf{k})e^{i\mathbf{G}\cdot\mathbf{r}} \tag{2.3}$$

where $a_{\mathbf{G}}(\mathbf{k})$ are the expansion coefficients in the reciprocal lattice, $\mathbf{G}$ is a reciprocal lattice vector.

Under Dirac transformations (see section 1.2), the momentum density distribution may be obtained as,

$$\chi(\mathbf{p}) = \sum_{\mathbf{G}} a_{\mathbf{G}}(\mathbf{k}) \int e^{i(\mathbf{G}+\mathbf{k})\cdot\mathbf{r}} \cdot e^{-i\mathbf{p}\cdot\mathbf{r}} dr \tag{2.4}$$

$$= \sum_{\mathbf{G}} a_{\mathbf{G}}(\mathbf{k}) \delta(\mathbf{p} - \mathbf{k} - \mathbf{G}). \tag{2.5}$$

The momentum density distribution of an electron in state $\mathbf{k}$ is therefore deduced as,

$$n_{\mathbf{k}}(\mathbf{p}) = \sum_{\mathbf{G}} |a_{\mathbf{G}}(\mathbf{k})|^2 \delta(\mathbf{p} - \mathbf{k} - \mathbf{G}) \tag{2.6}$$
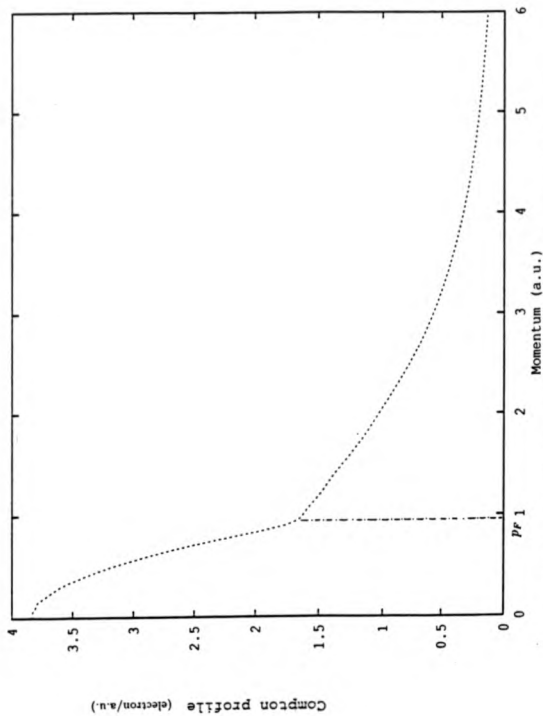
Figure 2.2 Free electron Compton profile + free ion core of aluminum. The discontinuity at the Fermi momentum disappears when the effects of the electron correlation are considered.
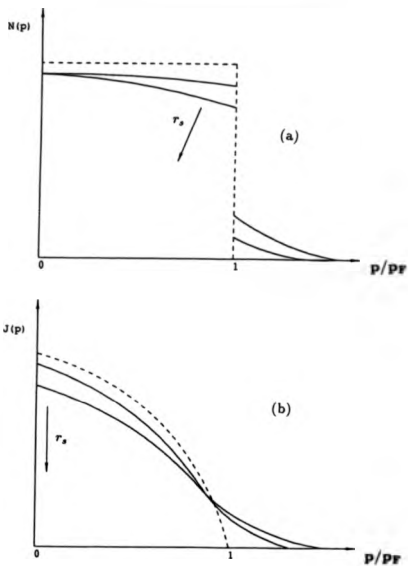
Figure 2.3 The effect of electron-electron correlation (solid line) on (a) the momentum density and (b) The Compton profile in a Homogeneous gas. The effect is determined by the Wigner radius r_s. The dashed curve represents the free electron limit.

The band momentum density, $n(\mathbf{p})$, may be obtained by summing $n_k(\mathbf{p})$ over all occupied states,

$$n(\mathbf{p}) = \sum_{\mathbf{k}} n(\mathbf{k}) \sum_{\mathbf{G}} |a_{\mathbf{G}}(\mathbf{k})|^2 \delta(\mathbf{p} - \mathbf{k} - \mathbf{G}) \qquad (2.7)$$

where $n(\mathbf{k})$ is the occupation function.

Figure 2.4 illustrates the two dimensional band construction for a nearly free-electron system. The Compton profile consists mainly of a central parabola centred at the origin of the reciprocal lattice (i.e. the centre of the first Brillouin zone), plus a series of decreasingly weaker parabolas centred at the origin of the second, third, etc... Brillouin zones.

2.2 Experimental systems

2.2.1 Gamma ray Spectrometers

The schematic diagrams of the low and high energy spectrometers are illustrated in figure 2.5. The spectrometers were designed and built about a decade ago (see Holt et al 1979) and have been used extensively and exclusively for the determination of momentum density distributions (see Holt 1978, Rollason 1984, Cardwell 1986 and Timms 1989). The spectrometers are quite similar in terms of constituency though the small differences were mainly depending upon the type of the source used. The higher energy source used is the ^{198}Au isotope obtained from an irradiated gold foil by thermal neutron flux. The source decaying process is governed by the following reaction,

$$^{197}Au(n,\gamma) \longrightarrow {}^{198}Au \xrightarrow{2.7d} {}^{198}Hg + \gamma(412keV) + \beta^- \qquad (2.8)$$
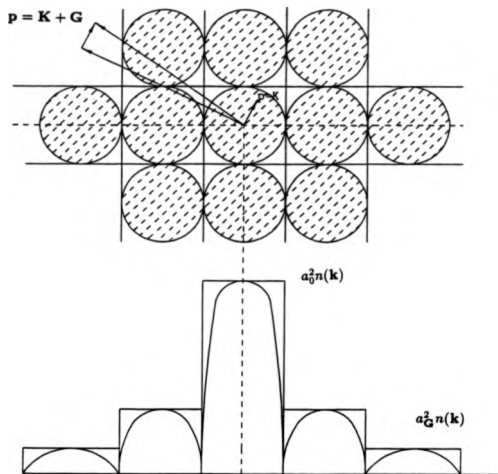
Figure 2.4 The Seitz model for nearly free electron gas in a square lattice. The effect of band structure is to promote electrons from a state $\mathbf{k}$ to a state $\mathbf{k + G}$. The main contribution comes from the first Brillouin zone. Less significant contributions are obtained at high momenta.
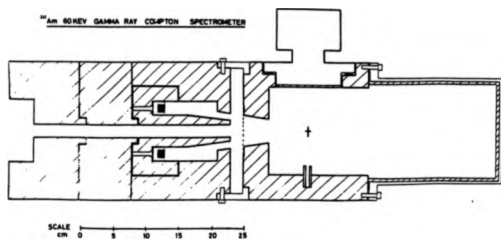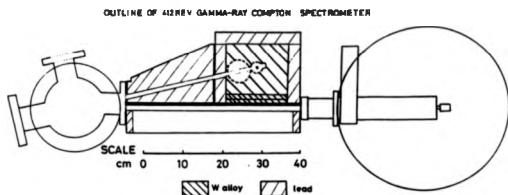
Figure 2.5 Schematic diagrams of the Compton scattering spectrometers; (a) the low energy (60keV) spectrometer and (b) the high energy (412keV) spectrometer.

The two sources have advantages and disadvantages, however, in most cases the disadvantages are minimised by the appropriate design of the spectrometer. For instance the low activity of the ^{241}Am source and its very high self absorption (40%), presented a big handicap in the early days to obtain a reasonable and adequate statistical accuracy over the whole region of the Compton profile in a reasonable length of time. The source half life is 458 years which is long enough to be able to run the experiment for a sufficiently long period in order to obtain enough integrated counts under the Compton peak. On the other hand, the longer the experiment is run, the higher is the risk of the data deteriorating due to electronic gain changes caused by temperature fluctuations (17 days are required to accumulate 10^5 counts at the origin of the Compton peak). Such an effect may be minimised whenever an air conditioning system in the experimental area is available. The drift in the electronics may be assessed by monitoring frequently the position and the width ($FWHM$) of the elastic peak.

As stated earlier, the Compton scattering is well established to be valid only for scattering angles close to 180° (see section 1.4). Moreover, the backscattering is essential in order to reduce the contribution of the angular divergence to the overall momentum resolution. The possibility of achieving such an arrangement may be realised when the source is placed as close as possible to the detector considering enough shielding between the source and the detector. However, with high energy sources, it is practically impossible to achieve such an arrangement due to the amount of shielding (mainly lead and heavy alloys) needed to stop unwanted radiation. Alternatively, it has been suggested that the backscattering arrangement could be achieved to some extent by using annular source geometry for which the detector

is positioned in such a way to look at the sample through the annular source along its axis (see figure 2.6) (see Weyrich 1975). This particular arrangement was very successful for obtaining scattering angles very close to 180°. Accordingly, Holt et al (1978) built the so-called low energy spectrometer located at Warwick University. The spectrometer was built around a 60 keV ^{241}Am source. The scattering angle was measured at 170° ± 1°. The source inner and outer diameters are respectively 2.6cm and 3.4cm. The beam is collimated along the surface of a cone through a block of lead. The scattering vector cannot be uniquely defined in such a scattering design. On the other hand, the scattering vectors could be found symmetrically distributed on the surface of a cone with a single component pointing towards the detector. Generally, this arrangement is very favourable for the study of polycrystalline samples where the scattering vector is randomly oriented with respect to the structure. Further considerations such as narrow incident collimation and long beam paths may be considered as a good approximation for the study of directional Compton profiles. The direction of the scattering vector may be averaged to be pointing towards the SSD and perpendicular to the sample face.

The high energy Compton spectrometer which is located at the Rutherford Appleton Laboratory (RAL) was designed by Holt et al (1979). In contrast with the low energy spectrometer, the high energy spectrometer was built around a block of tungsten material which encompasses the Gold source (^{198}Au). Principally the rectangular foil source is contained within a removable block of tungsten alloy in order to be able to be transported easily to be reactivated because of its very short half life ~ 2.7 days.

The background for such high energy sources may unfortunately be reduced at
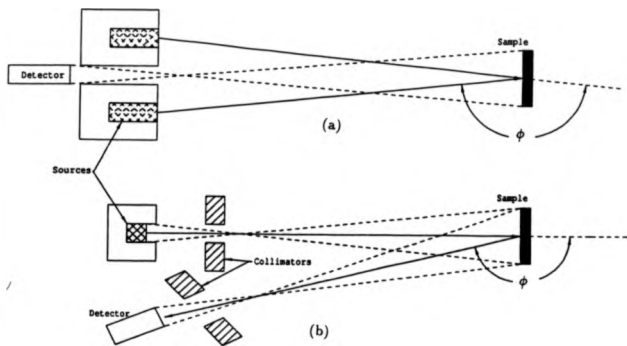
Figure 2.6 Schematic arrangement of the Compton scattering experiments; (a) the low energy (60keV) system and (b) the high energy (412keV) system.

the expense of the possible large scattering angle, principally because of the size
of the blocks of lead and heavy alloys separating the source from the detector. As
illustrated in figure 2.6, the scattering angle for the high energy system is 167°.
The source-sample and the sample-detector distances are, respectively, 476mm and
594mm. The radiated area at the sample position is equivalent to 18mm.

2.2.2 Solid State Detectors

Many different types of detectors may routinely be used in the detection of X-ray
scattering. However at the present time semi-conductor detectors, known as solid
state detectors, are considered as the most suitable for conducting Compton scat-
tering experiments. The semi-conductor devices consist of high purity material with
high carrier mobility such as germanium and silicon. The solid state detectors com-
monly used are either high purity germanium H-p-Ge or lithium drifted germanium
Ge(Li).

The detectors must be operated at liquid nitrogen temperature, principally to
reduce the noise in the amplifier, and furthermore, to prevent the lithium (Li) dif-
fusing out as in the case of Ge(Li). As a result, the Ge(Li) must be maintained
permanently running at liquid Ni temperature in order to avoid its destruction,
whereas the H-p-Ge cannot be damaged when they are left at warm temperatures
for some time. However, it is essential to cool the system down again for 24 hours
before operation. The detector resolution may be affected by the presence of crys-
tal imperfections as well as impurities inhomogeneously distributed throughout the
crystal. The carriers in the semi-conductors may be trapped by these imperfections
for a period exceeding the pulse-shaping time. The absorption of a photon in the

active region of the semi conductor by a photo-electric process may create a number of electron-hole pairs proportional to the energy of the absorbed photon. An applied electric field sweeps the electrons and holes to the electrodes. Consequently, the size of the current pulse created may be detected according to a charge-sensitive amplifier. The charge pulses collected are converted to voltage pulses in the pre-amplifier, then the output pulses are fed to the main amplifier where they are reshaped and transmitted to the Analogue to Digital Converter (ADC). The recorded counts of every photon energy are stored in a Multi-Channel Analyzer (MCA) which has a maximum scale of 4096 channels.

2.3 Data Reduction

2.3.1 The Compton scattering cross section in the relativistic limit

The inelastic scattering cross section obtained by Platzman and Tzoar (1970) within the framework of the impulse approximation for relativistically moving electrons must be rigorously modified in order to account for the initial relativistic scattered electrons. According to Jauch and Rohrlich (1955), the Compton scattering cross section for relativistic electrons may be dependent upon the momentum of the electron, p_1, before the scattering occurs. Hence, the Compton profile cannot adequately be related to the cross section as it has been illustrated in equation 1.48. Jauch and Rohrlich (1955) obtained a similar relationship dependent upon p_1,

$$\frac{d^2\sigma}{d\Omega\omega} = \frac{r_0^2 m^2 \omega_2 c^4}{2\omega_1 E_1 |\mathbf{K}| + \frac{\omega_2}{E_1}\Delta\omega} \int\int dp_x dp_y n(\mathbf{p}_1) X(\mathbf{p}_1) \tag{2.9}$$

where $X(\mathbf{p_1})$ is known as the flux vector.

$$X(\mathbf{p_1}) = \frac{\mathbf{p_1}.\mathbf{k}}{\mathbf{p_1}.\mathbf{k'}} + \frac{\mathbf{p_1}.\mathbf{k'}}{\mathbf{p_1}.\mathbf{k}} + 2m^2 \left(\frac{1}{\mathbf{p_1}.\mathbf{k}} - \frac{1}{\mathbf{p_1}.\mathbf{k'}} \right) + m^4 \left(\frac{1}{\mathbf{p_1}.\mathbf{k}} - \frac{1}{\mathbf{p_1}.\mathbf{k'}} \right)^2. \quad (2.10)$$

The extraction of the Compton profile from the cross section might be resolved by considering the initial electron as non-relativistic. Accordingly, Eisenberger and Reed (1974) simplified the cross section for scattering angles of the order of 180° which is close to that commonly obtained for Compton scattering experiments. Ribberfors (1975a) extended the same analysis by integrating by parts the cross section (equation 2.9) to obtain a rapidly converging series of terms each containing the Compton profile, $J(p_z)$, and a complicated factor X' (for detailed derivation see Ribberfors 1975b). Taking into account only significant terms (i.e. neglecting terms which are insignificant compared to $\frac{1}{z_1^2}$), the corrected double differential cross section becomes,

$$\frac{d^2\sigma}{d\Omega\omega} = \frac{r_0^2 m^2 \omega_2 c^4}{2\omega_1 E_1 |\mathbf{K}|} X' J(p_z) \quad (2.11)$$

2.4   Compton profile analysis

The Compton profile $J(p_z)$ can be related to the double differential cross section $D(\omega_2)$ by the following equation,

$$D(\omega_2) = C(\omega_2).J(p_z) \quad (2.12)$$

where ω_2 is the scattered photon energy. $C(\omega_2)$ is the Ribberfors cross section (see Ribberfors 1975b) and $D(\omega_2)$ is the double differential cross section which may be obtained from the data after being corrected from the systematic effects such as the background and the detector efficiency. Further reductions such as beam

attenuation. geometrical broadening and multiple scattering are also necessary (see figure 2.7), i.e.

$$D(\omega_2) = A^{-1}.S^{-1} * G^{-1} * E^{-1}.R^{-1} * [M(\omega_2) - B(\omega_2)] \tag{2.13}$$

where $*$ represents a convolution. $B(\omega_2)$ is the background noise, $M(\omega_2)$ is the measured energy spectrum, $R(\omega_2)$ is the detector resolution function, $E(\omega_2)$ is the detector efficiency $G(\omega_2)$ is the geometrical broadening function, $S(\omega_2)$ is the source broadening function and $A(\omega_2)$ is the absorption function. After such corrections, the Compton profile may now be effectively extracted after being normalised to the total number of electrons per atom and corrected for the multiple scattering. The Compton profile obtained from single scattering may be deduced according to the following formula,

$$J_{single}(p_z) = \alpha J_{total}(p_z) - J_{multiple}(p_z) \tag{2.14}$$

where α is a factor which conserves the data normalisation,

$$\alpha = \frac{\int J_{single}(p_z)dp_z - \int J_{multiple}(p_z)dp_z}{\int J_{single}(p_z)dp_z} \tag{2.15}$$

2.4.1 Background correction

In principle. the background to the Compton scattering may be separated from the Compton signal simply by joining a straight line between two points situated at the right and the left hand side of the peak. However, this simple method does not truly and effectively reduce the effect of the background because of the complexity of the problem. The background consists of two parts; a random part originating from a natural radioactivity such as cosmic rays etc..., and a second part which may be

BACKGROUND CORRECTION	$M(\omega_2) - B(\omega_2)$
DECONVOLUTION OF RESOLUTION FUNCTION	$R(\omega_2)$
DETECTOR EFFECIENCY CORRECTION	$E(\omega_2)$
DECONVOLUTION OF GEOMETRICAL BROADENING FUNCTION	$G(\omega_2)$
DECONVOLUTION OF SOURCE BROADENING FUNCTION	$S(\omega_2)$
ABSORPTION CORRECTION	$A(\omega_2)$
NORMALISATION	$C(\omega_2)$
MULTIPLE SCATTERING CORRECTION	$J_{Multi,\mu_0}(p_z)$
CORRECTED COMPTON PROFILE	$J(p_z)$

Figure 2.7 Outline of the procedure of the data reduction.

attributed to the radiation detected from the source, either through the shielding or scattered from the chamber walls, sample holder and molecules in the environment.

The second part of the background which is independent of the sample signal may be measured in a separate experiment, then must be scaled to match the background in the data before being subtracted. The scaling factor which is related to the source decay must be of the order of ~ 1, so that the statistical accuracy of the data may not be affected after the background subtraction (i.e. the background measurements must not be taken with a dying source). The time scaling factor (i.e. the period needed for the background measurements) may be estimated simply by measuring the source initial activity as well as the period of the data measurements. This principle is easily adopted, for the measurements of the Compton profile of many samples as well as the background for long half life sources such as ^{241}Am. However, for short half life sources such as ^{198}Au, the measurements of two samples and a background spectra are restricted by the short time of the activity of the source ($\sim$ 4 half lives).

The measurement of the random part (known elsewhere as the static background, Timms 1989) for the gold source revealed no significant effect (i.e. the random part is negligible). The insignificance of this part of the background is due to the relatively high activity of the gold source with respect to the cosmic rays. In addition, it is particularly important to know that the random background must only be measured when the source is completely removed from the spectrometer, rather than being measured with the source shut off, principally because some of the detected radiation may be obtained from the source through the shielding.

2.4.2 Absorption correction

Absorption is an important factor in the data correction especially for thick samples investigated with low energy sources. Figure 2.8 illustrates a clear description of the absorption process in the sample. A primary beam enters a sample of thickness (t) and making an angle (α) with the face of the sample. The scattered beam leaves the specimen with different angle β and an intensity,

$$I = I_0 \int \epsilon^{-\mu_1 x} . \epsilon^{-\mu_2 y} dv \qquad (2.16)$$

where $dv = S \frac{dt'}{\sin\alpha}$ (S is the beam cross section area), $x = \frac{t'}{\sin\alpha}$, $y = \frac{t-t'}{\sin\beta}$, and μ_1 and μ_2 are respectively the absorption coefficients of the sample for the incident and the scattered beam energies.

The integrated intensity over the sample thickness yields the absorption correction term,

$$A(\omega) = \frac{e^{-\mu_2 t \cos ec\beta} - e^{-\mu_1 t \cos ec\alpha}}{\mu_1 \cos ec\alpha + \mu_2 \cos ec\beta} \qquad (2.17)$$

2.4.3 Detector Efficiency

The probability of a photon being absorbed through a material of a thickness t is given as,

$$\frac{\Delta I}{I} = 1 - e^{-\mu(\omega)t} \qquad (2.18)$$

where $\mu(\omega)$ is the energy dependent photo-electron attenuation coefficient. The efficiency of such solid state detectors may be defined as,

$$Efficiency = \frac{Number\ of\ absorbed\ photons}{Number\ of\ photons\ entering\ the\ crystal\ detector}. \qquad (2.19)$$

The measurement of the detector efficiency may be carried out experimentally using Gamma-ray sources emitting several monochromatic radiations of well known
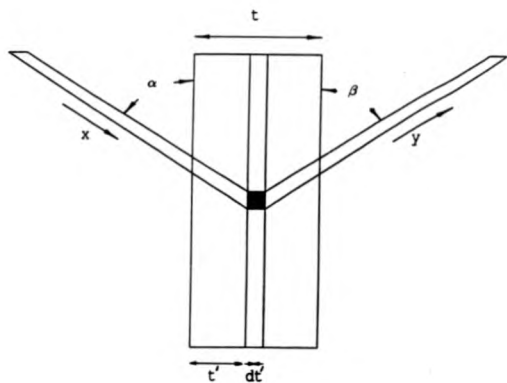
Figure 2.8 A schematic illustration for the absorption process in a thick sample.

relative intensities. Accordingly the ^{133}Ba radio isotope was deemed to be the most reliable source for such investigation (see Lederer et al 1967). Although the source is characterised by insufficient data points obtained within the region of the Compton peak (140-180keV) for the high energy system, the measurements were in good agreement with a Monte Carlo simulation of the detector (Laundy, 1986, private communication, see figure 2.9). As a result this simulation has been used to correct Compton data obtained on the high energy spectrometer system.

Clearly, equation 2.18 fails to describe the detector efficiency, especially at high energies, where the scattering process is less overwhelmed by the photoabsorption. Again it is also clear from the figure that the detector efficiency for the low energy system is 100% efficient. Hence, no such correction is necessary for the americium system.

2.4.4   Resolution correction

The statistical accuracy of Compton profile experiments may be easily improved at the expense of the total resolution. This might be obtained by increasing significantly the size of the sample, the crystal detector and the source (see figure 2.6). Consequently, the Compton profile lineshape may be deteriorated due to the large geometrical broadening function. In other words the Compton profile lineshape becomes broad as a result of the accumulation of different profiles, each originating from slightly different scattering angles. The total resolution may be approximated as,

$$R^2 = R_{Geo}^2 + R_{Det}^2 \tag{2.20}$$
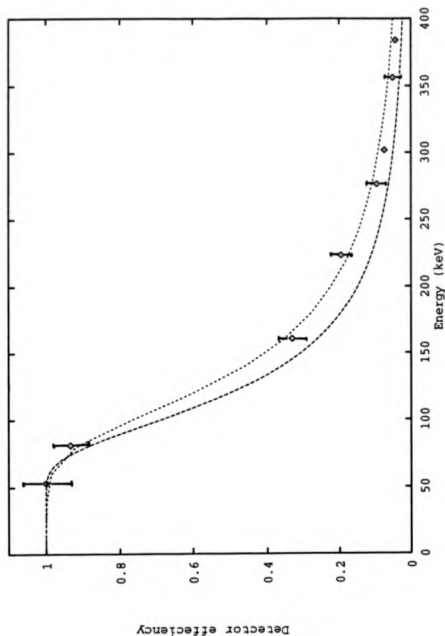
Figure 2.9 The detector efficiency obtained from the emission lines of ^{133}Ba compared with a calculation obtained from equation 2.18 (dashed line) and a Monte Carlo simulation (dotted line). The agreement is good at the Compton profile position obtained from the high energy system.

where R_{Geo} and R_{Det} are respectively the geometrical broadening resolution and the detector resolution which are assumed to be Gaussian.

The detector resolution is usually measured only at the energy corresponding to the Compton profile centre and it is approximated to be energy independent over the whole range of the Compton profile. This approximation has been made due to the absence of a tunable monochromatic source to determine the detector response as a function of energy through the range of the Compton profile (-10 a.u. , +10 a.u.), i.e. 13keV for the americium system and 23keV for the gold system. The measurement of the resolution function is effectively quoted as the full width at half maximum (FWHM) of Gaussian at a particular energy. The detector resolution for the americium system was measured at the incident photon energy, i.e. at 60keV, due to the unavailability of a suitable source with energy close to 48keV. On the other hand, the measurement of the detector response function for the gold system at the Compton peak energy 159keV was carried out with a weak ^{191}Te calibration source. The total resolution function for the low and the high energy systems were determined to be respectively 0.57 a.u. and 0.40 a.u.

2.5 Zinc

2.5.1 Previous research

In recent years, very few experiments have been carried out on the momentum density distribution of zinc. The isotropic Compton profile of zinc was measured with a ^{241}Am $60keV$ source for the first time by Manninen et al (1974). The data were later corrected for multiple scattering (see Pakkari et al 1975). The experimental

results were in good agreement with LCAO calculations performed by Aikala (see Pakkari et al 1975). The experimental results were deconvoluted with the residual instrumentation function (RIF) in order to remove the effect of the finite experimental resolution (Paatero et al 1974). Rayleigh scattering of photons (i.e. coherent scattering) on polycrystalline zinc was measured using $100m\mu Ci$ ^{241}Am source with photon energy of $59.54keV$ (see Eichler et al 1984). The cross section was measured at scattering angles ranging from $20°$ to $90°$. The results were in good agreement with the theory within the experimental error $(4 - 10\%)$. The only directional measurements were carried out using positron annihilation method (see Mogensen et al 1969) and very small anisotropies were observed in the linear slit angular curves.

As far as directional Compton profile theory is concerned, the only attempted calculation was carried out by Aikala (1975). Unfortunately the theory failed to achieve an appropriate result mainly because the effect of the core orthogonalization was omitted. The uncertainties in the calculation were found to be very important in the directional profiles because of their higher sensitivity to the wavefunctions than what was revealed in the isotropic profile. Aikala (private communication) made another unsuccessful attempt to include the effect of the core orthogonalization. The failure is mainly due to the complicated calculation in hexagonal close-packed structures.

The study of the Fermi surface of zinc raised a disagreement until Stark et al (1967) performed an accurate pseudopotential calculation and obtained results which were later confirmed experimentally by Stenhaut et al (1967), who obtained detailed dimensions of the zinc Fermi surface using radio frequency size effect measurements. The agreement was found to be excellent (i.e. within 1% difference). As far as the

hexagonal close packed structure is concerned, one of the major corrections applied to the Fermi surface calculation is governed by the modified ratio of the inter-atomic distances (i.e. $c/a = 1.8246$), which exceeds the ideal value by about 10%, hence, causing a shrinking of the Brillouin zone parallel to c by about 10%.

2.5.2 Experimental details

The present experiments were performed at Warwick University and the Rutherford Appleton Laboratory (RAL) using, respectively, the low and the high energy systems. A schematic diagram of the experimental arrangements is illustrated in figure 2.6. Clearly, the scattering is obtained by reflection. The three sample discs of zinc single crystal were cut from a randomly oriented cylinder ($50 \times 12mm$) purchased from Cambridge Metal Crystal Ltd. The orientation of the slices were verified using the Laue method. The technique was used to identify the orientation of the cylinder axis which was found to be $10\bar{1}0$. The other two major orientations ($0001, 11\bar{2}0$) were obtained simply by rotation using a goniometer with two degrees of freedom. Hence, the crystal cylinder was cut and shaped, by means of a spark erosion method, into three similar discs ($11.50 \times 2.1mm$) oriented along the major orientations.

Individual spectra were accumulated for each sample. Approximately 10^8 counts were accumulated at the Compton peak centre over a period of about 2 weeks for the low energy system and for (2-5 days) for the high energy system depending upon the source activity. Two gold sources were necessary for the measurements of the three directions with good statistical accuracy. This is mainly due to the short half life of the gold source (2.7 days).

The raw data were corrected and processed as outlined in the diagram 2.7. The

data were corrected from the multiple scattering using a Monte Carlo simulation. The multiple scattering distribution obtained from an input of 18×10^{6} photons (see figure 2.10) was cubic spline fitted so that the Compton data obtained from the processed single scattering might not need further corrections due the random statistical fluctuations. The normalisation factor α was calculated over the momentum range (0a.u., +5a.u.), to be 1.1065 and 1.1350 respectively for the low and the high energy systems (i.e. the multiple scattering contribution is evaluated as to be 9.6% and 12.5% respectively for the two systems).

The processed high energy data were normalised to the free atom total number of electrons (12.03) included within the range (0a.u.,+5a.u.). However , the processed low energy data were normalised only to a fractional number of electrons responsible for the scattering which were accurately estimated to be 11.87. Those non-excited electrons are included in the K-shell. This is due to the energy transfer which is smaller than the binding energy of those electrons (K-edge threshold energy = 9.656keV).

2.5.3   Results and Discussion

The experimental directional Compton profiles of zinc are listed in table 2.1. Also tabulated are the isotropic LCAO calculation and the Hartree Fock free atom profile taken from Biggs et al (1975). The theoretical data have been convoluted with a Gaussian of Full Width at Half Maximum ($FWHM = 0.40a.u.$), corresponding to the system's total resolution function.

The electron momentum density is a centro-symmetric function, therefore it was necessary to recover the inherent symmetry of the Compton profiles by reducing the

p_z	Exp-000$\bar{1}$	Exp-10$\bar{1}$0	Exp-11$\bar{2}$0	$J_{iso}(p_z)$	$(Theory)_{iso}$	Free atom
0.0	5.55309	5.53864	5.52757	5.52821	5.50278	6.28490
0.1	5.52872	5.51719	5.51008	5.50806	5.47677	6.16458
0.2	5.46484	5.44870	5.43831	5.4375	5.39076	5.83976
0.3	5.32561	5.32500	5.31705	5.31423	5.25074	5.40022
0.4	5.15174	5.15994	5.15103	5.14773	5.05671	4.94676
0.5	4.94200	4.95262	4.92575	4.93267	4.80868	4.55263
0.6	4.69538	4.70042	4.67050	4.68031	4.52564	4.24844
0.7	4.42743	4.44066	4.41760	4.42268	4.23060	4.02994
0.8	4.16974	4.19489	4.18060	4.17931	3.98456	3.87520
0.9	3.95541	3.98052	3.97553	3.96923	3.82454	3.75941
1.0	3.78599	3.81013	3.80137	3.79760	3.72352	3.66274
1.2	3.53427	3.53243	3.52567	3.52485	3.54850	3.48023
1.4	3.28982	3.27784	3.28508	3.27805	3.34447	3.27983
1.6	3.05264	3.05621	3.05673	3.05165	3.11144	3.05609
1.8	2.81887	2.80924	2.81694	2.80998	2.86240	2.81981
2.0	2.57118	2.56710	2.55999	2.56105	2.60937	2.58163
2.5	2.00949	2.01391	2.00519	2.00673	2.02888	2.02127
3.0	1.55425	1.55889	1.56206	1.55740	1.56922	1.56697
3.5	1.20679	1.21574	1.20818	1.20952	1.22717	1.22928
4.0	0.96320	0.96670	0.96372	0.96357	0.98214	0.98469
4.5	0.77791	0.78238	0.77891	0.77916	0.80511	0.80582
5.0	0.64840	0.65741	0.65098	0.65245	0.67410	0.67382
5.5	0.54803	0.56128	0.55700	0.55677	0.57456	0.57427
6.0	0.46588	0.47432	0.46766	0.46960	0.49707	0.49679
6.5	0.39601	0.41281	0.40610	0.40696	0.43418	0.43375
7.0	0.34200	0.35051	0.34000	0.34431	0.38205	0.38149
7.5	0.29419	0.30513	0.29136	0.29725	0.33799	0.33770
8.0	0.25375	0.26796	0.25928	0.26184	0.30004	0.30025
8.5	0.21389	0.23460	0.21764	0.22406	0.26671	0.26739
9.0	0.19138	0.20513	0.18996	0.19639	0.23746	0.23836
9.5	0.16798	0.18810	0.17137	0.17781	0.21200	0.21256
10	0.16172	0.16172	0.16091	0.16115	0.19003	0.10908

Table 2.1 Experimental Compton profiles of Zn for 000$\bar{1}$, 10$\bar{1}$0 and 11$\bar{2}$0 directions, measured on the high energy spectrometer system. Also tabulated are the experimental isotropic profile obtained from equation 2.22, the isotropic theory (taken from Aikala et al 1975) and the relativistic free atom profile (taken from Biggs et al 1975). The theories have been convoluted with the corresponding experimental resolution function of FWHM=0.4a.u.
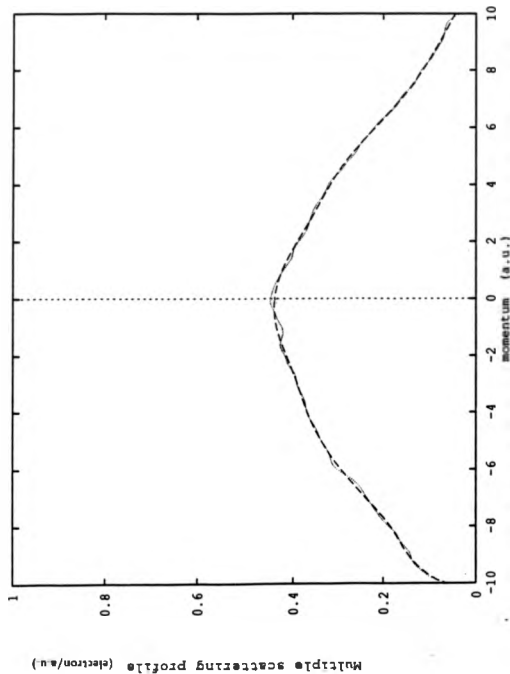
Figure 2.10 The multiple scattering profile of FeN_3 obtained for an energy of 412keV; the monte Carlo simulation output (dotted line) obtained from an input of 18×10^4 photons and its cubic spline fit (dashed line).

different effects outlined in figure 2.7. The 0001 profile asymmetry is shown in figure 2.11 where clearly the difference between the low and the high energy sides of the Compton profile are within 1%. The similarity between the low and the high energy side of the Compton enables the data to be averaged for anisotropy interpretations.

Since anisotropy effects contain more fine structure than isotropic profiles do, it is desirable to have the directional profiles compared with an accurate calculation. However, in the absence of proper directional Compton profile calculation, the experimental data were averaged for isotropic system, i.e.

$$J_{iso}(p_z) = \frac{1}{7}[3J_{10\bar{1}0}(p_z) + 3J_{11\bar{2}0}(p_z) + J_{0001}(p_z)]. \tag{2.21}$$

The averaged isotropic profile is compared with the LCAO calculation (see Aikala et al 1975). Clearly from figure 2.12 the difference between the theory and the experiment exhibits over all good agreement, especially at high momenta. The small differences $(2-3\%)$ between theory and experiment around the Fermi momentum are commonly obtained (i.e. theoretical profiles are usually too large below the Fermi momentum and too small immediately above it). This discrepancy indicates the underestimation of the electron correlation effects in the theory.

2.5.4 Anisotropy

Since the core electron contribution is of very small interest as far as the Compton scattering objective is concerned, therefore, to make progress in the analysis of valence electrons which are responsible for the band structure of solids, the Compton profile data are usually interpreted in terms of differences between directional profiles
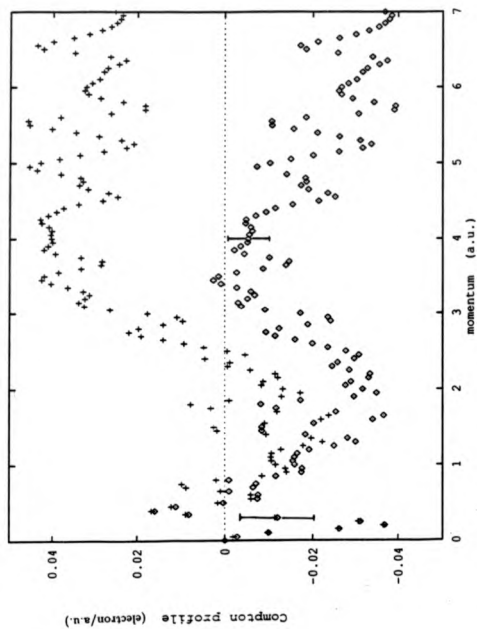
Figure 2.11 Asymmetry in the 0001 Compton profile measured on the high energy spectrometer system, (•) before correction for multiple scattering and (+) after correction for multiple scattering.
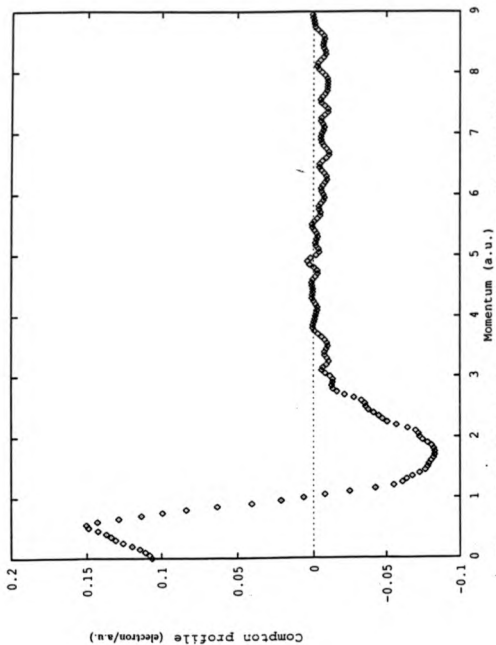
Figure 2.12 The difference between theoretical and experimental isotropic data obtained using equation 2.22, measured on the high energy spectrometer system. The theory has been convoluted with a Gaussian of $0.40 a.u.$ FWHM before comparison with experiment.

i.e.

$$\Delta J(p_z) = J_{hkl}(p_z) - J_{h'k'l'}(p_z). \tag{2.22}$$

where hkl denote crystallographical directions. This method is very effective since it eliminates the systematic error in the data as well as the core contribution. The oscillations obtained in anisotropies may clearly be understood by studying the Fermi surface, i.e. directional Compton profiles obtained by integration over the scattering plane intersect with the Fermi surface by varying amounts, which depend firstly upon the orientation of the plane and secondly on the location of the plane with respect to the valence bands.

The experimental directional Compton profile differences obtained from the low and high energy system are illustrated in figure 2.13. Clearly the data exhibits very small anisotropies which confirm the positron annihilation measurements. The difference at the Compton peak is estimated to about $1/2\% J(0)$. The small magnitude of the oscillations observed in all anisotropies indicates a relatively spherical Fermi surface. The qualitative differences between the low and the high energy data may be related to some kind of deffeciency in the data collection (the remeasuments of the data were not possible due to the heavy scheduled spectrometer). Those differences become very important, especially when small anisotropies are revealed. For instance, the high energy side of the Compton profile contribution is effectively reduced due to the K-absorption edge ($9.656 keV$) which lies around $2.4 a.u.$ (i.e. K-shell electrons cannot be excited with photon energy of $59.54 keV$ due to small energy transfer).
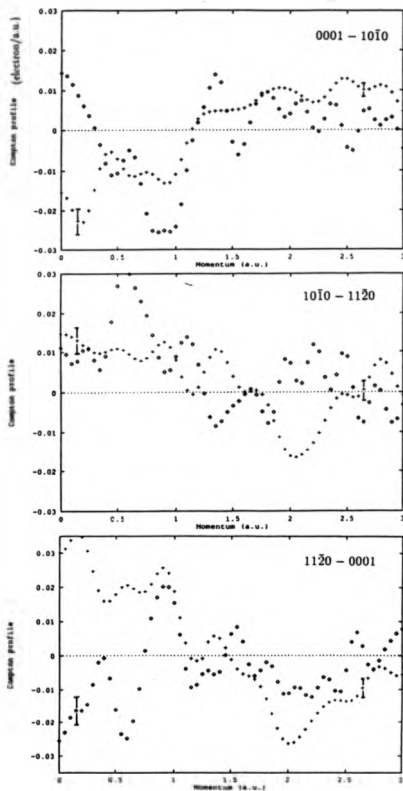
Figure 2.13 Experimental anisotropies for zinc data measured on the high spectrometer system (o) and the low energy spectrometer (+).

2.6   Iron-Nickel alloy

2.6.1   Introduction

The ultimate goal of the study of the directional Compton profiles of iron-nickel alloy ($FeNi_3$) was focused on obtaining accurate data to investigate the validity of a recent KKR-CPA calculation (see Staunton 1987). Recently, Timms (1989) carried out similar measurements on Fe rich FeNi alloy. Clear discrepancies were revealed with the KKR-CPA and the RB-APW calculations. The most frequently studied alloys are nickel or iron based substitutional systems. This is to reveal the changes which occur in those two transition metals such as the radius of the Fermi Surface along different orientations.

A substitutional alloy ($A_x B_{1-x}$) usually falls into two kinds of solution (ordered or disordered). In a disordered substitutional alloy (i.e. a solid solution of two kind of metals), the distribution of atoms on a regular lattice is random. In transition metal where the d-band is half filled, ordering is obtained since the filled bonding states of the ordered state are lower than those of the clustring because of the level repulsion. An alloy of Fe and Ni metal adopts the FCC structure for a nickel concentration of less than 65 at %. In the case where the d-orbitals of Fe are similar in energy and wavefunction to those of nickel, the disorder of the alloy would be irrelevant (i.e. electrons occupying the d band would not differentiate between the two kind of atoms). On the other hand, if the d-bands of the two constituent atoms are different, the system would have two sets of d-bands associated with Fe and Ni sites respectively (i.e. the energy cannot be well defined with the lattice translation vector because the symmetry of the structure disappears).

As far as magnetism is concerned, the averaged moment per site as well as the Curie temperature rise with increase of Fe concentration (the magnetic moment of an atom for a given iron-nickel alloy composition exists at a given composition associated with the two constituent atoms, i.e. μ_{Fe} and μ_{Ni}). For iron concentrations near 25 at %, the Curie temperature suddenly changes its slope and starts to decline whereas the magnetic moment continue to rise until a concentration of 64 at % where it starts to decline in its turn. This behaviour is believed to be attributed to the ferromagnetic exchange interactions between local magnetic moment at Fe sites; the ferromagnetic state may be perturbed for a large number of nearest neighbour Fe pairs. Direct evidence of such features was predicted from a single spin-only model (see Eggarter et al 1977, Lawrence et 1986). Moreover, Pinski et al (1986) and Kakahashi (1983) and Hasegawa (1981) consolidated those features by predicting theoretically that iron in an FCC lattice would be anti-ferromagnet for a concentration near 25 at %.

2.6.2 Experimental analysis

Three directional Compton profiles (100, 110, 111) of iron-nickel alloy, $FeNi_3$, were measured using both high and low energy systems. The three disc samples (15 × 2.0mm) were cut and shaped in a similar way as for zinc. The Laue method was again used for directional orientations. Electron microscope analysis of Fe and Ni fluorescent lines revealed the exact composition of the FeNi alloy (i.e. $27 \pm 0.4\%$ Fe, and $73 \pm 0.4\%$ Ni).

Individual spectra were recorded for each sample using both systems. Due to statistical accuracy requirements, integrated counts of 10^7 were accumulated over

the range $-10a.u.\,to + 10a.u.$ for each profile. Each spectrum was recorded over a period of time fractionally shorter than that for zinc due to the smaller rate of the photo-electric absorption in the iron-nickel alloy.

The data were processed as outlined in diagram 2.7. The correction from the multiple scattering revealed a normalisation factor of $\alpha = 1.1587$ over the region $(0a.u., +5a.u.)$ for the high energy system, (i.e. the multiple scattering represents 13.7% of the total profile). The data were normalised to a free atom profile obtained from Biggs et al (1975).

2.6.3   Results and discussion

The experimental directional Compton profiles of iron-nickel alloy are listed in table 2.2. The 100 directional Compton profile of FeNi is shown in figure 2.14 The asymmetry curves for the 100 processed profile for the two systems are shown in figure 2.15. Clearly from the curves the profile obtained from the high energy system is characterised by excellent centro-symmetry which is an important feature of the electron momentum density. The anisotropy profiles for FeNi are shown in figure 2.16. Also illustrated are the theoretical anisotropies. The theoretical calculation was based on the KKR scheme. (Staunton, Private communication). The theoretical prediction of the oscillations in the anisotropy lineshape is in very good agreement with the experiment. Although a qualitative agreement is obtained between theory and experiment, quantitatively it was a complete disagreement. This discrepancy is possibly attributed to the overestimation of the normalisation of the core states. Significant differences in the scale of the anisotropies are revealed. A difference of 2% *at* $J(0)$ between the directional profiles is obtained which is almost three times

p_z	Exp-100	Exp-110	Exp-111	Free atom
0.0	5.24445	5.28853	5.24166	6.39307
0.1	5.22434	5.27192	5.22241	6.25672
0.2	5.17379	5.21475	5.16539	5.89146
0.3	5.10268	5.11941	5.07702	5.40449
0.4	4.99280	4.98365	4.95530	4.91234
0.5	4.83687	4.82301	4.80270	4.49479
0.6	4.64909	4.64835	4.62373	4.17996
0.7	4.44031	4.44704	4.43078	3.95682
0.8	4.25077	4.24670	4.24012	3.79707
0.9	4.06194	4.06486	4.04815	3.67213
1.0	3.85846	3.88342	3.86729	3.56113
1.2	3.51396	3.55191	3.52805	3.33772
1.4	3.17091	3.21837	3.19112	3.06968
1.6	2.85968	2.89075	2.85976	2.82109
1.8	2.57024	2.55602	2.56762	2.54904
2.0	2.29563	2.26259	2.29623	2.28814
2.5	1.72432	1.73413	1.73337	1.73037
3.0	1.31825	1.31388	1.32948	1.31343
3.5	1.02693	1.01404	1.03197	1.02140
4.0	0.82891	0.82647	0.84381	0.82224
4.5	0.69322	0.67891	0.70171	0.68195
5.0	0.59045	0.57928	0.60046	0.57925
5.5	0.51560	0.50103	0.52178	0.49966
6.0	0.44896	0.43486	0.46094	0.43561
6.5	0.40395	0.38087	0.40482	0.38245
7.0	0.35187	0.33855	0.36207	0.33734
7.5	0.31159	0.29710	0.31519	0.29831
8.0	0.27016	0.25270	0.28267	0.26424
8.5	0.23351	0.21927	0.24349	0.23437
9.0	0.20629	0.19418	0.21778	0.20820
9.5	0.18896	0.17511	0.19794	0.18511
10	0.19118	0.18168	0.20301	0.09479

Table 2.2 Experimental Compton profiles of $Fe_{0.25}Ni_{0.75}$ for 100, 110 and 111 directions, measured on the high energy spectrometer system. Also tabulated is the non-relativistic free atom Compton profile obtained from Biggs et al (1975). The theory has been convoluted with the corresponding experimental resolution function of FWHM=0.4a.u.
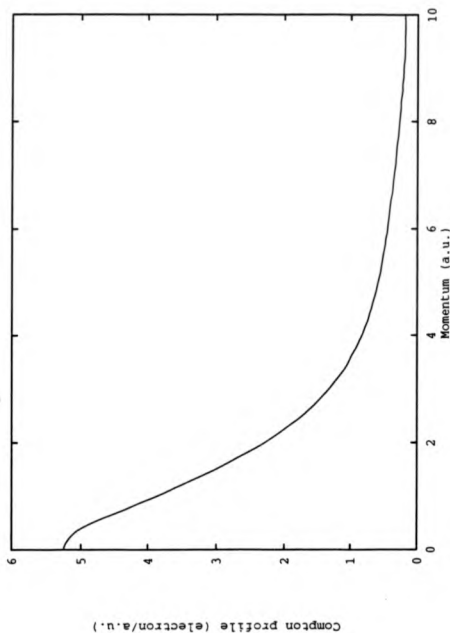
Figure 2.14 100-directional compton profile of $Fe_{0.25}Ni_{0.75}$ obtained with the high energy source ^{198}Au.
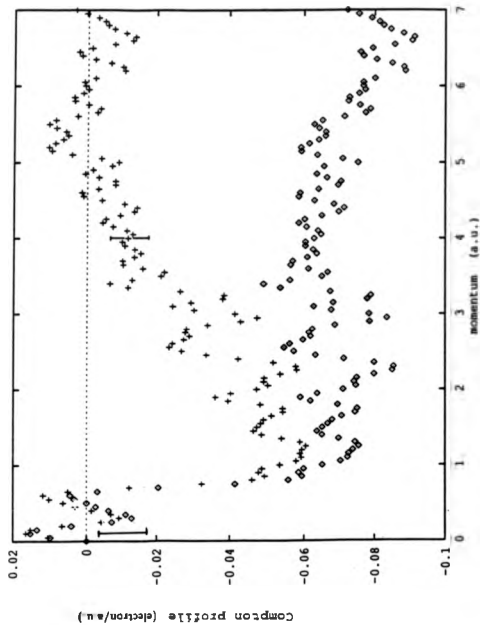
Figure 2.15 Asymmetry in the 100 Compton profile measured on the high energy spectrometer system, (•) before correction for multiple scattering and (+) after correction for multiple scattering.
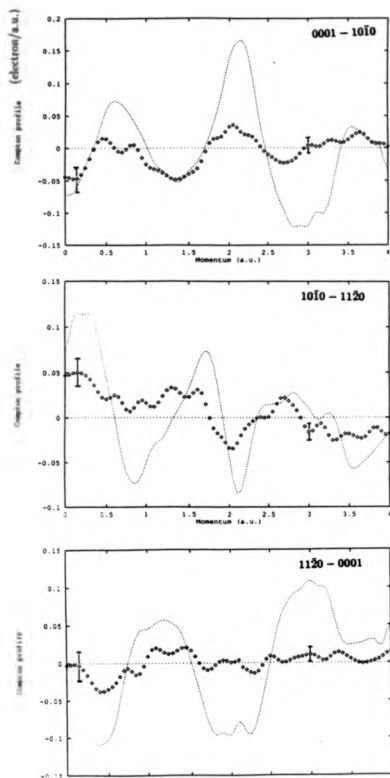
Figure 2.16 Experimental anisotropies for $Fe_{0.25}Ni_{0.75}$ data measured on the high energy spectrometer system (•) and the RB-KKR theory (dashed line). Clear disagreement is revealed in the scale of the anisotropies.

as much that experimentally measured.

The difference between the theoretical and the experimental absolute profile 100 (see figure 2.17) provides further evidence about the overestimation of the core normalisation which badly affects the correlation effects. Clear disagreement is obtained over the whole range of the Compton profile particularly at high momenta where the agreement is commonly predicted as it is the case for the free atom profiles (see figure 2.17). Hence, the theory needs further adequate corrections in order to be able to make any real progress in the data interpretation.
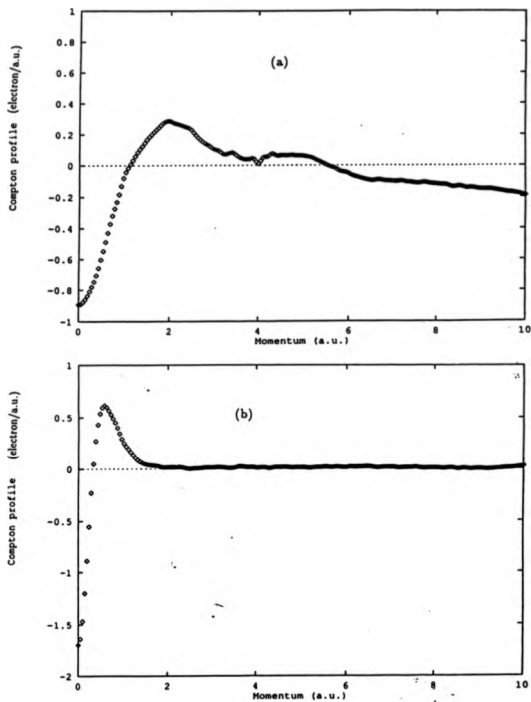
Figure 2.17 (a) The difference between the theoretical (RB-KKR) and the experimental 100 directional Compton profile measured on the high energy system. Significant disagreement is obtained even at high momenta. (b) Experimental (100) - free atom profile of $Fe_{0.25}Ni_{0.75}$. Good agreement is obtained at high momenta. The theories have been convoluted with a Gaussian of $0.40a.u.$ FWHM before comparison with the experiment data.

Chapter 3

SYNCHROTRON RADIATION
AND POLARISATION MEASUREMENTS

3.1 Introduction

A brief overview of the more important aspects of synchrotron radiation (SR) is given
in this chapter as well as a comprehensive introduction to its major properties. In
addition the measurements of the polarisation of synchrotron radiation by means of
the technique of Compton scattering are described in detail.

Synchrotron radiation was first discovered in 1947 at the General Electric 70-
MeV synchrotron (Elder et al 1947), although the consideration of radiation emit-
ted from the acceleration of charged particles (electrons, positrons) goes back to the
end of the 19th century (Lienard 1898). In 1947 Elder studied the connection of
the experimental results with the spectral distribution predicted earlier from accel-
erating charged particles. The results were in a good agreement with the spectral
distribution derived from the passage of a relativistic electron through a magnetic
field. At that time many research scientists (Corson 1952, Tomboulian et al 1956,

Codling and Madden 1964) showed a great interest in this discovery by investigating experimentally the different theoretical predictions reported for the properties of this particular radiation using the few synchrotron machines available. These were the 250 MeV synchrotron at Lebedev Institute in Moscow, the Cornell 300 MeV synchrotron, the 180 MeV synchrotron at the National Bureau of Standards (NBS) in Washington D.C. and the 6 GeV synchrotron in Hamburg. By the late 1970s the impact of synchrotron radiation on scientific research was evident from the construction of storage rings in different parts of the world (table 3.1), dedicated to users of the radiation rather than the nuclear physicists studying the properties of the circulating particles.

The development of synchrotron radiation especially in the last couple of decades has contributed significantly in a variety of fields such as condensed matter physics, chemistry and protein crystallography. The unique quantitative and qualitative results were basically achieved with the introduction of multi-GeV storage rings which showed greater stability and higher stored beam currents than synchrotrons. In storage rings the electrons are injected from powerful accelerators at the operating energy, whereas in synchrotrons the electrons are repeatedly accelerated within the ring itself from low to high energy which results in the variation of the electron current as well as the electron beam position from one cycle to another. As a result the existing storage rings are capable of producing higher and stable total radiation emitted within a very small opening angle of the order of $\frac{1}{\gamma}$ ($\gamma = \frac{E}{m_0 c^2}$, where E is the energy of the accelerated electron and $m_0 c^2 = 511 keV$ is the electron rest energy). The total intensity emitted is several order of magnitude higher than any other sources over a broad bandwidth, from the infra red region $10^3 \mathring{A}$ to the hard

Name	Location	E(GeV)	I(ma)
ACO	ORSAY (FRANCE)	0.7	100
NSLS	BROOKHAVEN (USA)	0.75	500
UVSOR	OKAZAKI JAPAN	0.75	500
VEPP-2M	NOVOSIBIRSK (USSR)	0.80	100
SPRL	STANFORD (USA)	1	500
BESSY	BERLIN (FRG)	0.8	500
ALADIN	WISCONSIN (USA)	1.3	500
PAKHARA	MOSCOW (USSR)	1.36	300
DCI	ORSAY (FRANCE)	1.8	300
SRS	DARESBURY (UK)	2.0	500
VEPP-3	NOVOSIBIRSK (USSR)	2.25	100
PHOTON FACTORY	TSUKUBA (JAPAN)	2.5	500
NSLS	BROOKHAVEN (USA)	2.5	500
SIBERIA II	MOSCOW (USSR)	2.5	300
SPEAR	STANFORD (USA)	4.0	100
VEPP-4	NOVOSIBIRSK (USSR)	7.0	10
CESR	ITHACA (USA)	8.0	100
PETRA	HAMBURG (FRG)	18.0	18
PEP	STANFORD (USA)	18.0	10

Table 3.1 Synchrotron radiation facilities dedicated to radiation users.

X-ray region $10^{-1} \mathring{A}$ (range of photon energy from 10 eV to 100 keV).

3.2 Synchrotron radiation

3.2.1 Radiation emitted from an electron moving in uniform circular motion

The radiation emitted from a centrepetally accelerated electron or positron has been well established since the first classical examination of the model by Lienard (1898). The total power generated from a high energy electron, with a charge (e) and a rest mass (m) in uniform circular motion accelerated radially in a magnetic field was treated classically by Schwinger (1949) who based the calculation on Larmor's formula for an electron instantaneously at rest. The result is

$$P = \frac{2}{3} \frac{e^2}{m^2 c^3} \left(\frac{d\mathbf{p}}{dt} \right)^2 \tag{3.1}$$

where p is the the electron momentum.

However the relativistic form of the radiation power (equation 3.1) may be obtained as,

$$P = \frac{2}{3} \frac{e^2 c}{R^2} \beta^4 \left(\frac{E}{mc^2} \right)^4 \tag{3.2}$$

where R is the radius of curvature of the orbit and $\beta = v/c$

Clearly the radiation power, proportional to $(\frac{E}{mc^2})^4$, is strongly dependent upon the energy of the accelerated particle. On the other hand it is also strongly dependent upon the mass of the particle. Therefore , the synchrotron radiation produced from accelerated protons, compared to electrons, may be considered negligible.

For a non-relativistic centrepetally accelerated electron i.e. $\gamma = \frac{E}{m_0 c^2} \ll 1$, the radiation is emitted in a dipole pattern, with its zero at 90° to the direction of motion (figure 3.1a). On the other hand the emission from ultra-relativistic electron ($\gamma \gg 1$) is sharply and symmetrically peaked in a narrow cone towards the direction of the electron motion. with an opening angle of the order of $\sim \frac{1}{\gamma}$ i.e. 0.025 mrad for the SRS (figure 3.1b).

The radiation emitted is concentrated near the electron beam orbit with an infinitesimal length of the order of $\frac{R}{\gamma}$, where R is the radius of the curvature of the electron beam orbit. The electromagnetic wave irradiated from the synchrotron radiation is characterised by its electric field which is lying in the orbital plane and perpendicular to the direction of the radiation travel. as well as the magnetic field which is perpendicular to the orbital plane (Kulipanov et al 1977).

The most complete treatment of the radiation in the relativistic limit is obtained by Lorentz transformation. where the power generated by a radially accelerated electron. as deduced from Larmor's formula, must be invariant. The total instantaneous intensity radiated per unit solid angle per second into a bandwidth ($\frac{\Delta\lambda}{\lambda}$) may be obtained as a linear combination of the phase shifted ($\pm\frac{\pi}{2}$) intensity components, $I_\parallel$ and $I_\perp$, which are respectively the intensities of the radiation polarised perpendicular and parallel to the median plane of the electron orbit (see Kim 1984 and Kim 1986),

$$I = I_\parallel + I_\perp = \frac{3\alpha^2}{4\pi^2}\frac{I'}{e}\frac{\Delta\lambda}{\lambda}\gamma^2 y^2 (1 + X^2)\left[K^2_{2/3}(\xi) + \frac{X^2}{1 + X^2}K^2_{1/3}(\xi)\right] \qquad (3.3)$$

where α is the fine structure constant and I' the electron beam current, $X = \gamma\psi$

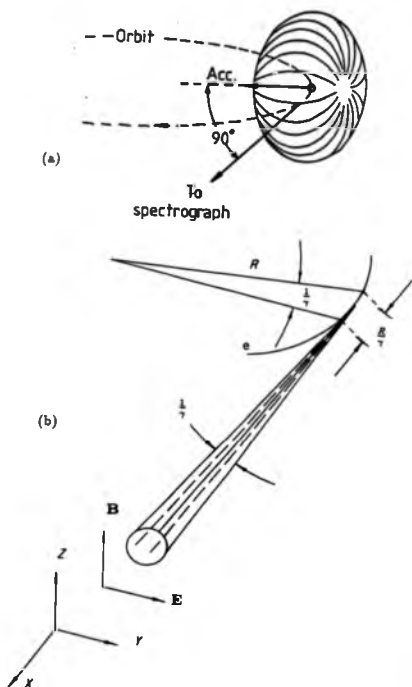**Figure 3.1**Synchrotron radiation emitted by (a) a non-relativistic electron traveling on a curved trajectory and (b) a relativistic electron traveling on a curved trajectory. The magnetic field, **B**, is perpendicular to the electron and the electric field **E** is parallel to the orbital plane and perpendicular to the radiation travel. $\psi = 1/\gamma$ is a natural opening angle in the vertical plane.

where ψ is the azimuthal angle of the beam. $y = (\frac{\lambda_c}{\lambda})$, $\lambda_c = 5.59R(m)/E^3(GeV)$ being the critical wavelength of the radiation for which half the power is generated below this wavelength and half is generated above ($\lambda_c = 3.88 Å$ for the main dipole 1.2 Tesla bending magnets and $\lambda_c = 0.93 Å$ for the wiggler at the SRS, E=2 GeV) and and $\xi = \frac{\lambda_c}{\lambda}(1 + X^2)^{3/2}/2$. K_ν is the modified Bessel function of the second kind of order ν.

The general behaviour of the angular distribution function is presented graphically, for the main dipole magnet as well as the high field (5.0 Tesla) wiggler at the SRS, in figure 3.2.

3.2.2 Properties of synchrotron radiation

The combination of a number of special properties of synchrotron radiation emitted from such an X-ray source, lead to a wide variety of scientific research. Those properties arising from an extremely stable source are basically governed by the total intensity emitted (discussed in the previous section) within a very narrow opening angle of the order of $\frac{1}{\gamma}$. This feature results mainly in obtaining extremely high concentrated flux which therefore may be focused on small experimental samples even at large distances away from the source. For example, in the X-ray region a maximum of 10^{13} *photons/s/mrad (horizontal) in 0.1% bandwidth*) is achievable and it is possible to focus this on a few (mm^2) of the sample area at the SRS. Moreover, due to the high concentrated flux, the synchrotron radiation which leaves the vacuum enclosure to travel along a single tangential port may be split by means of mirrors, perfect crystals and gratings to serve simultaneously more than one experimental station.
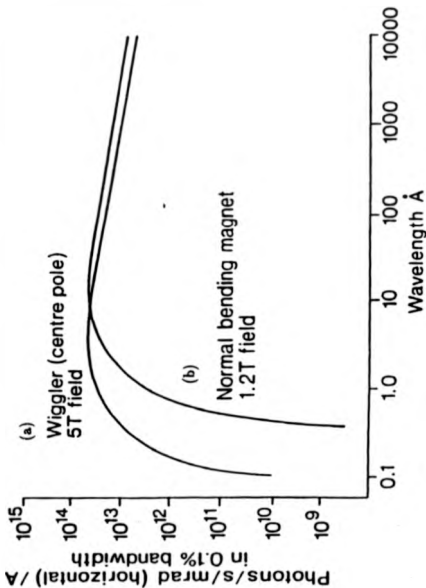
Figure 3.2 Spectral distribution of the SRS synchrotron radiation emitted by electrons traveling through (a) 1.2 Tesla dipole magnet and (b) 5.0 Tesla three pole wiggler.

The figure of merit for a number of experiments, which characterize the radiation is not the flux but the brightness or the brilliance which are defined respectively as:

$$Brightness = \frac{number\ of\ photons\ emitted/second}{(mrad)^2.(mm)^2\ into\ 0.1\%\ bandwidth} \tag{3.4}$$

$$Brilliance = \frac{number\ of\ photons\ emitted/second}{(mrad)^2\ into\ 0.1\%\ bandwidth}. \tag{3.5}$$

The source brightness which is defined as the emitted flux per unit source area per unit solid angle is directly dependent upon the electron beam emittance, in other words the size and the angular spread of the electron beam. The electron beam emittance which is dictated largely by the betatron oscillations, Pellegreni (1972), and commonly described by means of the positions and the angular divergence parameters in the vertical and the horizontal plane, respectively $(\sigma_x, \sigma_{x'})_v, (\sigma_y, \sigma_{y'})_h$. The knowledge of such parameters is very important for the calculation of the intensity of the flux and consequently the beam polarisation. Hence, for the SRS the average standard angular and position deviations for the bending magnets in the vertical plane were estimated at $\sigma_x = 0.16mm$ and $\sigma_{x'} = 0.04mrad$, whereas the same parameters may be considered in the horizontal plane. Beyond high collimated flux, however, synchrotron radiation is characterised also by its high linear polarisation in the orbital plane and becomes increasingly circular polarised away from the electron median plane. The degree of circular polarisation is an important quantity in the study of magnetism and is our main concern in this chapter. It will be discussed in detail later. Further important properties of synchrotron radiation such as the pulsed time structure and the tunability of the radiation are described and discussed

elsewhere (Tomboulian et al 1955, Jackson 1975 and Winick et al 1978).

3.2.3 Introduction to synchrotron machines

As far as the SRS is concerned, the synchrotron radiation is a three stage electron accelerator as it is shown schematically in figure 3.3. Firstly, the electrons are accelerated in a 12 MeV linear accelerator (Linac) which feeds to a 600 MeV Booster synchrotron. Secondly, the electrons are injected continuously into the storage ring for several minutes until the accumulation of a current of about 300 mA. After that, electrons with 2 GeV energy may obtained by supplying radio frequency energy as well as increasing the field in the dipole magnets. The ring was improved in 1986 by the introduction of better focusing magnets to provide the Higher Brightness Source with a smaller divergence. The emittance of the beam was consequently reduced by a factor of 14. Accordingly the average position and angular deviations of the electron distribution with respect to the median plane were improved and therefore, reduced respectively to 0.16mm and 0.04 mrad.

A single machine consists of a closed high vacuum chamber converging the beam through the different essential parts such as; bending magnets, wigglers, undulators, vacuum pumps and an rf cavity which is capable of replenishing the energy lost by the electron through the creation of photons. The 16 similar 1.2 Tesla bending magnets existing at the SRS bend the electrons into closed orbits, therefore, producing X-ray radiation by centrepetally accelerating them. Besides the dipole bending magnets existing at the SRS storage ring, which produce high energy radiation, a high field (5.0Tesla) wiggler is incorporated in a straight section of the ring with the object of producing high energy radiation (figure 3.4). The SRS wiggler is
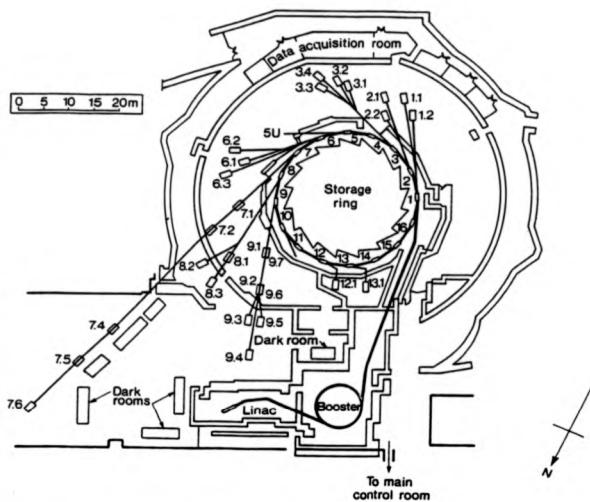
Figure 3.3 The layout of the SRS facilities.
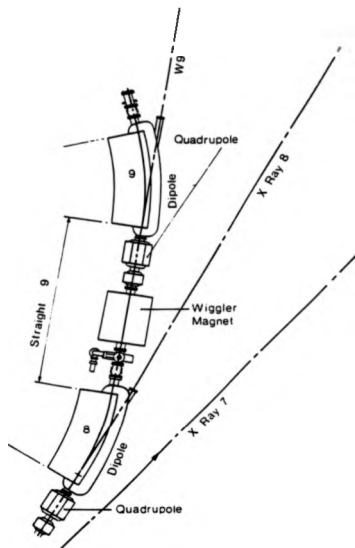
Figure 3.4 The layout of SRS machine straight 9, including the wiggler and the adjacent dipole magnets.

a three pole magnet which imposes a beam inflection in the electron orbital plane during its passage through two half peak field magnets (2.5 Tesla) and a peak of 5.0 Tesla in the centre magnet (see figure 3.5a). The trajectory of the electron as well as the variation in the vertical field through the wiggler are shown in figure 3.5b. At the X-ray topography wiggler line (W9.4) the radiation is emanating only from the central tangent point of the wiggler and therefore, the degree of circular polarisation was fortunately unaffected by the contamination of the emitted radiation from the up/downstream magnet radiation as well as the dipole magnets 8 and 9. The contributions to the power emitted from the central magnet is shown in figure 3.5c. Clearly the contributions are symmetrically distributed about the tangent point of the central magnet. The other insertion device which produce radiation is a so-called undulator which consists of a series of bending magnets mounted in a straight section along the electron path. The series of the magnets imposes an undulatory motion on the electron orbit, and therefore the total intensity emitted is almost equivalent to the sum of the intensities emitted by all the magnets constituting the undulator device.

3.2.4 Introduction to synchrotron polarisation

Studies of magnetism by means of magnetic scattering as well as magnetic diffraction has been well established (Platzman and Tzoar 1970, 1985). These techniques require, in most cases, an accurate knowledge of the radiation polarisation state for data interpretation. During the last couple of decades, circularly polarised radiation has been used for measurements of the spin dependent Compton profile (Sakai et al 1984, Mills 1987, Cooper et al 1986, 1988). Circularly polarised radiation may
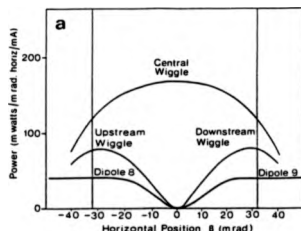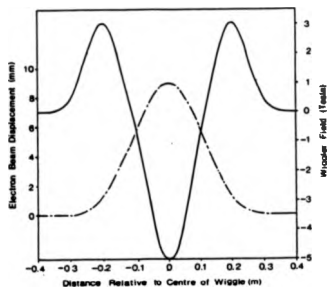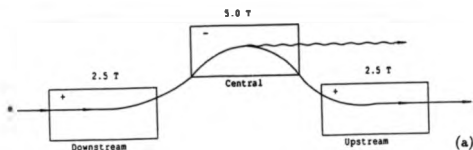
Figure 3.5 (a) Schematic diagram of the SRS three pole wiggler, viewed from the top, (b) the SRS wiggler field (solid line) and the electron beam trajectory (broken line) relative to the centre magnet (from Greaves et al 1983) and (c) Contributions to the power emitted into W9 from the wiggler magnet and the adjacent dipole magnets, 8 and 9.

be used also in the study of magnetic diffraction in magnetic substances. Recently, circularly polarised radiation was successfully introduced to measure spin dependent photoabsorption in ferromagnets (Schutz el al 1988, Collins et al 1989). In addition, linearly polarised radiation is also a major factor for the study of the anomalous scattering of X-rays. The interference between magnetic Bragg scattering and the charge scattering may occur when the periodicity of the spin lattice coincides with that of the chemical one.

Though Lipps et al (1954) derived the cross section for photon and electron polarisation coupling, Wheatly et al (1955) were the first to suggest the possibility of measuring the degree of circular polarisation by means of the spin dependent Compton scattering. Ten years later Bathow et al (1966) carried out the polarisation measurements by means of Compton scattering at photon energies from 15 to 300 keV as a function of electron energies at DESY in Hamburg. The technique was based on using two scintillation counters to detect separately the scattered photons polarised parallel to the orbital plane and the scattered photons polarised perpendicular to the orbital plane. Templeton et al (1988) calculated the polarisation of the synchrotron radiation at the SSRL wiggler line. They pointed out that the accurate knowledge of the degree of linear polarisation was required for the interpretation of their measurement carried out on the anomalous X-ray scattering effects. The polarisation of electromagnetic plane waves is dictated by the orientation as well as the amplitude of the electric and magnetic fields, i.e. a state of polarisation may be given by a relation between the amplitude and the phase of the two fields. As far as synchrotron radiation is concerned, the electric field is lying in the orbital plane and it is perpendicular to the tangent drawn from the source point and pointing

towards the radiation direction. whereas the magnetic field is perpendicular to the electron median plane (see figure 3.1). Hence, the radiation must be linearly polarised in the orbital plane and becomes increasingly elliptical away from the orbital plane. The radiation is symmetrically polarised below and above the orbital plane (i.e. left and right circular polarisation) because the direction of rotation of the radiation field vector coincides with the electron radiation direction seen from a point of observation located in the orbital plane along a tangent drawn to the electron trajectory.

Ideally, the radiation emitted by accelerated electrons would be 100% plane polarised in the orbital plane for non-divergent point sources. However the synchrotron radiation beam is around 95% plane polarised mainly due to the finite source size ($0.8mm^2$ for the SRS) as well as the betatron oscillations which are responsible for the polarisation smearing. This high polarisation in the median plane drops to about 75% of the total polarisation when it is integrated over all vertical angles. The degree of linear and circular polarisation can be expressed in terms of the intensity amplitudes of the beam in the two polarisation directions, which are parallel and perpendicular to the orbital plane.

$$P_L = \frac{I_\parallel - I_\perp}{I_\parallel + I_\perp} \tag{3.6}$$

$$P_C = \mp \frac{\sqrt{I_\parallel I_\perp}}{I_\parallel + I_\perp} \tag{3.7}$$

where the positive and the negative signs correspond to the left-hand and right-hand circularly polarised radiation.

The total degree of polarisation of synchrotron radiation, P_T, is well defined by

the general density matrix (equation 1.38) where the component P_L of the total polarisation is zero for synchrotron radiation. The total degree of polarisation, therefore, may be related to the linear and circular polarisation by the relation.

$$P_T{}^2 = P_C{}^2 + P_L{}^2 \tag{3.8}$$

3.3 Polarisation measurements

3.3.1 Introduction

The motivation for measuring the degree of circular polarisation of synchrotron radiation was the need to optimise the spin dependent Compton scattering experiments to be discussed in the next chapter. Principally, it is the intensity, not the magnetic Compton lineshape, that depends directly upon the degree of the circular polarisation. However, an accurate knowledge of the degree of circular polarisation of synchrotron radiation is required to optimise the spin dependent Compton scattering experiment. Further explanations about the Compton scattering experiment optimisation are described later in section 4.3.

The method applied, for the determination of the degree of circular polarisation, P_C, is governed by the first order differential Compton scattering cross section (equation 1.32). Clearly the equation consists of two terms: a charge scattering part and the spin dependent scattering part.

$$\frac{d\sigma}{d\Omega} = \underbrace{Z\frac{r_o{}^2}{2}[2 - \sin^2 o.(1 + P_L)]}_{(\text{荷})_c} + \underbrace{P_C\frac{r_o^2}{2}\mu.(1 - \cos\phi).\mathbf{S}[\mathbf{k}\cos\phi + \mathbf{k}']}_{(\text{荷})_m}, \tag{3.9}$$

where Z is the total number of electrons involved in the scattering atom and μ is the magnetic moment (Bohr magneton) of the ferromagnetic target, mounted in an applied magnetic field.

Clearly the cross section is a combination of two scattering cross section i.e. charge scattering cross section $\left(\frac{d\sigma}{d\Omega}\right)_c$ and spin dependent cross section $\left(\frac{d\sigma}{d\Omega}\right)_{sp}$. On one hand the charge scattering cross section quoted in equation 1.41 includes a small term which depends upon the degree of linear polarisation of the incident beam which becomes insignificant for backscattering. On the other hand the spin dependent cross section is proportional to the degree of the circular polarisation of the photon beam. Therefore, P_C may be calculated for the magnetic Compton backscattering arrangement where the uncertainties about the polarisation are less important than that of the charge scattering cross section.

Ideally the magnetic cross section (equation 3.9) is optimum when the applied field is chosen to be parallel anti-parallel to $(\mathbf{k}\cos\phi + \mathbf{k'})$. Under these circumstances the variation of the relative scattered intensity is given by,

$$\frac{\Delta I}{I} = \frac{I_{\downarrow} - I_{\uparrow}}{I_{\uparrow} + I_{\downarrow}}. \tag{3.10}$$

Using equation 3.9 and 3.10 we may obtain,

$$\frac{\Delta I}{I} = \frac{P_C \mu.(1 - \cos\phi).\mathbf{S}[(\mathbf{k}\cos\phi + \mathbf{k'}]}{Z[2 - \sin^2\phi(1 + p_L)]}. \tag{3.11}$$

The total polarisation of synchrotron radiation for a negligible emittance is very close to 100%, therefore the relation between the degree of circular and linear polarisation quoted in equation 3.8 may be approximated to $P_C{}^2 + P_L{}^2 = 1$.

The contribution of the magnetic scattering to the total scattering is very weak

(of the order of $\sim \frac{\hbar\omega}{m_ec^2}$, where $\hbar\omega$ is the photon energy, typically $\frac{m_ec^2}{10}$) (see equation 1.43). On the top of that the effect is even more reduced due to the relative small number of electrons with a net spin to the total number of electron involved in the charge scattering.

3.3.2 Experimental apparatus

All the spin dependent measurements were made at the Daresbury Laboratory SRS using a Compton scattering spectrometer described in detail elsewhere (Timms 1989). Partially circular polarised radiation may be obtained by means of the inclined view method. The apparatus assembly may be lowered and raised through the orbital plane by means of an adjustable baseplate. The spectrometer shown schematically in figure 3.6 was designed to satisfy the requirements of the spin dependent Compton scattering experiments. It consists mainly of three main parts. Firstly a monochromator plane single crystal mosaic Ge-220 was chosen in preference to Si crystal mainly due to the higher reflectivity. On the other hand the Ge-220 was chosen instead of the Ge-111, despite a higher reflectivity is obtained with the later monochromator, because of the wide range of the energy selection obtained from the 220 reflection. For instance an energy of 60 keV may be obtained with a Bragg angle of the order of 3.6° for the Ge-220, whereas the same energy is obtained only with a Bragg angle equivalent to 1.5° for the Ge-111. The monochromator may be mounted on a finely adjustable motor drives a goniometer. Secondly, the sample: the ferromagnetic crystal may be mounted between the pole pieces of the electromagnet. The faces of the magnet pole pieces were ground flat to ensure good contact with the samples and therefore ensure that samples would be fully
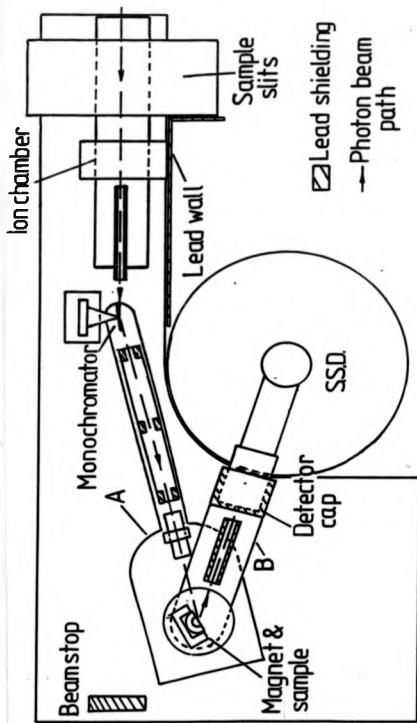
Figure 3.6 Schematic layout of the Compton Scattering spectrometer, viewed from the top.

magnetised. Moreover an extra pieces of spring steel material were used to hold and maintain the stability of the sample. The pole pieces were shaped in such a way to allow large scattering angle in the scattering by transmission (see figure 3.7). Sets of adjustable tungsten slits were placed in front of both the monochromator and the sample in order to collimate the beam and stop any scattering from the air and the shielding.

Although the magnet was designed mainly for measuring Compton scattering by transmission, it was deemed necessary to adopt the reflection geometry for the polarisation experiment for the main reason to obtain high count rate particularly away from the orbital plane (a schematic diagram of the experimental arrangement is shown in figure 3.8). Finally, a solid state germanium crystal detector (SSD) was used and accurately positioned to make a maximum practicable scattering angle of the order of $\sim 145°$, so that, the second term in Equation 3.9 is maximised.

3.3.3 Experimental techniques and measurements

The present experiments were performed at different positions above and below the orbital plane on the wiggler line (W9.4) at the Daresbury synchrotron radiation source (SRS). The station is situated at 37m from the source. According to equation 1.32 the magnetic effect in the Compton scattering increases with the photon energy. Accordingly the two energies chosen for the measurements were as high as practicable from this device (wiggler critical energy is only 14.4 keV).

The different parts of the spectrometer were first of all pre-aligned and positioned at approximately the height of the orbital plane using the laser beam which is pointing at the synchrotron emitting source. A white beam of 1mm high and 3mm wide
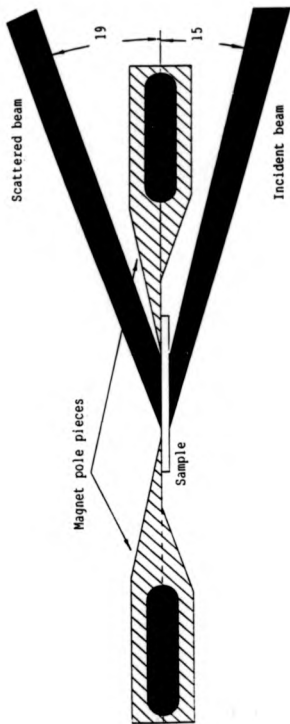
Figure 3.7 Electromagnet designed for scattering by transmission, viewed from above.
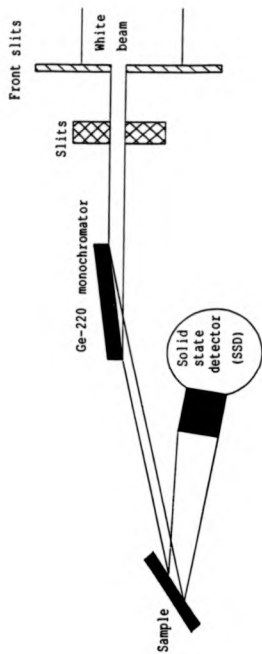
Figure 3.8 A schematic diagram of the experimental arrangement for the polarisation measurement.

was collimated by horizontally and vertically adjustable slits positioned in front of the monochromator. The width of the monochromatic beam was virtually dictated by the length of the monochromator due to the small selected Bragg angles ($\sim 3°$). The incident monochromatic photon energies selected from the first order Bragg reflection of an 80mm long Ge-220 monochromator were 53.8keV and 63.9keV. The monochromated beam impinged upon a long saturated rectangular parallelepiped polycrystalline iron sample ($30 \times 10 \times 2mm$) mounted between the widely open pole pieces of the electromagnet. where the face of the sample was oriented to make a small angle of $15°$ with the incident beam in the horizontal plane to maximise the term $\mathbf{S}.(\mathbf{k}\cos\phi + \mathbf{k}')$. The scattered radiation is detected by a solid state detector through a scattering angle of $140°$. chosen as high as practicable for the apparatus in order to obtain high magnetic effect by maximising the factor ($1 - \cos\phi$) in equation 3.9. The detector was calibrated with a low activity source ($10\mu Ci$ ^{241}Am). The high dead time ($\sim 20\%$) in the analogue to digital converter (ADC) resulting from the high count rate (close to the orbital plane) detected by the solid state detector was reduced firstly by an assembly of aluminum foils placed in front of the detector and secondly, by reducing the shaping time of the detector amplifier to $2\mu s$ compared to $6\mu s$ used for gamma ray Compton scattering. This degrades the spectral resolution, but that is unimportant for measurements of total intensity.

A series of 12 measurements were made for each incident energy at different position above and below the orbital plane. Each of these measurements lasted until a sufficient number of integrated counts accumulated under the Compton profile. At positions close to the orbital plane. the measurements were taken for about 30min, whereas at positions far away from the median plane the measurements lasted for

up to 120min due to the sharply decreased flux. The orbital plane position was checked after each machine refill because the median plane of the electron orbit may be subjected to slight vertical movements. Between two refills, movements of up to $\mp 1.5mm$ were found (see figure 3.9). Moreover, the stability of the beam was continuously checked and readily assessed by monitoring the incident beam flux by means of an ion-chamber during each run. The intensity of the incident beam was displayed graphically. The fluctuations in the intensity due to the beam movements were very significant off-axis because of the rapid intensity drop away from the median plane (see figure 3.10).

The energy spectra were recorded by a computer-based CANBERRA multi-channel analyzer (MCA). The magnetic field direction in the sample was reversed every 5 seconds and spin up and spin down data stored in different memory locations. The short counting time ensured that the difference data were completely unaffected over a long period of time from the source decay and small fluctuations of the beam intensity. The magnetic field was switched and controlled accordingly by the same computer. The integrated counts over the Compton profile showed a residual fractional magnetic effect of the order of $\sim 1\%$ above the orbital plane which was in agreement with the estimation based on equation 3.9 for energy of the order of $(60keV)$. The magnetic electrons present only 8% of the total atomic number of electrons in iron. The disappearance of the fluorescent lines, (K_α, K_β) located at low energy, in the difference spectra emphasised the cancellation of the systematic errors in the data.
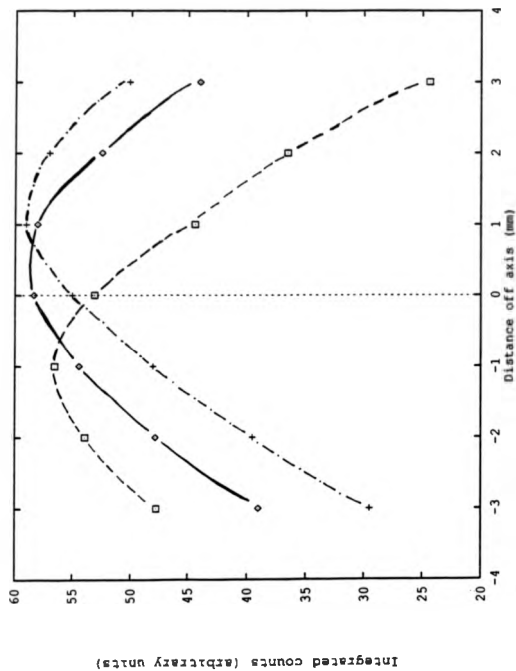
Figure 3.9 Experimental curves which show the variation of the position of the orbital plane for different refills.

Distance off axis (mm)

Integrated counts (arbitrary units)
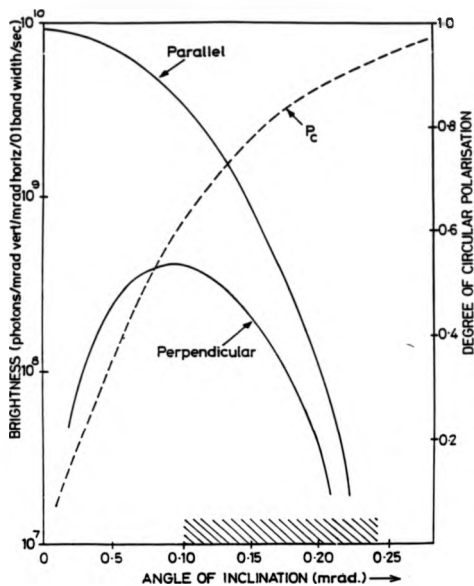
Figure 3.10 The corresponding variations in the degree of circular polarisation P_C and the SR intensity with azimuthal angle for $0.1\mathring{A}$ incident wavelength (from Holt and Cooper 1983).

3.3.4 Data processing

The degree of circular polarisation of synchrotron radiation may be accurately deduced from the relative variation of the flux $\frac{dN}{N}$. Clearly an absorption correction is unnecessary: the effect in the ratio is self consoling (see equation 3.11). The data were therefore subject to correction for the energy variation of the charge and the magnetic scattering cross section. The magnetic electrons which originate predominantly from the 3d orbitals are well included in the region of interest for which the data are considered, i.e. the profile due to the 3d electrons which lies on a peripheral orbits is peaked around the origin of the total Compton profile, whereas the profile which originates from the charge scattering is very broad, due to the highly Doppler shifted electrons which are lying deeply in the atom, hence not all 26 electrons were included in the region of interest. The fractional number of electrons responsible for the charge scattering were accurately estimated according to the well established prediction of the core electron of free atom (Biggs et al 1975). Accordingly, only 22.84 electrons out of the total number of (26) were found to be contributing in the charge scattering within the range $(-8.0a.u., 8.0a.u..)$. Part of those omitted electrons (K-shell electrons) were included in the region of interest but not possibly exited due the energy transfer which is smaller than the binding energy of those electrons (K-edge threshold energy = 7.112keV).

The degree of circular polarisation was finally deduced after the data was subject to a multiple scattering correction. Sakai (1987) investigated in detail the effect of the multiple scattering for the magnetic Compton scattering and came to the conclusion that because the spin dependent scattering cross section changes its sign

at scattering angles at $\phi = \pi/2$. the double magnetic Compton scattering is largely self-canceling. This is not true for the charge scattering when the multiple scattering is always additive. The ratio defining the difference spectrum to the sum spectrum for spin-up and spin-down may be given by,

$$
\begin{aligned}
\frac{\Delta I}{I} &= \frac{(single)_{mag} + (multip)_{mag}}{(multip)_{charge} + (single)_{charge}} \\
&= K \frac{(single)_{mag}}{(single)_{charge}}.
\end{aligned} \tag{3.12}
$$

where K is the rescaling factor which originates from the multiple scattering,

$$
K = \frac{1 - (multip)_{mag}/(single)_{mag}}{1 - (multip)_{charge}/(single)_{charge}} \tag{3.13}
$$

Sakai (1987) reported in his calculation that the integrated intensity ratio of the magnetic multiple scattering to the magnetic single scattering $(multip)_{mag}/(single)_{mag}$ is of the order $\sim 3.8\%$ for similar experimental conditions as those reported here. On the other hand the multiple scattering effect to the single scattering ratio $(multip)_{charge}/(single)_{charge}$ has been computed here using a Monte Carlo simulation and estimated to be 11.8%. According to those values the scaling factor K due the multiple scattering is therefore estimated to be 0.93, which shows that the effect of the multiple scattering over the region of interest (-8.0, 8.0 a.u.) was around 7%.

3.3.5 Results and Discussion

A typical spectrum from the spin-up orientation as well as the difference spectra recorded respectively at the positions of 0mm ($\psi = 0mrads$) i.e. at the orbital plane and 8mm ($\psi = 0.21mrads$) above the orbital plane are shown in figures 3.11
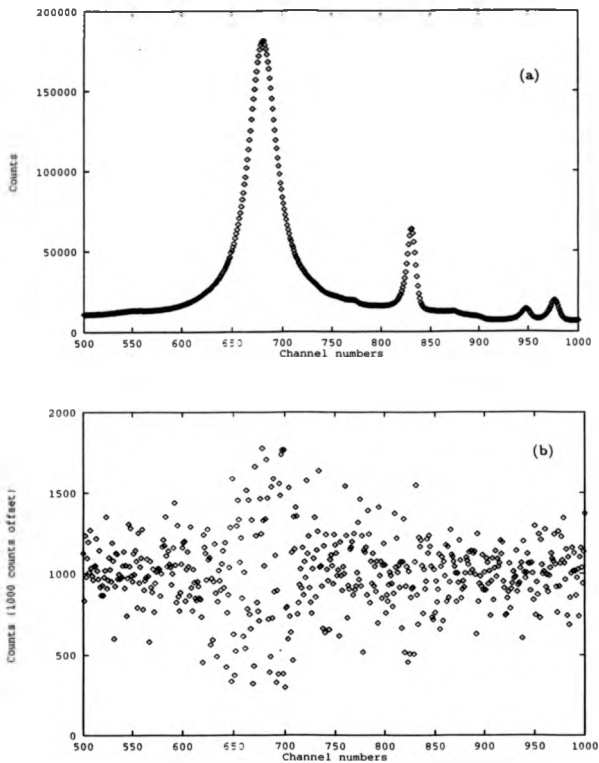
Figure 3.11 Spectra obtained at azimuthal angle $\psi = 0mrad$ from (a) spin up distribution and (b) the difference between spin up and spin down.
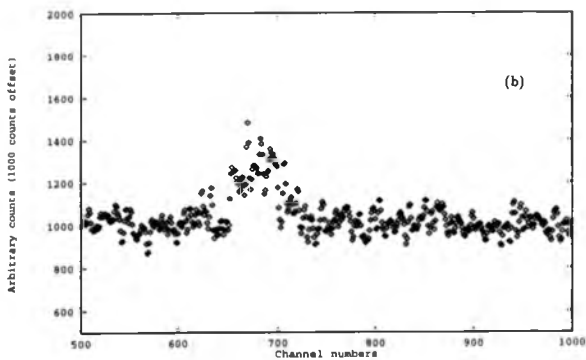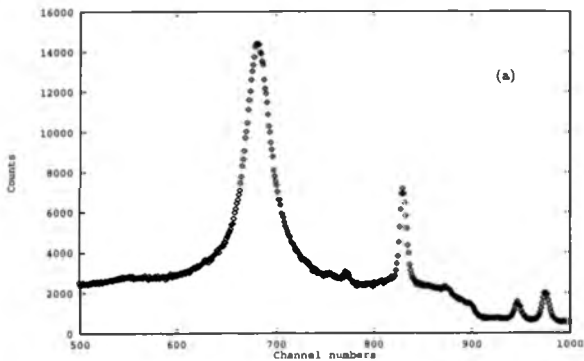
Figure 3.12 Spectra obtained at azimuthal angle $\psi = 0.21 mrad$ from (a) spin up distribution and (b) the difference between spin up and spin down.

and 3.12. It is clear that the magnetic effect is absent in the orbital plane whereas a significant residual effect is apparent above the orbital plane. Again the difference spectra is clearly a sensitive test to the cancellation of the systematic errors. As it has been mentioned earlier the data were considered completely clear of such errors because of the disappearance of the fluorescent lines (see Collins et al 1990).

The accompanying figures 3.13a and 3.13b show the good agreement of the data with the calculation performed recently by Laundy (1990). The theoretical predictions for ideal electron orbits (Schwinger 1949) are strongly affected by different parameters mainly arising from the source emittance. However the polarisation may be reduced due to the linear and perpendicular distributions of the electron motion around the source point. Hence, the horizontal and the vertical intensity components of the beam polarisation (Kim 1986) must be modified accordingly.

Though the interpretation of the Compton line shape does not depend directly upon the value of P_C, the complete understanding of the beam polarisation is still a major factor in optimising the performance of the experiment. In addition, other experiments such as magnetic diffraction and magnetic photoabsorption studies require knowledge of the degree of circular polarisation for complete interpretation.

The measurements of the degree of circular polarisation were performed at high energies, though the experiments depending directly on P_C (mentioned above) usually take place at low energies (5-10 keV), because the possibility of examining the Compton scattering peak obtained from low energy elastic line is virtually impossible. Since high energy is a critical test, therefore, the degree of circular polarisation which is well described at high energy (50-60 keV), will be better described at low energy (5-10 keV). As a consequence, the estimation of the degree of circular polari-
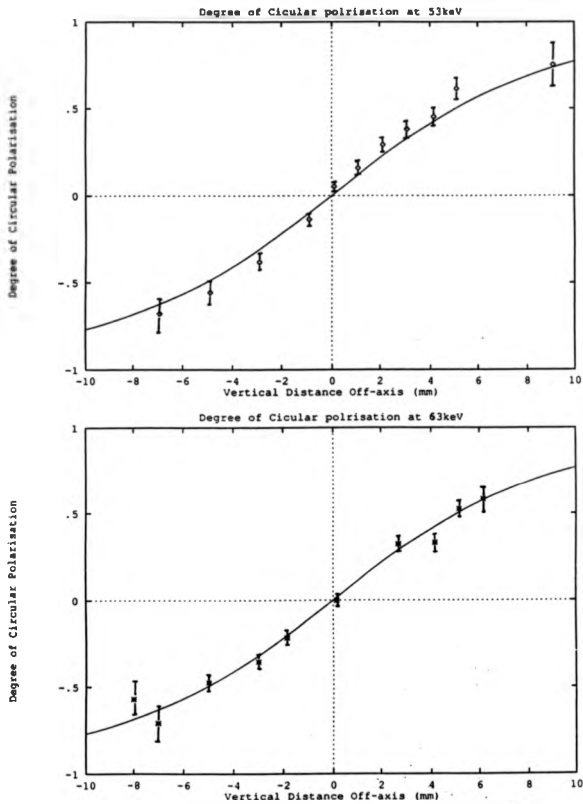
Figure 3.13 Comparison between the variation of the measured and the calculated degree of circular polarisation as a function of azimuthal angle (a) at 53.8 keV and (b) at 63.9 keV.

sation of synchrotron radiation obtained from dipole magnets may be deduced from the calculation performed by Laundy (1990).

Chapter 4

MAGNETIC COMPTON PROFILE OF GADOLINIUM AND NICKEL

4.1 Introduction to magnetic Compton scattering

The existence of electron spin terms in the photon scattering cross section was established four decades ago when Lipps et al (1954) discussed theoretically the scattering cross section for polarised X-rays.

The second order magnetic term which was identified in equation 1.32 is real for real polarisation. It is commonly know as the pure magnetic scattering term; it contributes insignificantly to the charge scattering term, i.e. $\sim (\frac{\hbar\omega}{mc^2})^2$ of the charge term (see Brunel et al 1981, 1983). For magnetic transition metals where only 10% or less of the atomic electrons give a net magnetic contribution, the pure magnetic scattering cross section is typically of the order of $\sim 10^{-3}$ comparative to the charge scattering cross section for conventional X-rays. De Bergevin and Brunel (1972) were the first to observe such an effect using unpolarised radiation from a 1 kw X-ray tube. The observed two superlattice X-ray diffraction peaks from

anti-ferromagnetic NiO disappeared above the Néel point. The magnetic superlattice reflections are completely distinguished from the ordinary charge peaks. The Compton scattering is not sensitive to anti-ferromagnetism (i.e. no information is provided with such a technique since coherent scattering sums the magnetisation). On the other hand, information may be obtained with the same technique but carried out on ferromagnets (i.e. a net spin contribution to the Compton profile is obtained from the summed magnetisation).

As has been discussed in section 1.5, Platzman and Tzoar (1970) extended the theory of the Compton scattering (regardless of the pure magnetic scattering term), and established for the first time a method of isolating an unpaired spin distribution in ferromagnets from a spinless distribution, commonly known as the electron momentum density distribution within the Born approximation and the framework of the impulse approximation. The Compton scattering cross section for circularly polarised X-rays for a magnetic system with a spin (s) and negligible contribution from orbital moment may be obtained as,

$$
\begin{aligned}
\frac{d\sigma^2}{d\Omega d\omega} = \; & \frac{1}{2}\left(\frac{e^2}{mc^2}\right)\frac{\omega_2}{\omega_1}\left((1+cos^2\phi).J(p_z)\right. \\
& \left. + P_C\frac{2\hbar\omega_1}{mc^2}(1-cos\phi)\; S(\mathbf{K})(\mathbf{k}cos\phi + \mathbf{k}').J_{mag}(p_z)\right)
\end{aligned}
\tag{4.1}
$$

where $J_{mag}(p_z)$ is commonly referred to as the spin dependent Compton profile, given as,

$$
J_{mag}(p_z) = \int_{p_x}\int_{p_z}(n_\uparrow - n_\downarrow)dp_y dp_x
\tag{4.2}
$$

where $n_\uparrow$ and $n_\downarrow$ are the electron densities with spin up and spin down respectively.

4.1.1 General introduction to previous research

The first measurements of spin dependent Compton profiles were carried out on polycrystalline iron by Sakai et al (1976, 1977). The experiments were performed using 122keV circularly polarised gamma ray obtained from cryogenically oriented radioactive source of ^{57}Co. The source was cooled down to about 40mK. The emitted radiation was characterised by a small degree of circular polarisation ($P_C = 0.3$) along the magnetisation field direction. Statistically, the experiment was very poor due to the self heating effect imposed by the radiation on the radioactive isotope. A similar experiment was later carried out using the same technique but a different radioactive source (^{191}Ir) (see Sakai et al 1984). The energy provided was of the same order (129keV), whereas the degree of circular polarisation was significantly higher ($P_C = 0.8$). Moreover, the source activity obtained was four times as high as that obtained from the ^{57}Co (i.e 0.40 mCi).

Holt et al (1983) suggested the use of a synchrotron radiation source for the study of the Compton scattering (partially circular polarised beam may be obtained fractionally below or above the orbital plane). Subsequently, the first measurement using the inclined view method was performed by Holt et al (1985) at the SRS. Despite the very poor statistical accuracy of the data, the quantitative agreement with the APW calculation (Wakoh et al 1977) confirmed the feasibility of such a method for the study of the magnetic effects in magnetic substances. The method was later pioneered by Cooper et al (1986). A central dip at the origin was apparent in the data for the first time. The statistical accuracy was sufficient to establish the central dip and revealed a significant difference between the experiment and the

APW band theory (i.e. the s-p negative polarisation was underestimated by the calculation).

Mills (1987) adopted a different technique to produce circularly polarised radiation. Circularly polarised radiation was obtained from a predominantly linearly polarised synchrotron radiation emitted from CHESS, using an X-ray phase plate. Polycrystalline Fe, Ni and Co were measured and a similar magnetic profiles to those reported earlier were reproduced. More measurements of a better statistical accuracy particularly on polycrystalline iron were repeatedly produced (Sakai et al 1987 and Timms et al 1988). Recently Cooper et al (1988) measured for the first time the directional Compton profile of iron using 60keV CPSR. Further measurements of an improved statistical accuracy (Collins et al 1989) enabled to confirm the discrepancy predicted at low momenta by the electron band theory (APW) particularly along the 100 direction. More recently Sakai et al (1989) adopted the same technique used by Cooper et al (1988) to measure the directional Compton profiles of iron using the newly installed wiggler at the 6.5GeV storage ring at TRISTAN complex in Japan. Similar profiles to those reported by Collins et al (1990) were reproduced.

4.2 Spin-orbit separation

The complete study of the photon scattering cross section (see equation 1.32) has been well established for a long time. The first order contributions arise from the charge term and the interference magnetic term. The interference term consists of the electron spin scattering as well as the orbital scattering. The orbital term contributes negligibly in most magnetic substances to the spin dependent Compton

scattering, particularly because of the common experimental arrangement usually adopted for such investigation (i.e. backscattering arrangement). In contrast with the neutron scattering, where spin and orbital terms are not separable because neutrons are only scattered by virtue of the magnetic moment, photon scattering permits the separation due to charge interactions, spin interactions and orbital interactions which arise from the electric and the magnetic fields of the electromagnetic wave,

$$\frac{d\sigma^2}{d\Omega d\omega} = \frac{1}{2}\left(\frac{e^2}{mc^2}\right) P_C \left(\frac{\hbar\omega_1}{mc^2}\right)(1-\cos\phi)\left[S(\mathbf{K})(\mathbf{k}\cos\phi + \mathbf{k}') + L(\mathbf{K})(\mathbf{k}+\mathbf{k}')\cos^2\phi/2\right].$$
(4.3)

Clearly from equation 4.3, the observation of spin and orbital scattering terms may be distinguished separately in a Compton scattering experiment by choosing the correct scattering geometry. Specifically, there is the case where spin and orbital densities are aligned together in the scattering plane $(\mathbf{k}, \mathbf{k}')$ and oriented in such a way to make an angle (α) with the incident wavevector $\mathbf{k}$ (see figure 4.1). The orbital component may be eliminated for scattering angles close to 180° or by aligning the vector $(\mathbf{k} + \mathbf{k}')$ to be perpendicular to the magnetisation direction. Clearly, the backscattering (i.e. scattering angles close to 180°) is the most favourable arrangement since the spin scattering term may be maximised at the same time (see equation 4.3). On the other hand the optimisation of the orbital term and the elimination of the spin scattering term combined together is a very complicated arrangement to achieve. Assuming the incident beam makes an angle α with the magnetisation direction as stated in figure 4.1, therefore, for elastic scattering obtained in the transmission arrangement, the spin scattering term is eliminated when $(\tan \alpha = 2 \cot \phi)$ (see figure 4.2). However the orbital scattering term may be
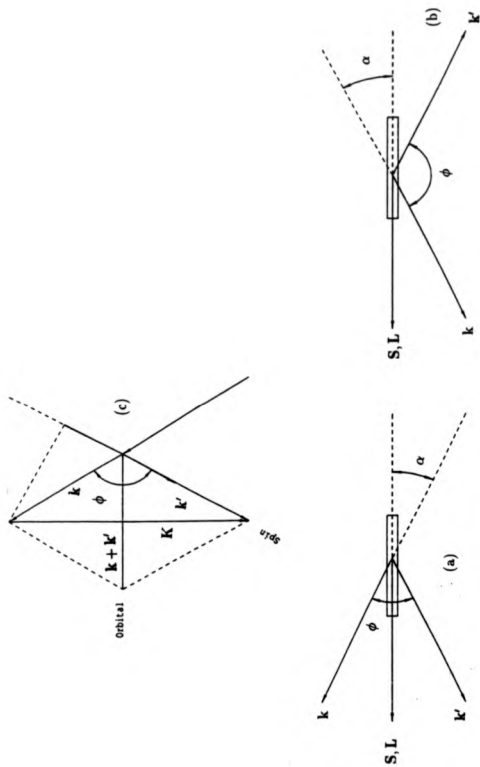
Figure 4.1 The geometry of scattering experiment (a) in transmission and (b) in reflection. (c) represents the possible geometry for separating spin and orbital contributions to magnetisation.
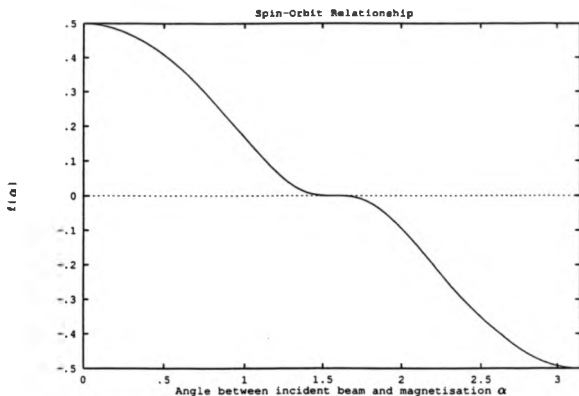
Figure 4.2 Figure of merit for optimization of spin term and orbital term, deduced from the relationship between the scattering angle ϕ and the angle between the incident beam and the magnetisation α.

maximised accordingly when $(f(\alpha) = [\cos\alpha + \cos(\alpha + \phi)]\cos(\phi/2)^2)$ is a maximum. For such considerations, the optimum scattering arrangement may be obtained for $\alpha = 0°$, hence $\phi = 90°$ (see figure 4.2). In the case of inelastic scattering, the spin dependent term drops to zero and changes sign with respect to the charge scattering for angle α given as,

$$\tan\alpha = -\frac{E + E'}{E'}\cot\phi. \tag{4.4}$$

Recently Collins et al (1989) measured the variation of the total magnetisation for scattering angle of 90°, as a function of the angle between the incident beam and sample magnetisation (α), (see figure 4.3). The flipping ratio in cobalt was also measured. The spin and the orbital moment are assumed to be collinear with the total moment.

4.3 Compton scattering optimisation

It is well established and clearly understood from the study of synchrotron radiation (chapter 3) that the degree of circular polarisation increases strongly on moving out of the orbital plane (i.e. by increasing the azimuthal angle ψ of the beam), whereas at the same time the flux decreases rapidly from a maximum value at the orbital plane to almost zero fractionally off axis (see figure 3.10). Accordingly, the study of magnetism by means of Compton scattering using synchrotron radiation is a relatively slow process because of the difficulty of obtaining circular polarised radiation with sufficient intensity.

Since fully circular polarised radiation is not necessary for the interpretation of the lineshape of the Compton profile, therefore, an optimum point between the
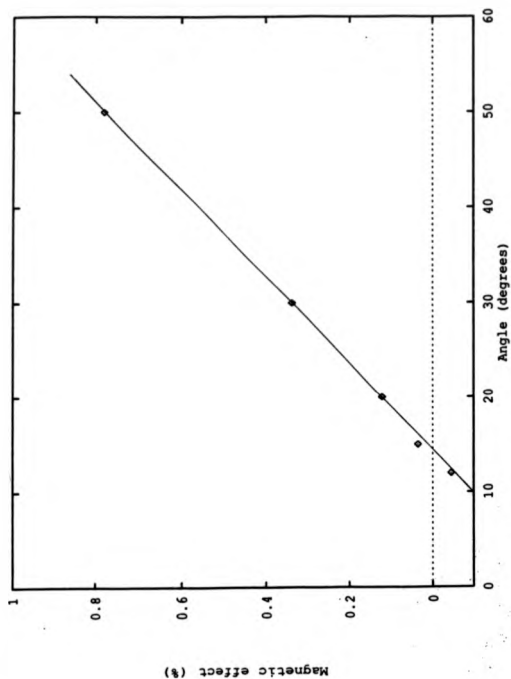
Figure 4.3 The measured fractional magnetic effect L/S in the ferromagnet iron plotted against the angle made between the incident beam and the magnetisation direction. The solid line is a linear least square fit (Collins et al 1990).

degree of circular polarisation and the rapidly decreasing flux is necessary to obtain the best possible quality data with limited beam time. The main objective for the Compton scattering optimisation is governed by the improvement of the statistical accuracy as well as optimising the magnetic effect at the same time. The magnetic effect in nickel ferromagnet is of the order of 2% and 12% for gadolinium ferromagnet. Under those circumstances the important quantity which needs to be optimised is (*magnetic signal/Compton noise*). This figure of merit, which was first pointed out by Sakai, may be easily obtained according to equation 3.9 and is given as,

$$\frac{magnetic\ signal}{Compton\ noise} \propto \frac{I P_C}{\sqrt{I}} \tag{4.5}$$

where I is the scattered intensity for one spin direction and P_C is the degree of circular polarisation,

$$P_C \propto \frac{I_\uparrow - I_\downarrow}{I} \tag{4.6}$$

Substituting 4.6 into 4.5 one may obtain,

$$\frac{magnetic\ signal}{Compton\ noise} \propto \frac{I_\uparrow - I_\downarrow}{\sqrt{I}} \tag{4.7}$$

The ratio increases critically with the increase of energy. Unfortunately synchrotron radiation intensity drops dramatically as the energy increases above E_c.

Preliminary investigations for optimising the ratio were simply performed by measuring the count rate over the region of interest at the Compton profile for different vertical positions above the orbital plane for energies ranging from 40 to 80keV. The optimum position was found to be within the range of 0.10-0.24 mrad above or below the orbital plane. Principally, it was not possible to find precisely the exact position due to the size of the beam cross section ($5 \times 1mm^2$). The

large vertical width of the beam was necessary to obtain enough counts under the Compton profile . However. a specific calculation carried out by Laundy (1989) for the SRS wiggler W9.4 line. taking into consideration the different parameters of the finite electron source such as the electron beam emittance. The calculation predicted an optimum position at an azimuthal angle of 0.14 mrad below or above the electron median plane. The predictions are illustrated graphically in figure 4.4. Clearly the optimum energy required for the nickel experiment is within the range 55-60 keV.

4.4   Geometrical broadening

It is well understood from gamma-ray Compton profile studies that the theory must be smeared out with the experimental resolution before being compared with the experimental data in order to allow for the effect of finite spectrometer resolution. The total resolution is well established to be a combination of the detector resolution and the geometrical broadening resolution due to the scattered beam divergence. The total experimental resolution in itself is a delicate problem to solve accurately because of its complexity. Moreover because the resolution is so poor, various assumptions can confidently be made, i.e. the detector resolution and the beam divergence are assumed to be Gaussians. hence. the total resolution may be approximated as,

$$\Delta P_{tot}^2 = \Delta P_{det}^2 + \Delta P_{geom}^2 \tag{4.8}$$

where ΔP_{det} is the detector resolution function (FWHM) and ΔP_{geom} is the geometrical broadening effect.

The geometrical broadening was assumed to be significant only for the scattered
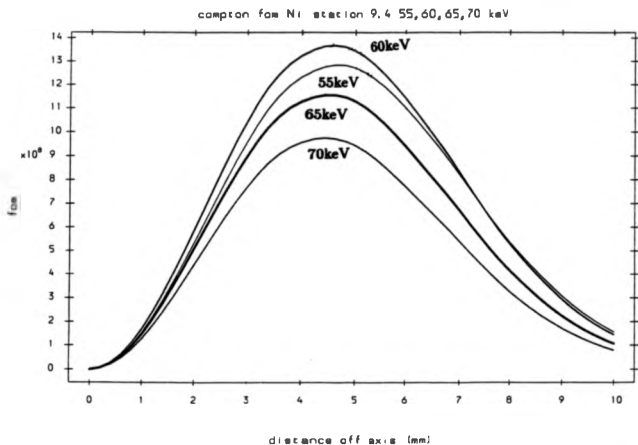
Figure 4.4 The figure of merit (fom $\equiv$ *Flux* $\times$ *Energy* $\times$ P_C $\times$ *absorption*) calculated by Laundy (private communication) for nickel sample.

beam because the divergence of the incident monochromatic beam obtained from the crystal monochromator was assumed to be negligible. Therefore the differentiation of equation 1.12 with respect to the scattered photon energy and the scattering angle may be obtained as,

$$\Delta P_{geom} = \frac{mc}{2\omega_1}\Delta\omega_2 + \frac{\omega_1 sin\phi}{4c}\Delta\phi. \tag{4.9}$$

where $\Delta\omega_2$ may be derived from equation 1.9 to be,

$$\Delta\omega_2 = \frac{\omega_1^2 sin\phi}{mc^2}\Delta\phi \tag{4.10}$$

Therefore, expression 4.9 may be approximated for backscattering as follows,

$$\Delta P_{geom} = \frac{3}{4}\frac{mc}{4mc^2}\omega_1 sin\phi\Delta\phi \tag{4.11}$$

where $\Delta\phi \sim \frac{d}{l}$ (d being the diameter of the detector and l sample-detector distance).

It is often desirable in the study of Compton scattering to have a higher experimental resolution for the data interpretation. However, it is impracticable to have a high experimental resolution as well as improving the statistical accuracy mainly because of the limited beam time.

4.5 Gadolinium

4.5.1 Introduction

Gadolinium was the fourth ferromagnetic element to be discovered in nature (see Urbain et al 1935). The element is distinguished from transition metals firstly by its Curie point of around room temperature (293.2K) and secondly by its large number of 4f unpaired electrons (7), which give rise to magnetism. Although gadolinium is considered to be relatively simple in terms of magnetic structure with respect to

ferromagnet transition metals, it differs from them by virtue of its strong spin-orbit coupling. In addition, the exchange field derived from the localised 4f electrons is very distinct from that of conduction electrons. Moon et al (1972) carried out a neutron diffraction experiment on gadolinium in order to measure its magnetic moment distribution. According to their result, a good agreement between the form factor and the shape of the spin distribution was obtained at large scattering angles which explains the perfect description around that region from the 4f electrons. However, a significant disagreement at small scattering angles was observed between the data and the 4f form factor (i.e. total magnetic moment of $7.0\mu_B$). The disagreement was featured by a change of slope at around Fermi level. They conclusively pointed out that the unpaired spin density sensed by the neutron diffraction consists of a localised 4f part and a diffuse part due to the polarisation density of the unpaired conduction electrons. The excess in the magnetic moment per gadolinium atom was experimentally deduced in polycrystalline sample to be $0.55\mu_B$, (see Nigh et al 1963). This excess is attributed to the polarisation of the conduction band electrons by the localised 4f electrons by means of the exchange interaction.

Most spin dependent Compton scattering has been carried out on transition metals and particularly iron due to its simplicity (i.e iron is an easy material to magnetise and it is possible to measure the magnetic Compton profile of iron at room temperature. Moreover, it has a relatively high magnetic moment). The first attempt at measuring a rare earth gadolinium ferromagnet was done by Mills (1987) using circularly polarised X-ray produced from an X-ray phase plate at the Cornell High Energy Synchrotron Source (CHESS). Recently Itoh (private communication) performed a similar experiment using circularly polarised gamma-ray radiation ob-

tained from a cryogenically oriented radioactive source.

4.5.2 Description of the experimental system

A schematic diagram of the experimental arrangement for gadolinium Compton scattering is shown in figure 4.5. Since the Curie temperature for gadolinium is very close to room temperature, it was necessary to cool the sample as low as possible below Curie point in order to line spin up and the spin down states in the ferromagnetic phase. As a result a cooling system was incorporated into the Compton scattering spectrometer described earlier in the study of synchrotron polarisation. The method of cooling the sample consisted of blowing nitrogen gas, passed through liquid nitrogen stored in a large dewar, onto the sample and the magnet insulated in a polystyrene box.

4.5.3 The cooling system

In the cooling process many materials have been tested for their quality of insulating the sample and the magnet. Different investigations carried out, lead successfully to the construction of a small box made of polystyrene material. Preliminary investigations showed that the building up of ice on the sample and the surface of the box was negligible.

The box was made as small as practicable in order to minimise the volume of the cooled environment, i.e. for such arrangement, very low temperature may be achieved with small quantities of nitrogen gas. The thickness of the polystyrene box walls was 6mm. The beam attenuation through the polystyrene material was measured using a small radioactive calibration source of americium ^{241}Am. A neg-
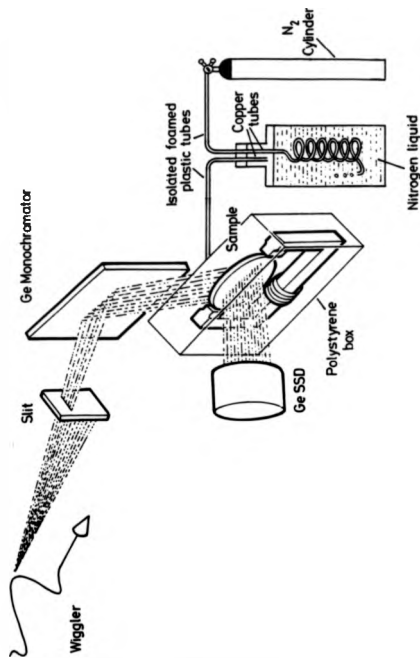
Figure 4.5 Schematic diagram of the experimental arrangement for the measurements

of the Compton profile of gadolinium, including the cooling system.

ligible absorption rate was measured to be 1% and 0.5% respectively for 26.36keV
and 59.54keV

The warm nitrogen gas stored in the cylinder was firstly blown through a foamed
plastic tube connected to a coiled cooper pipe immersed in liquid nitrogen stored in
a large dewar. The idea of bubbling nitrogen gas by passage through liquid nitrogen
had two objectives: both cooled nitrogen gas blown from the cylinder and evaporated
nitrogen contributed to the cooling process. This method was effective enough to
obtain temperatures of around $-100°C$. The boiling point of liquid nitrogen is at
77.3K (i.e. $-195.8°C$)

4.5.4 Magnetisation of gadolinium

It is well established that the study of the spin dependent Compton profile is only
possible when the target is fully magnetised. Accordingly, cooling the gadolinium
foil below the Curie point was necessary to obtain ferromagnet material (Curie
point, T_c is known as the temperature above which the spontaneous magnetisation
vanishes and therefore separates the disordered paramagnetic phase ($T < T_c$) from
the ordered ferromagnetic phase ($T > T_c$)). The magnetic dipoles are originally
oriented randomly in the paramagnetic phase. The significance of temperature in
such a material is governed by the fact that the orienting effect due to magnetic
interactions is highly opposed by thermal agitation. As a result, the spin order is
destroyed when the temperature increases.

Nigh (1963) studied the magnetisation of gadolinium as a function of temper-
ature. It was shown that the easy direction of the magnetisation varies as the
temperature increases: at $4.2°K$ the easy direction is oriented about 30° from the

0001 axis. As the temperature increases to around $160°K$, the magnetisation vector tends to lay on the basal plane, whereas it becomes parallel to the 0001 axis at $270°K$.

The spontaneous magnetisation of gadolinium was studied by Nigh et al (1963) for zero external magnetic field at different temperatures. The magnetisation is estimated to be around 70% at $200°K$. It is conceivable from our point of view that the alignment of spins of the same character may be easily achievable with an external magnetic field produced from a highly saturated electromagnet (2500 turns of 0.5mm insulated copper around the core of the magnet). In addition, preliminary investigation dealing with the magnetisation saturation was carried out at different temperatures (*room temperature.* $0°C$, $-30°C$ *and* $-70°C$) using a small coil fitted around the gadolinium foil in order to measure the current induced in the coil as a function of the current in the ferromagnet coil. Clearly from the curves (figure 4.6), the saturation was achieved at $-70°c$ with an induced current $I > 0.4$ Ampere.

4.5.5 Spectrum analysis and data reduction

The present experiment was carried out at the topography station using the wiggler beam line W9.4 (see Brahmia et al 1988). The same inclined view technique as that reported for the polarisation measurements was adopted here as well . The apparatus was elevated 6mm above the orbital plane (i.e. an azimuthal angle of the order of 0.15 mrad), in order to obtain a circularly polarised radiation with $P_C = 0.6$. A white beam was collimated with finely adjustable slits of a vertical gap of 4mm and a horizontal gap of 5mm. The same Ge-220 monochromator was used to select photon energy at 46.3 keV, i.e. the monochromator was tuned to a
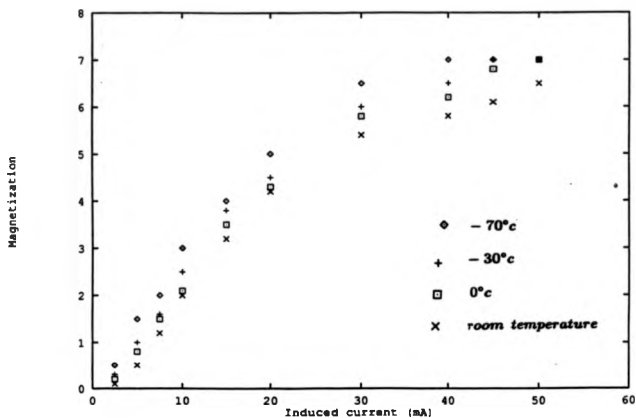
Figure 4.6 Curves describing the magnetisation saturation in gadolinium at different temperatures (*room temperature*, 0°C −30°c *and* −70°C).

Bragg angle of 3.7°. It is clearly evident that the energy selected in this particular Compton experiment is well below the Compton scattering optimum energy at the SRS wiggler line W9.4 (55-60 keV). The main reason for that was to avoid the overlap of the Compton scattering profile with the gadolinium fluorescent lines (K_{β_1} and K_{β_2}) respectively located at 50.38keV and 49.97keV, and therefore may increase the uncertainty of the magnetic effect. The K_{α_1} and the K_{α_2} located at 42.99kev and 42.31keV, respectively. do not present any kind of problem since it does not interfere with the profile at all.

Although the transmission arrangement is originally proposed only for the anisotropic studies of the Compton profile due to simplicity (i.e. the possibility of aligning the magnetisation and the scattering vector is easily achieved, see section 4.6.3). The experimental arrangement for the measurement of isotropic gadolinium was adopted by transmission also mainly because absorption was insignificant (i.e. negligible absorption in the thin foil $\sim 0.025mm$). The scattering beam was detected through a 149° scattering angle by a 10mm crystal germanium solid state detector. The large scattering angle obtained for this experimental set up was due to the long gadolinium foil which dictated the widely opened gap between the magnet pole pieces. The magnetic field was reversed at 10 and 20 seconds intervals in an asynchronous period of 80 seconds controlled by a BBC microcomputer. The combination of the magnetic field provided by the electromagnet and the reasonable low temperature was effective enough to saturate the gadolinium foil. The sample temperature was measured continuously throughout the experiment by means of a calibrated nickel-chrome/ nickel-aluminum thermocouple connected to a voltmeter, which enabled the temperature to be calculated.

The data were recorded for two spin directions in separate memories in the first and the second quarter of an Ortec 4096-multichannel analyzer (Cooper et al 1986). The sum and the difference profile was computed and memorised in the third and the fourth quarters. Typical spectrum for the spin up orientation as well as the difference spectrum are shown in figure 4.7. Some 10^6 and 10^4 integrated counts were accumulated respectively under each magnetisation direction Compton profile and the difference Compton profile in a measurement period of 15 hours. Therefore an expected magnetic effect of the order of 1.2% was obtained (equation 4.1).

Though the degree of the circular polarisation of synchrotron radiation on the wiggler line at the SRS was accurately predicted, its knowledge is not particularly important in the data reduction because the area of the profile is normalised to the total moment. A simple calculation was initially used to reduce the low energy tail of the detector response function. The spin dependent data (i.e. the difference profile) were first of all corrected from the beam attenuation in the specimen despite the thin thickness of the foil (0.025mm) because the experiment was set up in such a way that the incident beam impinged onto the sample with a small angle ($\sim 15°$). Therefore, the beam may penetrate into the sample by up to ($\frac{0.025}{\sin 15} \sim 0.1mm$) in the direction of the incident beam. The difference data were corrected for the energy variation of the magnetic cross section (equation 1.51) across the region of interest, then transformed into momentum scale according to equation 1.12. The data were averaged in momentum intervals and normalised in the region (-8.0a.u., +8.0a.u.) to the number of Bohr magneton ($7.55\mu_B$) and averaged left/right to yield the final spin dependent Compton profile. According to Sakai (1987) (see section 3.3.4), a multiple scattering correction was unnecessary for the magnetic data, especially with
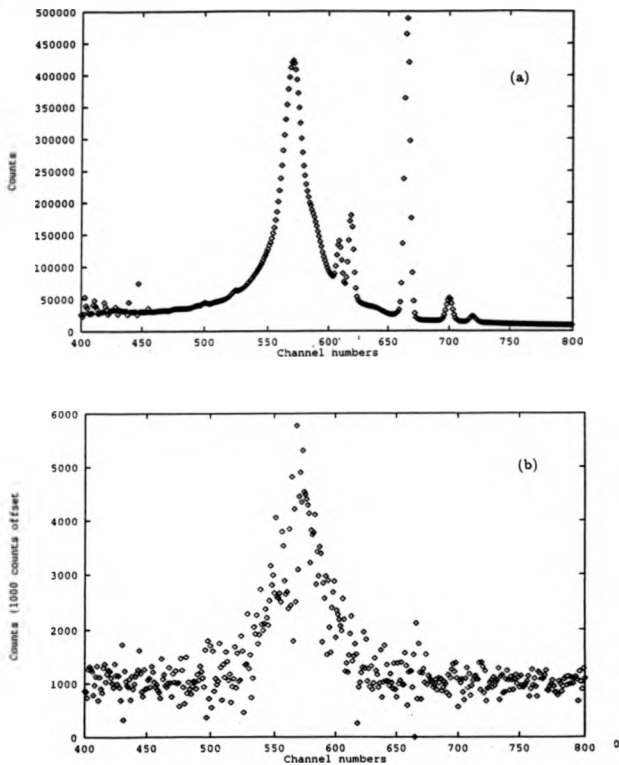
Figure 4.7 Compton profile spectra of gadolinium; (a) the total profile from spin up orientation and (b) the magnetic difference profile.

such a thin sample.

4.5.6 Results and discussion

The final processed spin dependent Compton profile of gadolinium is shown in figure 4.8. The original data compared with the calculated profile obtained from the 4f electrons (see Biggs et al 1975) shows a significant disagreement at low momenta below Fermi level. This discrepancy explains that the experimental spin dependent Compton profile data may not be adequately described by the magnetic profile from the 4f electrons at low momentum. In the absence of any theoretical calculation of the spin dependent Compton profile of gadolinium, the data were compared with a simple model based on equation 2.1. The model consists of a superposition of the Compton profile originating from the seven highly bound unpaired 4f electrons with magnetic moment of $7\mu_B$, obtained from Biggs et al (1975), and a free electron component originating from the conduction electrons ($6s^25d$) with a magnetic moment equivalent to $0.55\mu_B$. This 7.5% increase in the magnetic moment represents an increased estimate of the polarisation due to the diffused conductions electrons which are particularly important in the calculation of the energy bands.

Though the model is not efficient enough to describe accurately the data particularly around the Fermi momentum (i.e. electron-electron correlation effects are not taken into account), it still a very good approximation for the description of the polarised conduction electrons. The reasonable accuracy of the model is governed by the fact that the magnetic 4f shell lies well inside the atom i.e. the 4f band is about 6 eV below the bottom of the conduction electrons band (Roeland 1975). Hence, the 4f electrons have a very small and negligible overlapping with the 4f
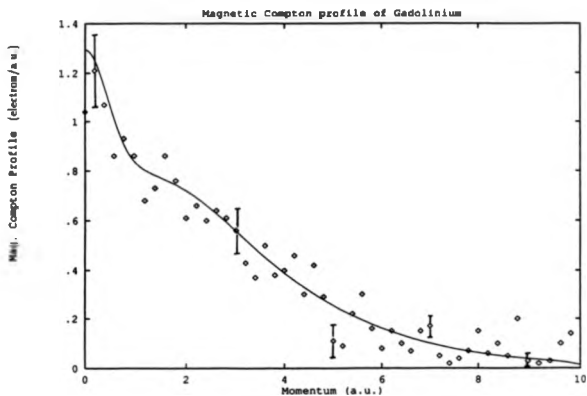
Figure 4.8 Comparison of the experimental spin dependent Compton profile of gadolinium (o) with the core + free free electron model (solid line) calculated numerically from Biggs et at (1975). The model has been convoluted with a Gaussian of FWHM=0.7 a.u. corresponding to the experimental resolution.

shells of the neighbouring ions, therefore, the only significant exchange interaction occurs between the magnetic 4f electrons and the conduction electrons.

Finally, it is important to mention that the small peak obtained below Fermi momentum was not apparent in the earlier measurements by Mills (1986) and recently Itoh (private communication) because of the relatively poor statistical quality of data. Moreover, a qualitative agreement of this simple model with the profile especially at low momenta must be statistically strengthen in the future.

4.6 Nickel

4.6.1 Origin of magnetism in nickel

Metallic systems involving d- and f-orbitals in the conduction band such as transition metals and rare earths, present a problem of a different character than other simple metals. For instance, the s-p like electrons existing in those metals usually exhibit nearly free electron behaviour, featured by the hybridisation with d- and f-states. As far as transition metals are concerned, the ferromagnetism is predominantly generated by the spin exchange between the nearest magnetic atoms or ions, due to the overlapping orbits of the magnetic 3d electrons. The lineshape of the spin dependent Compton profile may be very sensitive to the partial contributions to spin polarisation of the synchrotron radiation components as well as the mixed s/p hybrid electrons (figure 4.9) especially below Fermi level where the hybridisation may occur. Accordingly the spin dependent Compton profile lineshape is significantly modified at low momenta (below Fermi level) producing a dip at the centre of the profile because of the negative polarisation of the s-p-like electrons which are characterised
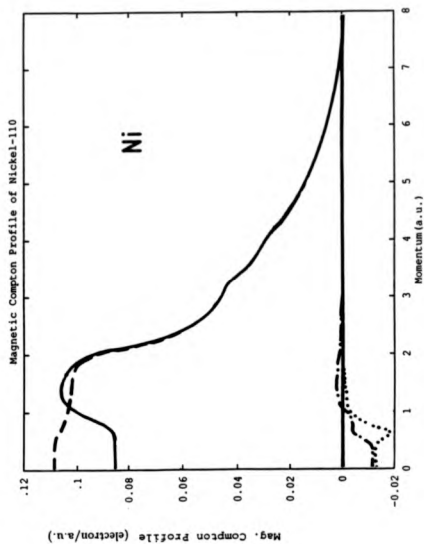
Figure 4.9 The partial contributions to the magnetic Compton profile of nickel from the 3d dashed lines, core (dotted line) and s/p hybrid electrons (dot/dashed line). The total distribution is indicated by the solid line (see Rennert et al 1983).

by the excess of the minority spin electrons in that particular region. Principally, the negative magnetisation occurs at small energies because the majority spin band lies deeper than the minority spin band below the Fermi level.

The directional spin dependent Compton profiles of nickel were calculated by Rennert (1983) using the combined interpolation scheme (CIS). The number of electrons for the majority band and the minority spin band were estimated to be $n^\uparrow = 5.28$ and $n^\downarrow = 4.72$ respectively. Hence, the total polarisation of nickel metal, $n^\uparrow - n^\downarrow$, which corresponds to the total magnetic moment is $0.56\mu_B$ which is consistent with the measured value (see Danan et al 1968). The total negative polarisation for s-electrons and p-electrons was estimated from the calculated partial densities to be $(-0.021\mu_B)$. The largest part was attributed to the p-like electrons $(-0.018\mu_B)$, whereas the s-like electrons represent only $(-0.003\mu_B)$.

Recently the band structure of nickel was treated by the full potential linearized augmented plane wave method (see Kubo and Asano 1990). The exchange splitting from s and p states was estimated to about $0.02eV$. The calculated magnetic moment $(0.58\mu_B)$ is slightly higher than that predicted by the CIS method. the negative polarisation for the s-p electrons was estimated to about $0.047\mu_B$ which is twice that predicted by the CIS calculation.

4.6.2 Sample preparation

The complete treatment of the Compton profile of any crystalline material is achieved by investigating the effect along as many crystallographic directions as possible. However, it is always possible to describe the magnetic Compton scattering effect along three major crystallographic orientations as (100, 110, 111) in the cubic sys-

tems. One of the most important features of the measurements of the Compton profile of cubic systems by transmission is illustrated in the use of a single sample oriented along the 110 direction. It is clear from figure 4.10 that the three major orientations may be found in the same plane, parallel to the face (110).

The orientation of the randomly oriented cylinder was first of all determined by means of the Laue method. then oriented along the (110) direction by rotation using a goniometer with two degrees of freedom. The (110) nickel single crystal was cut carefully by a spark erosion method from a randomly oriented cylinder purchased from Cambridge Metal Crystal Ltd. The shape of the sample was not particularly important for this experiment. however, the thickness was dedicated by the optimum Compton scattering intensity.

$$I_c = I_0 \int_v e^{-\mu_1 x} \mu_c e^{-\mu_2 y} dv \tag{4.12}$$

where $dv = S \frac{dl'}{\sin \alpha}$, (S is the beam cross section), $x = \frac{l'}{\sin \alpha}$, $y = \frac{l-l'}{\sin \alpha}$, and μ_1 and μ_2 are respectively the absorption coefficients of the sample material for the incident and the scattered beams. and μ_c is the Compton scattering absorption coefficient which is assumed to be constant and independent of the integral. The integrated Compton intensity may be obtained by integrating the intensity through the sample thickness,

$$I_c = \frac{I_0 S \mu_c \sin\beta}{\mu_1 \sin\beta - \mu_2 \sin\alpha} \left(e^{\frac{-\mu_2 t}{\sin\beta}} - e^{\frac{-\mu_1 t}{\sin\alpha}} \right) \tag{4.13}$$

where α and β are respectively the angles made by the sample face with the incident and the scattered beam as stated in figure 2.7. According to the previous equation,
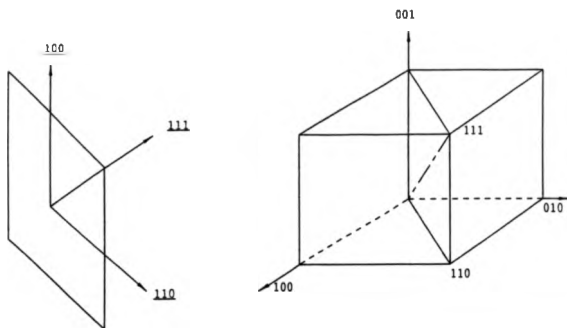
Figure 4.10 A diagram which shows that a single crystal wafer oriented with the sample face perpendicular to the 110 crystallographic axis, includes the three major crystallographic orientations in the same plane parallel to the face.

the optimum thickness may be derived as,

$$t_{opt} = \frac{1}{\frac{\mu_1}{\sin\alpha} - \frac{\mu_2}{\sin\beta}} ln \left(\frac{\mu_1 \sin\beta}{\mu_2 \sin\alpha} \right) \tag{4.14}$$

According to the previous equation, the nickel sample was cut then ground flat to a thickness of 0.20mm.

4.6.3 Experimental details

A schematic diagram of the experimental arrangement for directional magnetic Compton scattering is shown in figure 4.11. As with the synchrotron radiation polarisation measurement, this experiment was carried out in transmission. A white beam was collimated by adjustable tungsten slits 4.5mm wide and 4mm high. The same Ge-220 monochromator was used to select a beam of energy 55.3 keV; i.e the monochromator was tuned to 3.1° Bragg angle. The photons were scattered through a scattering angle of 145° in transmission through a 110 magnetised nickel single crystal slice 0.20mm thick. A backscattering transmission geometry was chosen for two reasons: firstly, an alignment of the scattered vector **K** with the magnetisation direction is easily achieved with thin samples mounted adequately between the magnet poles. Secondly, it is possible for a cubic single crystal such as Fe and Ni, to find the three major crystallographic orientations i.e. (100, 110, 111) lying in the same plane when the sample face is oriented along 110 (see figure 4.10). The complete magnetisation of nickel was easily achieved with the ferromagnet due to its low magnetisation saturation $(0.0481T.cm^{-1})$ compared to iron which is almost factor of four higher $(0.1714T cm^{-1})$.

The energy spectra for spin-up and spin-down were recorded with a computer
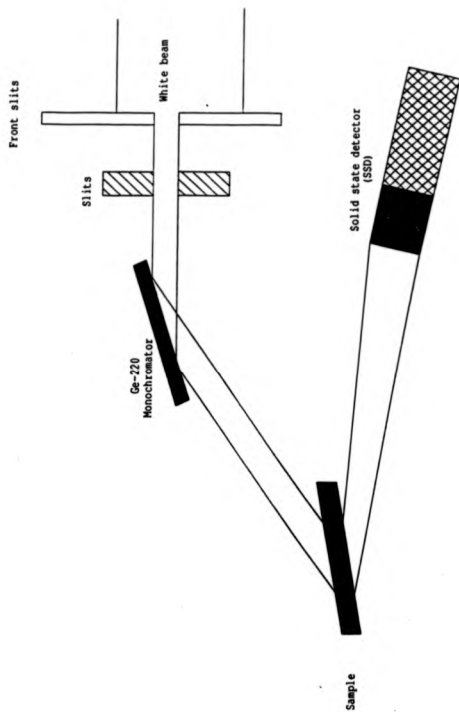
Figure 4.11 Schematic diagram of the experimental arrangement for the magnetic Compton scattering of nickel obtained in transmission.

based Canberra MCA. The magnetic field was reversed every 5 seconds in order to ensure that the data were completely unaffected from the source decay. Approximately 8×10^7 and 6×10^7 integrated counts were accumulated under each spin direction Compton profile and the difference profile over a period of 25 hours for each sample directions during the 6 days of measurements. The short beam time allocated for this measurements was not long enough to cover all three major orientations (100, 110, 111) with sufficient statistical accuracy due to the very small magnetic effect governed by the small magnetic moment ($0.58\mu_B$). As a result the spin dependent Compton profile was measured for only two crystallographic orientations (111, 100).

4.6.4 Results and Discussion

The directional Compton profiles of a single nickel crystal are tabulated in table 4.1 and shown in figure 4.12 (see Timms et al 1990). The data is compared to the APW calculation (Wakoh et al 1977) and the FLAPW calculation (Kubo and Asano 1990). The statistical accuracy of the data is not as good as that of iron (Cooper et al 1988) because of the small magnetic moment of nickel (i.e. the measurement time needed to achieve the same quality data as iron is estimated to be 4 times greater). The profiles are characterised by a central dip as was the case for iron. The dip originates from the negative polarisation of the s-p conduction electron states i.e. the spin density of the minority band is larger than that of the majority band. The 100 profile presents a larger dip than the 111 profile. Clearly the APW theory fails to predict the 111 spin dependent Compton profile. The theory does not show the dip obtained by the experiment. Similar discrepancies were obtained with the iron data

p_a	Exp 100	FLAPW 100	APW 100	FLPAW 110	APW 110	Exp 111	FLAPW 111	APW 111
0.0	0.049	0.06725	0.0517	0.05747	0.0606	0.066	0.08401	0.1023
0.2	0.066	0.06958	0.0561	0.06360	0.0684	0.690	0.08224	0.0992
0.4	0.056	0.07426	0.0656	0.07758	0.0856	0.062	0.07868	0.0923
0.6	0.065	0.07891	0.0752	0.09010	0.0999	0.081	0.07734	0.0869
0.8	0.077	0.08455	0.0845	0.09557	0.1040	0.078	0.08063	0.0858
1.0	0.093	0.09152	0.0939	0.09605	0.1006	0.087	0.08778	0.0891
1.2	0.091	0.09769	0.1019	0.09620	0.0963	0.097	0.09644	0.0952
1.4	0.104	0.10182	0.1079	0.09756	0.0950	0.102	0.10313	0.0999
1.6	0.098	0.10386	0.1118	0.09934	0.0965	0.071	0.10472	0.1004
1.8	0.110	0.10162	0.1106	0.09976	0.0977	0.095	0.10065	0.0957
2.0	0.091	0.09277	0.1010	0.09532	0.0935	0.085	0.09213	0.0869
2.2	0.090	0.07999	0.0862	0.08432	0.0819	0.079	0.08146	0.0762
2.4	0.085	0.06917	0.0733	0.07049	0.0673	0.071	0.07125	0.0662
2.6	0.079	0.06276	0.0655	0.05900	0.0556	0.059	0.06253	0.0581
2.8	0.068	0.05804	0.0598	0.05190	0.0489	0.059	0.05525	0.0515
3.0	0.051	0.05192	0.0522	0.04872	0.0463	0.064	0.04898	0.0461
3.5	0.035	0.03599	0.0351	0.03563	0.0381	0.031	0.03339	0.0341
4.0	0.014	0.02767	0.0257	0.02284	0.0219	0.037	0.02541	0.0247
4.5	0.012	0.01753	0.0172	0.01956	0.0192	0.014	0.01708	0.0174
5.0	0.011	0.01301	0.0122	0.01367	0.0145	0.014	0.01347	0.0119
5.5	0.009	0.00851		0.00745		0.007	0.00850	
6.0	0.012	0.00618		0.00744		0.006	0.00615	
6.5	0.008	0.00400		0.00317		0.005	0.00395	
7.0	0.008	0.00270		0.00256		0.002	0.00288	
7.5	0.004	0.00138		0.00181		0.006	0.00151	
8.0	0.004	0.00059		0.00048		0.003	0.00068	

Table 4.1 Experimental spin dependent Compton profiles of Ni for 100 and 111 directions. Also tabulated are the FLAPW and the APW calculations. The theories have been convoluted with the corresponding experimental resolution function of FWHM=0.7a.u.
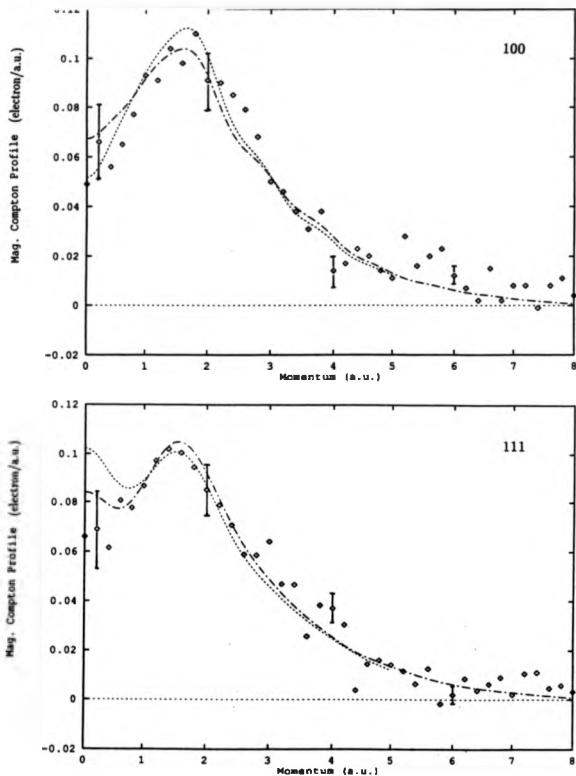
Figure 4.12 Comparison of the spin dependent Compton profile of nickel obtained experimentally (◦) with the APW calculation (dotted line) and the FLAPW (dashed line). The theories have been convoluted with the experimental resolution function which had a FWHM≈0.7 a.u.

particularly with the 100 direction. The APW calculation which was based on the
state dependent potential in the band structure is not adequate to describe the mag-
netic Compton profile, particularly at low momenta (i.e. negative spin polarisation
of p-like electrons is not well represented by the APW). The Combined Interpolation
Scheme (CIS) calculation by Rennert et al (1983) presents similar discrepancies due
to the underestimation of the s-p negative polarisation. This underestimation may
be attributed to the insufficient number of both four orthogonalised plane waves and
only 70 reciprocal lattice vectors are used in the calculation.

In order to remove the discrepancies in the negative polarisation of the s-p
electrons for iron and nickel, Kubo et al (1989) reconsidered the previous theo-
ries (Wakoh et al 1977, Rennert et al 1983, Poulter et al 1988 and Genoud et al
1989) using the full potential linearized augmented plane wave theory basing the
calculation on the local spin density approximation (LSDA). The energy values and
wavefunctions are calculated in $\frac{1}{48}$ of the Brillouin zone for each spin state. The
spin dependent momentum density distributions were determined to be 893 recip-
rocal lattice vectors whereas the spin momentum density distributions contributed
by the core states were determined from free atom wavefunctions. The predicted
directional magnetic Compton profile are in an excellent agreement with the mea-
sured spin dependent Compton profile of iron (see figure 4.13). In the case of iron
the calculation was based on lowering the centre of gravity of p-states in the third
minority band in order to reproduce correctly the hole pocket at points N at the
Brillouin zone. The band structure obtained by the FLAPW method revealed an
exchange splitting of predominantly s and p states of around $0.2eV$. The negative
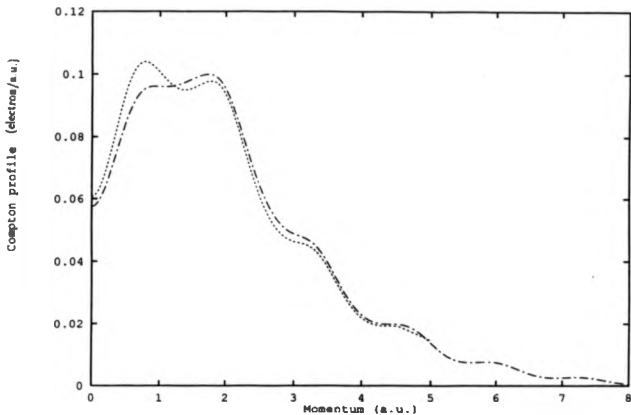polarisation obtained at low momenta was attributed firstly to the negative polari-

Figure 4.13 Comparison of the theoretical 110 spin dependent Compton profile of nickel obtained with the APW calculation (dotted line) and the FLAPW calculation (dashed line). Both theories have been convoluted with the experimental resolution function which had a FWHM=0.7 a.u.

sation of s-like electrons and secondly to the negative polarisation of p-like electrons from the second to fourth band.

As far as nickel is concerned the FLAPW describes the experimental data much more accurately than the APW theory particularly the 111 profile. A slight difference is noticeable in the 100 profile where the depth of the central dip is underestimated. This failure may be attributed to the nonlocal potential due to the electron-electron correlation effects. Sunderarajan et al (1990) also failed to describe the spin dependent momentum density distribution in ferromagnetic nickel using the self consistent spin polarised linear combination of Gaussian orbitals.

More recently, the directional Compton profiles of nickel were measured by Sakai et al (1989). Due to the small magnetic moment of nickel ($0.58\mu_B$), which caused major problems in the past in order to achieve data with sufficient statistical accuracy, Sakai et al (1989) adopted a similar technique to that reported here but significantly increased the count rate by resorting to using a focusing monochromator and multi SSD system combining thirteen Ge crystals. In this case, thirteen different spectra can be accumulated using thirteen different apparatus. Simultaneously the assembly of all spectra provides an important count rate (see table 4.2). The magnetic Compton profiles obtained were similar to those reported here within the experimental error.

As a conclusion one may say that the FLAPW method gave a very satisfactory picture in describing the nickel band structure. However the effect of the nonlocal potential due to electron-electron correlations must thoroughly be investigated in the future in order to resolve completely the problem. On the other hand a better experimental resolution and higher statistical accuracy of the data are necessary to

Reference	P_C	Ferromagnet	Energy (keV)	$(I_\uparrow - I_\downarrow)/0.1$a.u.	Time (s)
Sakai et al (76)	0.3	Fe	122	0.6×10^3	139
Sakai et al (83)	0.8	Fe	129	1.3×10^4	165
Holt et al (86)	0.5	Fe	33.7	3×10^3	8
Cooper et al (86)	0.6	Fe	46.4	5.0×10^4	16
Sakai et al (87)	0.6	Fe	129	2.5×10^4	594
Cooper et al (88)	0.6	Fe	60	1.1×10^4	24
Sakia et al (89)	0.6	Fe	60	6.2×10^3	11
Brahmia et al (88)	0.6	Gd	46.3	0.9×10^4	15
Present	0.6	Ni	55.3	1.2×10^4	25
Sakai et al (89)	0.6	Fe	60	2.2×10^5	1

Table 4.2 Comparison of count rates of spin dependent Compton profile measurements on ferromagnets.

give a clear view of the theory.

Chapter 5

THEORY OF MAGNETIC XANES

5.1 Introduction to X-ray absorption

The electronic structure of atoms is well established according to quantum theory of solids (Faulkner 1982). The study of the behaviour of electrons gives detailed information about many different physical quantities carried by electrons such as the spin moment which gives rise to magnetism (Weiss 1907). Moreover, information about physical quantities related to electrons via existing interactions in solids such as forces which bind atoms together may also be obtained.

In studying X-ray absorption, practically all interest is concentrated in the investigation dealing with the behaviour of the excited electrons during the process. The core electron behaviour may be understood easily since these electrons behave as in free atoms. This is due to the fact that core electrons are very tightly bound to the nucleus, hence the potential created by the neighbouring electrons is weak to a point that it is considered negligible with respect to the nuclear potential. In addition to the core electrons, the low energy outer electrons, are considered as free electron like.

As a result the crystal potential may be considered a fairly weak perturbation with respect to those electrons. Moreover, their states are approximated by plane waves, which are well known to be only weakly scattered by atoms. The crystal potential is strongly affected by valence electrons because of their capability of binding the whole system together and particularly determine its electronic structure (Grobman 1975).

The process of X-ray absorption leads the absorption cross section having sharp steps as the energy increases through each shell threshold (Brown and Winick 1980). The resulting spectrum describing the absorption cross section against energy (see figure 5.1) falls into three major parts as far as X-ray spectroscopy is concerned. Firstly, the pre-edge region or the threshold is the range lying just below the absorption edge which gives information about the binding energies as well as quantitative information. Secondly, the region which extends to about 50 keV above the edge is known as the near edge region or the X-ray absorption near edge structure (XANES). Thirdly, the next region is called the extended X-ray absorption fine structure (EXAFS). It is well known to be an accurate investigative tool for the determination of the interatomic distances as well as the structural information of the nearby scattering atoms.

The advent of intense tunable X-ray sources such as synchrotron radiation have made extended photoabsorption studies into a variety of fields namely; biological systems, condensed matter etc.... Greaves (1981), Munoz (1983) and Bianconi (1983). As far as condensed matter is concerned, the description of X-ray spectra originating from the absorption of photons by electrons in atoms, particularly core electrons, is characterised by the eigenstates of electrons before and after being excited. These
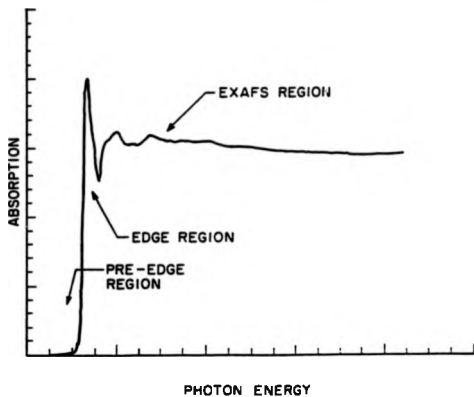
PHOTON ENERGY

Figure 5.1 A schematic illustration of the x-ray absorption spectrum showing the threshold region (including pre-edge and edge regions) and the EXAFS region.

eigenstates fall mainly into three different classes which are, in order of increasing energy, the core states, the valence states and finally the high energy excited states (figure 5.2). There are a number of effects and process occurring when a beam of X-rays impinges upon solid matter, resulting eventually in the attenuation of the beam intensity during its passage through the absorbing material. The absorption coefficient of the absorber, μ, may be defined from the intensity reduction caused by a given thickness of the material.

$$I = I_0 \exp(-\mu t) \tag{5.1}$$

where t is the thickness of the specimen and I_0 is the intensity at $t = 0$.

The mechanism of the absorption of photons in solids occurs when the energy of the X-ray exceeds the binding energy of a core level. Under these circumstances the photon is absorbed, exciting in the process an electron to an outgoing photo-electron wave.

5.2 Introduction to Photo-absorption

Photo-absorption is an excitation process characterised by the absorption of a high energy photon and consequently the excitation of an electron from its initial occupied state to a higher state. The generated photo-electron is governed by the energy of the absorbed photon. Accordingly, a core state electron whose wavefunction is very highly localized around the nucleus of a particular atom could be excited when high energy photons are used in X-ray photoemission spectroscopy (see figure 5.3a). On the other hand, a valence state electron is excited when lower energy photon is used in ultra-violet photoemission spectroscopy (figure 5.3b). The photo-electron ejected
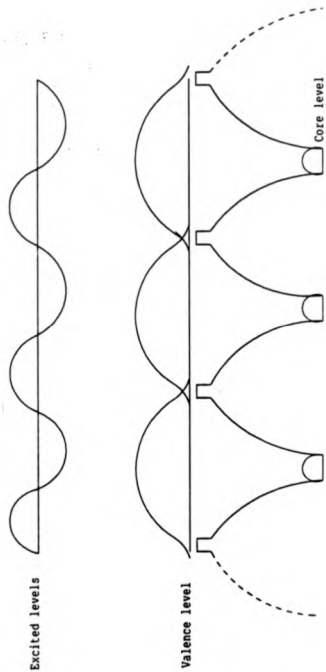
Excited levels

Valence level

Core level

Figure 5.2 Schematic diagram of the potential in a solid.

from the inner shells is governed by the energy conservation equation,

$$E = h\nu_0 - h\nu_a \tag{5.2}$$

where $h\nu_a$ is the binding energy of the (a) shell and $h\nu_0$ is the incident energy. Alternatively, in the photoabsorption process a high energy electron which lays in a high energy level may fill the hole left by the excited electron, emitting a photon as it does so (figure 5.3c). This process is known as fluorescence. The intensity of the emitted lines are hardly distinguished above the background of the X-ray photoemission spectroscopy. However, when a hole is left in the K-shell and then filled by an L-shell electron, the energy emitted in this transition may be lost to a nearby L-shell electron (figure 5.3d). This electron which is called an Auger electron, may lose its energy by collision or in a coulomb interaction process with an other electron, resulting in the creation of a second slow mono-energetic electron emission. As a consequence of this Auger process, the intensity of the X-ray emission lines are affected because of the transfer of the vacancy from one shell to another.

5.3   EXAFS and XANES

X-ray absorption edges carry fine structure which contains a variety of information. The extended X-ray absorption fine structure, EXAFS, appears in the high energy side above the edge in all forms of matter except in mono-atomic gases (see Brown and Winick 1980). This region could extend from 50 keV to up 1000 eV above the edge. EXAFS is due to the scattering of internally excited photo-electron waves by the atoms surrounding the ionised one.

The observed series of gentle oscillations in the EXAFS region are interpreted in
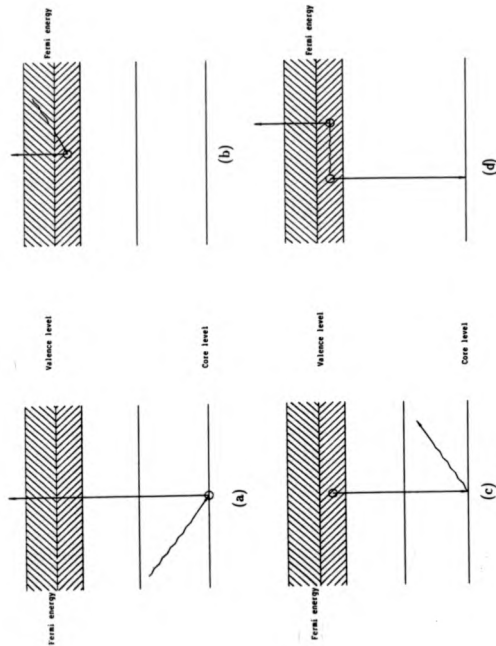
Figure 5.3 Schematic diagram for energy levels (a) core level transition, (b) valence band photoemission, (c) X-ray emission and (d) Auger transition.

terms of the scattering of the excited photo-electrons by the neighbouring atoms, (Lee et al 1981). The modulation of this series characterises the interference between excited photo-electron and photo-electrons scattered from neighboring atoms (see Durham et al 1983). Usual symbol for EXAFS

$$\chi(k) = \frac{\mu - \mu_0}{\mu_0} \tag{5.3}$$

where k is the wavevector characterising the ejected electron from an atom by means of the X-ray absorption (see Lee 1975 and Heald et al 1977) and μ and μ_0 are respectively, the absorption coefficients of an atom in the material and the absorption coefficient of the same atom in a free state, (Stern et al 1975, Ashley 1975). The study of EXAFS function may lead to important information about the material, (see Lee et al 1975). For instance. the distances between the absorber and the neighbouring atom are well established from the modulation of the cross section , (see Eisenberger et al 1980). Moreover. EXAFS gives information about the atomic arrangement of material as the X-ray diffraction does, (see De Crescenzi et al 1981). In some cases, the verification of postulated structure is also possible. This is achieved by changing the scatter identification to verify the proposed atomic type.

The X-ray absorption near edge structure (XANES) is defined to be covering the range from the edge up to 50 eV above the edge. The near edge structure is mostly related to the lowest unoccupied states in materials populated by the excited core electrons during the absorption process. The XANES region is distinguished from the EXAFS region by its higher cross section, governed by the appearance of a series of fairly narrow resonant peaks just above the edge, due to the strong scattering from

of fairly narrow resonant peaks just above the edge, due to the strong scattering from the neighbouring atoms (i.e. longer free paths of the photo-electrons are obtained), (see Lee et al 1975). Moreover, a stronger modulations are another feature of XANES (see figure 5.1). As a result, the interaction between the photo-electrons and the scattering atoms becomes weaker as the energy increases above the edge, therefore the theory of the multiple scattering is very significant in XANES, (see Durham et al 1981 and Durham et al 1982), whereas in EXAFS, single scattering is predominant. The introduction of multiple scattering in XANES has recently yielded a lot of geometrical information in a variety of substances (see Durham 1983).

In contrast with EXAFS, one of the rising interest in XANES is the possibility of extracting information about coordination geometry around the excited atom as well as bond angles which are not obtainable from EXAFS, (Bianconi 1980). Although these spectra are well known to be rich in chemical and structural information, it still very difficult to determine these features than would be from those rising from EXAFS.

5.4 Theory of magnetic XANES

5.4.1 Introduction

In principal, the treatment of the density of states may be applicable either by means of the electronic wavefunction as it has been the case for the momentum density, $n(\mathbf{p})$, for the Compton scattering, or by means of the Green's function. The two methods are equally applicable for disordered as well as ordered solids, however, in disordered alloys where the translational invariance is absent, it is believed that the

computation of the electronic wavefunctions is extremely complicated for a given atom. This is mainly due to the inhomogeneous density of states distribution at confident sites. This difficulty is overcome when Green's functions are applied because of their nature, i.e. the density of states is related to the imaginary part of the energy dependent average Green's function. As a result a comprehensive treatment of the theory is carried out by means of Green's functions.

The aim of this section is to give a detailed description of the theory of XANES in condensed matter systems, established in terms of one electron approximation, (see Durham et al 1984 and Muller et al 1983). A rigorous theory would have tackled the problem in terms of many-electron systems, mainly because the transition rate is basically dependent of the initial and the final states of many-electron systems. However, because of the difficulties of resolving the problem, it is much simpler to describe the system by means of one electron approximation, which represents the many-particle wavefunction as product of single particle wavefunctions. These wavefunctions are eigenfunctions of an effective one electron Hamiltonian. In brief, the system is described by the same Hamiltonian given in equation 1.13, which includes all the interacting terms occurring between photon and electron, relevant up to second order time dependent perturbation theory. However, since only terms linear in the vector potential $\mathbf{A}$ are responsible for absorption hence, only H'_2 and H'_3 are considered in the treatment of X-ray absorption (terms quadratic in $\mathbf{A}$ are responsible for high order scattering). In other words terms liner in $\mathbf{A}$ do not destroy photons.

$$H'_{2,3} = -\frac{e^2}{mc}\sum \mathbf{A}(\mathbf{r}_i).\mathbf{P} \underbrace{-\frac{e\hbar}{mc}\sum \mathbf{s}_j.\nabla \times \mathbf{A}(\mathbf{r}_i)}_{H'_3}. \tag{5.4}$$

The interacting Hamiltonian, $H'_{2,3}$, may be described differently elsewhere (see Durham et al 1984) in terms of current density of the ith electron at a position $\mathbf{r}$ i.e. $j_i(\mathbf{r})$.

$$H'_{2,3} = \frac{e}{c}\int d\mathbf{r} j_i(\mathbf{r})\mathbf{A}(\mathbf{r}), \tag{5.5}$$

where $j_i(\mathbf{r})$ is the current density.

$$j_i(\mathbf{r}) = \alpha_i \delta(\mathbf{R}_i - \mathbf{r}) \tag{5.6}$$

R_i being the position of the ith electron and α_i is the Dirac matrix which is linearly dependent upon the electron spin matrix (see Messiah 1981).

5.4.2 Transition rate

In order to describe the electron absorption and emission process it is very important to examine the absorption rate in detail by means of the transition probability that a photon is absorbed and consequently an electron is excited from its initial state. The transition probability of an excitation of a core electron from an initial state is characterised by a quantum state $|\alpha>$ which is an eigenstate for the uncoupled Hamiltonian (H_0) with energy E, to an unoccupied final state $|\beta>$ above the Fermi level. This transition probability is governed by the interacting Hamiltonian, $H'_{2,3}$.

First of all, assume that at a time $t = 0$ the system is comprised of an electron in the ground state $|\psi(t = 0)>$, plus an uncoupled photon in the state $|\mathbf{k}, \lambda>$, with wavevector $\mathbf{k}$, wavelength λ and polarisation vector $\epsilon_{\mathbf{k}}^{\lambda}$. At some much later time t,

the quantum system evolves to a state $|v(t)>$, according to the evolution operator, $U(t,t=0)$, which is related to the non-interacting Hamiltonian, H_0 (see appendix A). By postulating that the linear superposition of states is preserved in the course of time, therefore the correlation between the states $|v(0)>$ and $|v(t)>$ is linear and defined as,

$$|v(t)> = U(t, t = 0)|v(0)> \qquad (5.7)$$

where the evolution operator is given by,

$$U(t, t_1) = \exp[i H_0 (t - t_1)]. \qquad (5.8)$$

Assuming that the interaction occurs at the same time t. Hence, at some much later time, t_0, the system evolves to a state governed by,

$$|v(t_0)> = -i \int_0^{t_0} dt\, U(t_0, t) H'_{2,3} U(t, 0) |v(0)> . \qquad (5.9)$$

According to the final state, the probability that a photon is absorbed and therefore an electron is excited to a state $|v_n>$ is given by,

$$P_n(t_0) = | < v_n | v(t_0) > |^2. \qquad (5.10)$$

The states $|v_n>$ are obviously not observed, therefore, the summation over all those states is necessary,

$$P(t_0) = \sum_n P_n(t_0). \qquad (5.11)$$

Finally, the transition rate is defined as the transition probability per unit time, which is given by the familiar "Golden Rule" Durham (1984),

$$W = \frac{d}{dt_0} \{ \lim_{t_0 \to \infty} P(t_0) \} \qquad (5.12)$$

For our purpose the transition rate is going to be evaluated by means of Green's function. Economou (1979).

Substituting equation 5.9, 5.10 and 5.11 into 5.12 and using equation A14 in Appendix, one may obtain after Fourier transforming.

$$W = -2 \int_{-\infty}^{+\infty} d\mathbf{r} \int_{-\infty}^{+\infty} d\mathbf{r}' < \psi(\mathbf{r}) | H_{2,3}^* Im G^+(\mathbf{r},\mathbf{r}';E) H_{2,3}' | \psi(\mathbf{r}) > \tag{5.13}$$

where $H_{2,3}'$ is given in 1.33.

5.4.3 Atomic absorption within the multiple scattering theory

So far, a general expression for the transition probability has been deduced. Clearly the ambiguous point of this quantity consists of the calculation of the retarded Green's function, $G^+(\mathbf{r},\mathbf{r}';E)$, by means of multiple scattering theory, (Durham et al 1982 and Faulkner et al 1980). The retarded Green's function is due to be evaluated when $\mathbf{r}$ and $\mathbf{r}'$ lays within the muffin-tin potential, $V_i(\mathbf{r})$ i.e.

$$V(\mathbf{r}) = \begin{cases} V(\mathbf{r}) & if \ r \leq R_m \\ 0 & otherwise \end{cases} \tag{5.14}$$

where R_m is the muffin-tin radius which is chosen so that none of the atomic spheres overlap.

The one-electron Hamiltonian potential is a sum over lattice sites, $\mathbf{R}_l$.

$$V(\mathbf{r}) = \sum V_i(\mathbf{r} - \mathbf{R}_l). \tag{5.15}$$

Because of the complexcity of the derivation of the theory, only the important results are going to be given here. Accordingly the form of the retarded Green's

function is given by,

$$G^+(\mathbf{r}, \mathbf{r}'; E) = \sum_{lm, l'm'} Z_{lm}^i(\mathbf{r}_1, E).\tau_{lm, l'm'}^{ii} Z_{l'm'}^i(\mathbf{r}_1', E) - \sum_{lm} Z_{lm}^i(\mathbf{r}_<, E).J_{lm}^i(\mathbf{r}_>, E)$$

(5.16)

$Z_{lm}^i(\mathbf{r}_1, E)$ and $J_{lm}^i(\mathbf{r}, E)$ are real and known respectively as regular and irregular solutions of the radial Schroedinger equation. $\tau_{lm, l'm'}^{ii}$ is Complex quantity known as the scattering operator which describes the multiple scattering paths beginning in the state featured by the pair (l,m) of angular momentum quantum number at a site (i) and ending in different state (l', m') at the same site, (see Gyorffy et al 1973).

Since only the part describing the scattering path is complex,

$$ImG^+(\mathbf{r}, \mathbf{r}'; E) = \sum_{lm, l'm'} Z_{lm, l'm'}^2(\mathbf{r}, E).Im\tau_{lm, l'm'}^{ii}(E).$$ (5.17)

The local density of states for the atom at the origin is given by,

$$\rho^0(E) = -\frac{2}{\pi} \int_{cell} ImG^+(\mathbf{r}, \mathbf{r}'; E) d\mathbf{r}$$ (5.18)

where the integral involves the cell occupied by the atom at the origin.

Using equation 5.18, one may obtain the decomposition into angular momenta,

$$\begin{aligned} \rho^0(E) &= \sum_{lm} \rho_{lm}^0(E) \\ &= \sum_{lm} -\frac{2}{\pi} \int_{cell} d\mathbf{r} Z_{lm}^2(\mathbf{r}, E) Im\tau_{lm, lm}^{ii}(E). \end{aligned}$$ (5.19)

Finally substituting 5.17 and 5.19 into 5.13, one may write the transition rate formula as.

$$W = \pi \sum_{lm} |M_{lm}(E)|^2 \rho_{lm}^0(E),$$ (5.20)

$M_{lm}(E)$ being the matrix element which may be considered as an atomic quantity as well, varying smoothly and very slowly with energy. Thus all the effects of the surrounding atoms are ~~contained~~ in the scattering operator.

$$M_{lm}(E) = \int d\mathbf{r} < c(\mathbf{r})|H''H'_{2,3}|\varphi(\mathbf{r}) > . \tag{5.21}$$

5.4.4 Spin dependent photoabsorption

The measurements of the energy dependent photoabsorption in XANES has recently been established to be a method of probing the local density of empty states immediately above the inner shell threshold, (Ebert et al 1988 and Suortti 1979). The unoccupied states which get populated in the absorption process are of a selected angular momentum due to the dipole selection rule, (Vanderlaan et al 1986),

$$|\Delta j| \leq 1$$
$$\Delta l = \pm 1$$
$$\Delta m = +1.$$

Recently the study of the spin dependent photoabsorption near edge structure, hence, the spin density of the unoccupied states, has been made possible with circularly polarised radiation. (see Fano 1969). Therefore the majority and the minority bands may be separated in ferromagnets by reversing the direction of the magnetisation density in the absorber, (see Schutz et al 1988). The absorption coefficient which is proportional to the absorption transition rate (equation 5.20) may be written as,

$$\mu \propto |M|^2 \rho(E). \tag{5.22}$$

Because the matrix elements M vary smoothly and slowly with energy, one may assume accordingly that the matrix element is not influenced by photon-spin interaction. This assumption is considered valid for energies less than 100 keV (Pauli et al 1975). Moreover, the matrix is not sensitive to the spin orbit splitting in the core state and the final state (see Fano 1969). Hence, the density of the final state, $\rho(E)$, may be expressed as the sum of the density of states with spin up, $\rho^\uparrow$, and the density of states with spin down, $\rho^\downarrow$, which they describe respectively the majority and minority bands of the empty states.

$$\rho = \rho^\uparrow + \rho^\downarrow \tag{5.23}$$

Moreover the total number of photo-electrons transferred (n) is comprised of electrons with spin up, $n^\uparrow$, and electrons with spin down, $n^\downarrow$ (i.e. photo-electron with spin parallel and anti-parallel respectively to the photon spin).

$$n = n^\uparrow + n^\downarrow \tag{5.24}$$

Using equations 5.22, 5.23 and 5.24, the absorption coefficient may be expressed as the sum of two parts: spin independent term, μ_0, and spin dependent term which involves the spin of the photo-electron, P, and the density of states $\Delta\rho$.

$$\mu \propto \underbrace{|M|^2\rho}_{\mu_0} + \underbrace{|M|^2 P_e \Delta\rho}_{\mu_s} \tag{5.25}$$

where,

$$\Delta\rho = \rho^\uparrow - \rho^\downarrow. \tag{5.26}$$

The spin polarisation of the photo-electron is due to the photon spin polarisation transfer by means of the spin-orbit interaction,

$$P_e = \frac{n^\uparrow - n^\downarrow}{n^\uparrow + n^\downarrow} \tag{5.27}$$

Finally, the spin dependent absorption profile is possibly investigated in a difference experiment for which the ratio of the spin dependent photoabsorption coefficient $\frac{\Delta\mu}{\mu}$ is expressed as,

$$\begin{aligned}
\frac{\Delta\mu}{\mu} &= \frac{\mu^{\uparrow} - \mu^{\downarrow}}{\mu^{\uparrow} + \mu^{\downarrow}} \\
&= P_z \frac{\Delta\rho}{\rho}.
\end{aligned} \tag{5.28}$$

Chapter 6

MAGNETIC XANES IN IRON AND NICKEL

6.1 Introduction to magnetic X-ray absorption

The existence of spin dependent photoabsorption in magnetic atoms immediately above the Fermi energy may originate from the promotion of polarised photo-electrons from a lower unpolarised initial state to an empty final state characterised by its spin-split, immediately above the Fermi energy. Principally, the polarisation of photo-electrons may be created by a transfer from a photon polarisation in the direction of the incident photon wavevector, **k**, due to the influence of the spin-orbit interactions on the dipole matrix (see Fano 1969). The polarisation of photo-electrons excited by a circularly polarised radiation may extend up to few tens of electron-Volts above the edge.

The method applied for the observation of the spin dependent K-photoabsorption is established when circularly polarised photon interacts with unpolarised 1s electrons. The 1s electrons are promoted to higher unoccupied states, $(P_{\frac{1}{2}}, P_{\frac{3}{2}})$, which are governed by their different spin orbit splitting.

The estimation of the degree of circular polarisation was based upon the calculation of the degree of circular polarisation of the SRS synchrotron radiation emitted from line 7.6 which was accurately calculated by Laundy (1990). The calculation was based on the high brightness magnet lattice emittance.

In contrast with the Compton scattering experiment, the evaluation of the degree of circular polarisation of the incident beam must be accurately known for the spin dependent photoabsorption experiment in order to be able to estimate the magnetic effect because there is no normalisation criterion. Accordingly, the degree of the circular polarisation in the monochromatic beam was corrected after being diminished due to the Bragg reflection. The polarisation obtained after two Bragg reflections may be approximated for a perfect crystal as.

$$P_C' = \left(\frac{2cos2\theta}{1 + cos2\theta} \right)^2 P_C. \tag{6.1}$$

where P_C is the polarisation of the collimated white beam and θ is the Bragg angle (see Zachariasen 1967).

Since the stability of the beam was thoroughly controlled during each run, the only significant uncertainty associated with the value of the degree of circular polarisation results from the vertical width of the beam (0.5mm) and the crystal imperfections. The value of P_C was taken as the average value within the finite width of the beam and its uncertainty was estimated at 15%.

6.2 Previous research

The measurement of the spin dependent photoabsorption was recently introduced as a new method of studying magnetism in ferromagnetic materials (see Schutz et al 1987). A series of measurements were carried out at the L-edge of ferromagnetic Gd and Tb metals (see Schutz et al 1988). Later on, Schutz et al (1989a) reported for the first time the measurement of the spin dependent photoabsorption effect at the Gd L-edge in gadolinium metal and $Gd_3Fe_5O_{12}$ using circularly polarised radiation. Recently the spin dependent photo-absorption effect of the Fe K-edge and Pt $L_{2,3}$-edges in ferromagnetic alloy $Fe_{80}Pt_{20}$ were measured. Large relative spin dependent absorption coefficient (μ_s/μ_0) were obtained (i.e. 23% at the Pt L_2-edge and -12% at the Pt L_3-edge) (see Schutz et al 1989b) The measurements were made using the inclined view method at the synchrotron radiation facilities HASYLAB in Hamburg (DORIS) which operates at an electron energy of 3.7 GeV with a maximum current of 100mA and a typical life time of the order of 3 to 4 hours. Two photon beams were symmetrically collimated with respect to the orbital plane of the synchrotron radiation in order to obtain simultaneously partially circular polarised beams with opposite signs. A degree of $P_c=0.8$ for each beam was obtained. The beams were monochromated according to the double crystal monochromator (Si-311) which has an energy resolution of around 1eV at the region immediately above the Gd-edge. The intensities of the beams were monitored by means of two identical double ionisation chambers mounted in front and behind the magnetised absorber. In addition, the magnetic field in the absorber was reversed every second in order to ensure that the data could not be affected by the source

decay. The data obtained from the two beams were added together to improve the statistical accuracy

The spin dependent photoabsorption effects in transition metals were also measured (see Schutz 1989). The Fe K-edge profile was characterised by a positive effect immediately above the edge followed by a negative effect away from the edge. However, the effects in Ni and Co were found to be completely negative. A theoretical calculation based on the relativistic spin polarised multiple scattering theory described in the previous chapter, has been recently carried out by Ebert et al (1988), employing the self consistent potential, tabulated by Moruzzi et al (1978). The employment of a spin up and a spin down potential for the 1s core states in transition metals was necessary for the evaluation of the core wave functions.

6.3 Apparatus

The experimental assembly adopted for the spin dependent photoabsorption is shown schematically in figure 6.1. Principally, the apparatus employed was designed for spin dependent Compton scattering experiments. The spectrometer was mounted on a vertically adjustable baseplate, principally required for the magnetic photoabsorption experiment to select the beam polarisation above and below the orbital plane of the synchrotron radiation. A circularly polarised white beam may be collimated using adjustable tungsten slits positioned immediately in front of the crystal monochromator.

A tunable channel-cut monochromator was necessary to scan over a range of energy from 10eV up to 200eV immediately above the K-absorption edge in iron and
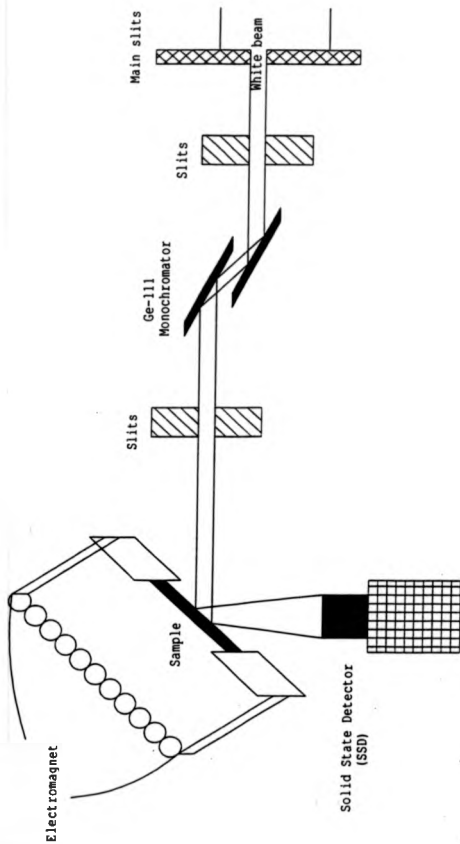
Figure 6.1 Schematic diagram of the experimental arrangement for the measurements of the spin dependent photoabsorption.

nickel. One of the major advantages of this kind of monochromator is emphasised in obtaining monochromatic beam parallel to the original white beam, therefore no further arrangements for beam alignment are necessary during an energy scan. Moreover, it provides rapid tunability over a broad spectral range, high transmission, narrow bandwidth ($\Delta E/E \sim 10^{-4}$ with perfect Si crystals). Accordingly, a vertically dispersing Si-111 channel cut monochromator, which was principally designed to operate over photon energy range of around 3-12 keV, was chosen in preference to a Si-311 mainly because of the higher reflectivity obtained from the 111 reflection. Moreover, the choice was also made because polarisation reduction is dramatically affected by the 311 Bragg reflection. For instance, for Si-311, $P_C = 0.90 \mp 0.1$ becomes $P_C' = 0.25 \mp 0.1$ after two reflections as quoted by Schutz et al (1988), whereas for Si-111, $P_C = 0.60 \mp 0.1$ becomes $P_C' = 0.45 \mp 0.1$ after two reflections.

The monochromator was mounted separately on a goniometer which formed part of an existing double crystal spectrometer in the experimental station. The monochromator height position had to be adjusted separately for the sample and detector which were both mounted on the same vertically adjustable baseplate. Although the energy scan over the region of interest was easily controlled using the SRS computer system, the adjustment of the monochromator and the alignment of the beam at the right height above and below the orbital plane of the synchrotron radiation was awkwardly achieved.

A second set of tungsten slits positioned just behind the crystal was necessary to stop radiation from the different Bragg reflections as well as radiation escaping straight through the gap in the crystal monochromator. The selected polarised monochromatic beam may be scattered from a fully magnetised foil through an an-

gle approximately equivalent to $\frac{\pi}{2}$ in order to monitor the fluorescence and maximise the scattering. The same solid state detector described in section 2.2.2 was used here, and it was calibrated with a low activity ^{133}Ba source. Moreover the transmitted radiation may be monitored with an ionisation chamber positioned behind the absorber and facing the incident beam. The Fe data were recorded with the old computerised MCA, whereas the Ni data were recorded with a Canberra Packcard Multi-Channel analyser (MCA) used previously in the Compton scattering experiments.

6.4 Experimental details

A new technique for the study of magnetic photoabsorption in ferromagnetic material was adopted for the first time. The method consists of measuring the difference in intensity of the fluorescence profile obtained from a magnetised ferromagnetic sample respectively for right- and left-hand circularly polarised radiation. The same investigation was carried out previously by means of the measurement of the modulation amplitude of the radiation transmitted through a magnetised ferromagnet using the inclined view method to extract circularly polarised synchrotron radiation.

The experimental measurements were similar to those reported for the spin dependent Compton scattering. Two spectra corresponding to opposite electron spin polarisation were recorded separately and the difference spectrum was then obtained. The measurement technique reported earlier, (see Collins et al 1989) was performed at the Daresbury storage ring at the X-ray topography station using the inclined view method. The station is situated some 80m away from the 1.2 Tesla dipole

magnet tangent point. The maximum current for which the ring was operating was around 280mA with a typical life time of around 30 hours. The emitted radiation is characterised by its critical wavelength, $3.88\mathring{A}$ (i.e a corresponding energy of 3.2 keV). Clearly from figure 3.2 the region including the K-absorption edge of transition metals is well within the energy spectrum of the synchrotron radiation.

The optimum magnetic signal measured for the Wiggler line (see chapter 3) is unfortunately not applicable for this particular line. However, as it has been mentioned in section 3.11, the prediction of the optimum magnetic signal for the dipole bending magnet at the 7.6 line may be accurately estimated according to the calculation performed by Laundy (1990). Accordingly the beam was selected with a minimum inclination of 0.125 mrads (i.e. 10mm above the orbital plane at the experimental station) to obtain a circularly polarised beam with $P_C = 0.7$. In contrast with the measurements reported by Schütz (1989), where two data sets could not be recorded simultaneously and symmetrically below and above the orbital plane of the synchrotron radiation but that was deemed to be unnecessary, mainly because the better positional stability of the beam is a routine operation of this storage ring. Typical synchrotron radiation beam movements were experienced in previous experiments (see figure 3.9)

The one $1\mu m$ thick foil was mounted between the electromagnet pole pieces to make an angle of around 35° to the incident beam. This was chosen to maximise the ratio ($signal/noise \propto cos\theta\sqrt{sin\theta}$. Similarly as in the Compton scattering experiment, the magnetic field in the sample was reversed every 5 minutes in order to minimise the effect due to source decay. The spin-up and the spin-down data are accumulated and stored separately in different memory locations. Since this kind of

experiment deals with the measurement of the integrated counts over the region of interest (i.e. the resolution of the detector is not significant), the solid state detector was positioned as close as possible to the foil in order to enlarge significantly the solid angle and therefore increasing the signal level. The resolution of the monochromator was assumed to be negligible. Despite this arrangement, the statistical accuracy of this scattering experiment was worse than that obtained from the transmission flux modulation performed by Schütz (1989); firstly because of a limited beam time and secondly because the integrated count rate obtained, immediately above the edge, from the transmitted radiation is almost twice as much as that obtained in the scattering experiment (i.e. $10^4/s$ integrated counts were obtained for the ion chamber compared to $5 \times 10^3/s$ obtained for the SSD)

A series of measurements were made for different energies immediately above the K-absorption edge of Fe and Ni. The measurements were made possible by tuning the monochromator marginally in order to increase the corresponding Bragg angle. Each of the measurements lasted one hour for energies above the edge, where the count rate is very high; typically $10^4/s$. However, in order to obtain the same statistical accuracy the measurements were recorded for as long as four hours at energies on the edge as well as immediately below the edge. The reason for such a low count rate at those energies is due to the high photoabsorption within that range. Magnetic effects of around 0.4% and 0.1% were obtained immediately above the edge for Fe and Ni respectively.

As usual the beam position was checked between machine refills in order to adjust the position of the spectrometer if the beam orbital plane had moved (see figure 3.9). Moreover, short energy scans were done between every two runs in order to check

the energy calibration, i.e. the edge position obtained from the original set up must remain the same within 1 eV of the energy resolution of the collimation and the monochromator arrangement (figure 6.2).

As far as nickel is concerned, the data were re-measured twice due to discrepancies found in the spin dependent photoabsorption intensities. These were attributed to the effect of the magnetic field produced by the electromagnet which affected the semi-conductor detector positioned very close to the magnet. The origin of this significant effect was confirmed when a measurement of the spin dependent photoabsorption was carried out with no foil mounted between the magnet pole pieces (i.e. a magnetic effect was still obtained). This problem was later resolved by moving the detector about $5mm$ away from the magnet, and good data were obtained.

6.5 Data analysis

The spin dependent photoabsorption profile in the XANES region is reflected by the spin density distribution of the final states populated in the absorption process, $\frac{\Delta \rho}{\rho}$ which may be obtained from equation 5.3.

$$\frac{\Delta \rho}{\rho} = \frac{1}{P_e} \cdot \frac{\mu_s}{\mu_0} \qquad (6.2)$$

where μ_0 is obtained in separate measurements of the scattered intensity detected respectively with and without foil mounted between the electromagnet pole pieces. The spin dependent modulation of the photoabsorption (μ_s/μ) was obtained from the experimental and the calculated $(\frac{\Delta I}{I})$ using an iterative calculation method in order to include the sample absorption into consideration.
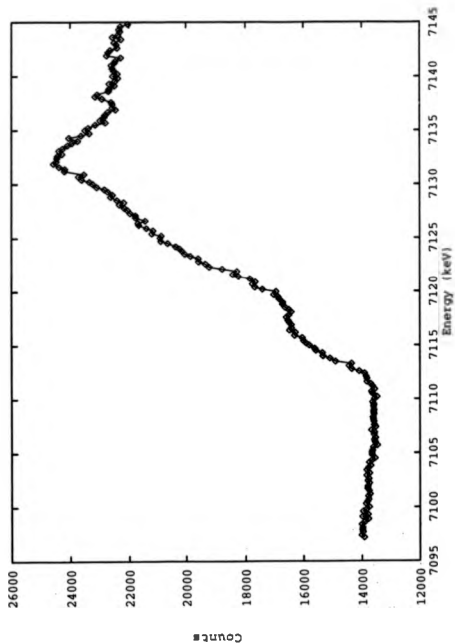
Figure 6.2 Schematic of the x-ray absorption edge in iron.

The intensity of a beam scattered in reflection from a sample of thickness t is given as,

$$I \propto I_0 \int_0^t e^{-\mu_1 t' \, cosec\alpha} \mu_K e^{-\mu_2 t' \, cosec\beta} dt' \tag{6.3}$$

where μ_1 and μ_2 are respectively the energy dependence absorption coefficients for the incident and the scattered beam, μ_K is the absorption coeficient at the K edge, α and β are the incident and the scattered angles described in figure 2.7.

The integrated intensity over the whole thickness of the absorber may be obtained as,

$$I \propto I_0 \mu_K \left[-\frac{e^{-\mu_1 t \, cosec\alpha} + e^{-\mu_2 t \, cosec\beta}}{\mu_1 \, cosec\alpha + \mu_2 \, cosec\beta} \right]_0^t \tag{6.4}$$

$$\propto I_0 \mu_K \left(\frac{1 - e^{-t(\mu_1 \, cosec\alpha + \mu_2 \, cosec\beta)}}{\mu_1 \, cosec\alpha + \mu_2 \, cosec\beta} \right). \tag{6.5}$$

The final processed data were normalised to the correct value of P_C taking into consideration that the circular polarisation dependence is given as $P_C' cos\alpha$, where α is the angle made between the incident and the scattered polarised beam and the photon spin direction.

6.6 Results and Discussion

The spin density distribution for iron and nickel, obtained from equation 5.2, are illustrated in figure 6.3 and 6.4. Originally the spin dependent photoabsorption effect of iron measured here with the scattering method was found to be twice as much as that measured by Schutz (1989) using the transmitted flux monitoring method. This discrepancy was later resolved after rescaling the transmission data using the correct value of the degree of circular polarisation ($P_C' = 0.25$), previously

Figure 6.3 The relative magnetic absorption rate in iron ($\Delta\mu/\mu$) plotted against the photo-electron energy (the zero energy correspond to the Fermi energy); (+) is corrected only for sample absorption and (•) is corrected for the finite P_C and sample absorption. The broken curve is from the first principles spin-polarised band calculation (from Ebert et al 1988).
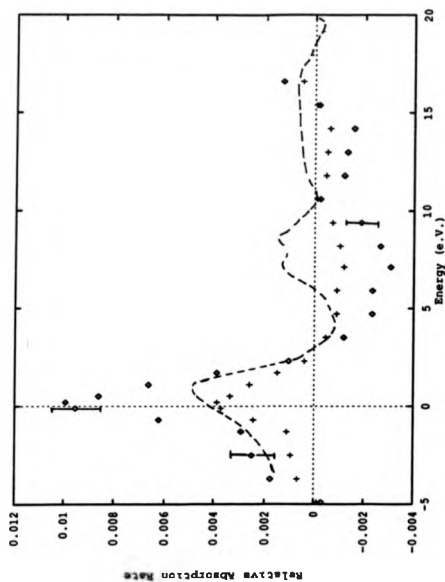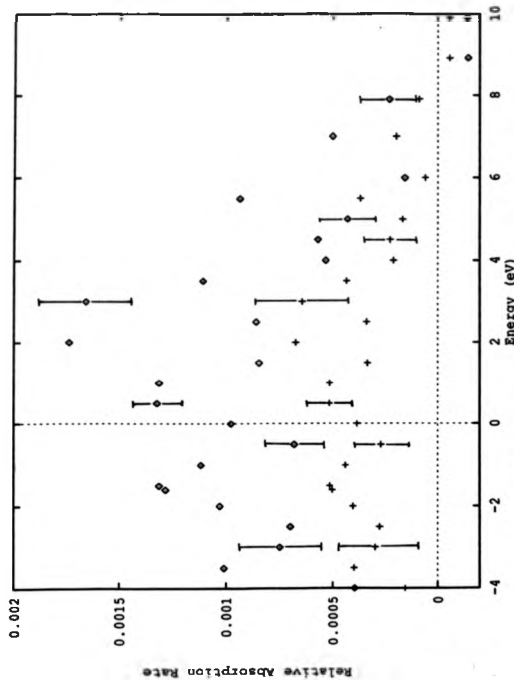
Figure 6.4 The relative magnetic absorption rate in nickel ($\Delta\mu/\mu$) plotted against the photo-electron energy (the zero energy correspond to the Fermi energy); (+) is corrected only for sample absorption and (◆) is corrected for the finite P_C and sample absorption.

mis-calculated by Schutz et al (1987) ($P_C^s = 0.42$), using equation 6.1.

After rescaling the transmission data, the agreement between the transmission data and the fluorescence data reported here is very good within the statistical accuracy and the estimated error of $P_C^s \sim 15\%$, which is mainly due to crystal imperfections and beam finite width. However, the good agreement between the theory and the experiment reported earlier by Ebert et al (1988) no longer exists due to the new correction.

Clearly from figure 6.3, there is a significant difference in the scale level of the spin dependent photoabsorption of iron between the theory and the fluorescent data. The peak obtained immediately above the edge in the spin dependent absorption data is twice as much as that predicted by the theory (i.e. the theory has underestimate the magnetic absorption rate in the calculation). Moreover, the second small broad positive peak predicted by the theory at around 10eV above the edge is not apparent either. It is clear from the figure that the spin dependent photoabsorption effect is concentrated immediately above the edge and extends to about 10 eV, with a maximum positive peak centred at around 2 eV ($\mu_s/\mu_0 \sim 1\%$) (i.e. majority spin states are obtained at the Fermi level followed by minority states). The distribution of the spin dependent density of states becomes negative at around 3.95 eV above the edge.

As far as nickel is concerned, the spin dependent photoabsorption behave quite differently from iron, i.e. the spin density profile features a broad negative distribution data from about -4eV below the edge to +4eV above the edge (only minority states are obtained). In contrast with the iron, the theory failed completely to predict the spin dependent photoabsorption in nickel. The theory reveals a positive

peak immediately above the edge followed by a long tail to about 10 eV (Ebert 1988, private communication).

The unsuccessful quantitative prediction of the theory may be attributed, as has been mentioned by Ebert et al (1988), firstly to the neglect of many-body effect, which could be significant, and secondly, the theory has not been averaged over the direction of the magnetisation because this could lead to a complete deterioration of the structure.

Chapter 7

CONCLUSIONS

7.1 Gamma-ray Compton scattering

The better understanding of Gamma-ray Compton profiles has become a routine operation. This kind of experiment may possibly have come to an end of an era unless higher energy sources such as ^{198}Au and ^{137}Cs are exploited in the goal to study heavy metals and alloys.

The gamma-ray Compton profile data of $Fe_{0.25}Ni_{0.75}$ which are obtained with the high energy source ^{198}Au have highlighted deficiencies in the calculations of the directional Compton profile. The discrepancies revealed at low momenta are directly related to the normalisation of core states. Hence, a rigorous calculation is needed particularly in the normalisation of core states in order to be able to make any real progress in the data interpretations. Furthermore, the data interpretation is also restricted by the relatively poor experimental resolution (i.e. 0.4 a.u. compared to 0.07 a.u. for the CuK_α X-ray focusing spectrometer (see Pattison et al 1981) and 0.08 a.u. for the S.R. (Photon Factory) focusing monochromator (see Itoh et

al 1989)). The interpretation of the momentum density is severely restricted by the poor experimental resolution, i.e. the Fermi surface will not be described accurately for resolution which represents a sizable fraction of the Brillouin zone. In order to obtain high resolution Itoh at al (1988) employed a double crystal monochromator, a curved crystal monochromator and a position sensitive detector which consists of imaging plates.

7.2 Magnetic Compton scattering and photo-absorption

The magnetic Compton scattering studies suffer similar problems as gamma-ray Compton scattering. In recent years the study of the total momentum density by means of the Gamma-ray Compton scattering technique has been overshadowed by the magnetic Compton scattering studies of the spin dependent momentum distribution with the synchrotron radiation. The radiation has made the study of magnetic X-ray experiments very successful and a critical test to band structure theories. The poor resolution obtained in the spin dependent Compton scattering ($\sim 0.7 a.u.$) and the poor statistical accuracy of the data were a major obstacle in the data interpretations particularly at low momenta where most interesting features are concentrated. Higher resolution data are really required in order to test the advanced FLAPW theory which has recently been introduced in the calculations of the spin dependent Compton profiles of ferromagnetic transition metals. Focusing monochromators may be very useful in the near future in the Compton scattering experiments. For such systems the count rate may be improved several times higher than what it is obtained in current experiments. Moreover the experimental reso-

lution may consequently be improved to match the detector resolution. One of the major advantages which arise from such systems is the use of very small samples. The spin dependent Compton data of gadolinium were very successful in describing the polarised conduction electrons. Recently Sakai el al (1990) measured the spin dependent Compton profile of gadolinium. A similar profile was reproduced with a better statistical accuracy.

Recently the magnetisation dependent electron momentum distribution raised a controversial point at the separation of spin and orbital contributions to the total magnetisation. It is well known that neutron scattering is sensitive to the total magnetisation density which can include contributions from both spin and orbital moments. However the separation of those two quantities is possible with photon scattering since they appear attached to different geometrical factors in the cross section. A close investigation of equation 1.32 confirms that the orbital term is always out of phase with respect to the charge scattering term whereas the spin term changes sign at some particular value of α (see figure 4.1). Hence the ratio L/S may be deduced by means of the Compton scattering technique. Recent experimental data carried out on Fe, Co and $HoFe_2$ (see Cooper et al 1991) have not supported fully the new formulation of the scattering cross section (see Lovesey et al 1991) which predicted the preservation of the orbital term for inelastic scattering governed by $\frac{\Delta E}{E} \ll 1$ (i.e. when $(\frac{E}{mc^2})^2 \ll 1$). This new formulation of the theory failed completely to predict the experiment particularly in the case of $HoFe_2$. Further clarifications regarding the theory are urgently required to solve this problem. For the same reason better quality data are also required in the near future.

As far as the spin dependent photoabsorption is concerned, the technique em-

ployed here has been very successful although it was very limited by the poor count rate with respect to the transmission experiment. Both methods present advantages and disadvantages, for instance the scattering method is not very accurate above the edge due to the Auger process; the intensity of the X-ray emission lines are affected because of the transfer of the vacancy created by the process from one shell to another. On the other hand the transmission method is not very accurate below the edge due to the different effects obtained in that particular region such as the Compton scattering and the anomalous scattering effects. Furthermore, in dilute systems the absorption obtained from the target atom is not very significant and therefore the signal-to-noise ratio is very low (i.e. the fluorescence method is a better experiment for investigating dilute systems).

Appendix A

The Green's function, $G(\mathbf{r}, \mathbf{r}'; z)$, is defined to be the solution of the following equation,

$$[z - L(\mathbf{r})]G(\mathbf{r}, \mathbf{r}', z) = \delta(\mathbf{r}' - \mathbf{r}) \tag{A.1}$$

$L(\mathbf{r})$ being the linear, hermitian, time dependent operator and z a complex variable.

Assume that $\{|\phi>\}$ is a complete set of eigenfunctions of the operator, L, corresponding to a set of eigenvalues (λ_n), i.e $L|\phi_n> = \lambda_n|\psi_n>$, then in the Dirac notation we have,

$$G(z) = \frac{1}{z - L}\sum_n |\phi_n><\phi_n| \tag{A.2}$$

Using the general relation valid for every function F, i.e.

$$F(L)|\psi_n> = F(\lambda_n)|\phi_n> \tag{A.3}$$

Green's functions may be evaluated as,

$$G(z) = \sum_n \frac{|\phi_n><\phi_n|}{z - \lambda_n} \tag{A.4}$$

Clearly from the equation A.4 that Green's function, $G(z)$, exhibits simple poles at the position of the eigenvalues of L and vise-versa. Hence, by assuming $(z = \lambda)$, where λ belongs to the continuous of the spectrum of L, the Green's functions becomes well defined in equation A.4. However, one may try to define $G(\lambda)$ by a limiting procedure,

which means that the eigenstates associated with the continuous spectrum are extended i.e.

$$G^{\pm}(\lambda) = \lim_{\epsilon \to 0^+} G(\lambda \pm i\epsilon) \tag{A.5}$$

where ϵ is positive and infinitesimal.

By substituting equation A.3 into equation A.4, it is straightforward to obtain the side limits,

$$G^{\pm}(\lambda) = \lim_{\epsilon \to 0^+} \sum_n \frac{|\phi_n > < \phi_n|}{\lambda - \lambda_n \pm i\epsilon} \tag{A.6}$$

$$= \sum_n |\phi_n > < \phi_n| \lim_{\epsilon \to 0^+} \frac{1}{\lambda - \lambda_n \pm i\epsilon} \tag{A.7}$$

Finally using Cauchy identity (Messiah (981),one may obtain.

$$G(\lambda) = \sum_n |\circ_n > < \phi_n| \{ \Theta(\frac{1}{\lambda - \lambda_n}) \pm i\pi\delta(\lambda - \lambda_n) \} \tag{A.8}$$

The first term in the right hand side of the last equation, which is known as the Cauchy identity (Messiah 1981). drops out in the difference expression,

$$\tilde{G}(\lambda)^{\pm} = G^+(\lambda) - G^-(\lambda)$$
$$= -i2\pi \sum_n |\phi_n > < \phi_n| \delta\lambda - \lambda_n \tag{A.9}$$

To describe the quantum system by means of the evolution operator, $U(t, t_0)$,it is necessary to make the following assumption; the system is assumed to be in certain dynamical state at time t_0, then evolves to a different state at a later time t.

As a preliminary, the Fourier transform of $\tilde{G}(\lambda)$ which is $\tilde{G}(\tau)$ where $\tau = t - t_0$ may be written as,

$$\tilde{G}(\tau) = \frac{1}{2\pi} \int_{-\infty}^{+\infty} \exp(-\lambda\tau)\tilde{G}(\lambda)d\lambda. \tag{A.10}$$

Substituting equation A.9 into A.10 one may obtain,

$$\tilde{G}(\tau) = i \int_{-\infty}^{+\infty} \sum_n \{\exp(-\lambda\tau)\delta(\lambda - \lambda_n)d\lambda|\psi_n > < \psi_n| \tag{A.11}$$

Taking into account that the quantity $G(\lambda)$ is different from zero only when $\lambda = \lambda_n$, therefore,

$$G(\tau) = i \sum_n \exp(-\lambda_n \tau) |\psi_n > < \psi_n| \tag{A.12}$$

Using the general relation given in equation A.3, one may obtain,

$$G(\tau) = i \exp(iL\tau) \tag{A.13}$$

Finally, the evolution operator may be expressed in terms of Green's function as,

$$
\begin{aligned}
U(\tau) &= \exp(-iL\tau) \\
&= i\bar{G}(\tau)
\end{aligned}
\tag{A.14}
$$

References:

Aikala, O. Phil. Mag. 33, 603 (1975).

Ashley, C.A. and Doniach, S. Phys. Rev. B11, 1279 (1975).

Bathow, G. Freytag, E. and Haensel, R. J. of Appl. Phys. 37, 3449 (1966).

Bhatt, G. Grotch, H. Kazes, E. and Owen. D.A. Phys. Rev. A28, 2195 (1983)

Bianconi, A. Appl. Surf. Sci. 6, 392 (1980).

Bianconi, A. In : EXAFS, ed. Bianconi. A.. Incoccia, L. and Stipcich, S., Berlin:
Springer-Verlag (1983).

Biggs, F. Mendelsohn, L.B. and Mann. J.B. Nucl. Atom. Data Tables 16, 201
(1975).

Blume, M.J. Appl. Phys. 57, 3615 (1985).

Blume, M.J. and Gibbs, D. Phys. Rev. B37. 1779 (1988).

Brahmia, A. Cooper, M.J Timms, D.N. Collins, S.P. Kane, P.P. and Laundy, D. J.
Phys.: Condens. Matter 1, 3879 (1988).

Winick, H. and Doniach, S. (New york plenum), ch.10 (1980).

Brunel, M. and De Bergevin, M. Acta. Cryst. A37. 324 (1981)

Brunel, M. Patrat, G. De Bergevin, M. Rousseaux, F. and Lemmonier, M. Acta.
Cryst. A39. 84 (1983)

Cardwell, D.A. Ph.D Thesis, University of Warwick, England (1987).

Codling, K. and Madden, R.P. Phys. Rev. Letts. 12, 106 (1964).

Collins, S.P. Cooper, M.J. Timms, D.N. Brahmia. A. Laundy, D. and Kane, P.P. J.
Phys. Condens. Matter 1, 9009 (1989).

Collins, S.P. Cooper, M.J. Brahmia, A. Laundy, D. and Pitkanen, T. J. Phys. Con-
dens. Matter 1, 323 (1989).

Collins, S.P. Laundy, . Brahmia. A. Jones, S. Timms, D.N. Cooper, M.J. Rollason, A.J. Nucl. Instrum. Methods A290, 254 (1990).

Collins, S.P. Cooper, M.J. Lovesey. S.W. and Laundy, D. J. Phys.: Condens. Matter 2, 6439 (1990).

Compton, A.H. Phys. Rev. 21. 483 (1923) and Phys. Rev. 22, 409 (1923).

Cooper, M.J., Leak, J.A. and Weiss, R.J. Phil. Mag. 12, 797 (1965).

Cooper, M.J. Pattison. P. Williams, B. and Pendey, K.C. Phil. Mag. 29, 1237 (1974).

Cooper, M.J. Pattison. P. and Schneider, J.R. Phil. Mag. 34, 213 (1976).

Cooper, M.J. Rep. Prog. Phys. 48, 415 (1985).

Cooper, M.J. Laundy. D. Cardwell, D.A. Timms, D.N. Holt. R.S. and Clark Phys. Rev. B34, 5984 (1986).

Cooper, M.J. Collins. S.P. Timms, D.N. Brahmia, A. Kane, P.P. Holt, R.S. and Laundy, D. Nature. Vol. 333. No. 6169, 151 (1988).

Cooper, M.J. Collins. S.P. Lovesey, S.W. Laundy, D. Timms, D.N. Physica Scripta. T35,103 (1991).

Corson, D.A. Phys. Rev. 86. 1052 (1952).

Coulson, C.A. and Duncanson. W.E. Proc. Camb. Phil. Soc. 37, 67 (1941).

Coulson, C.A. and Duncanson. W.E. Proc. Camb. Phil. Soc. 38, 100 (1942).

Danan, H. Herr, A. and Meyer. J.H. J. Appl. Phys. 39, 669 (1968).

De Bergevin, F. and Brunel. M. Phys. Letts A39, 141 (1972).

De Bergevin, F. and Brunel. M. Acta. Cryst. A37, 314 (1981).

De Crescenzi, M. Lapagno. L. Chiarello, G. Scarmozzino, R. Colavita, E. Rosei, R. and Mobilio, S. Sol. Stat. Commun. 40, 613 (1981).

Dirac, P.A.M. Proc. R. Soc. A111, 405 (1926).

DuMond, J.W.M. Phys. Rev. 33, 643 (1929).

DuMond, J.W.M. and Kirkpatrick, H.A. Phys. Rev. 52, 419 (1937).

Durham, P.J., J. Phys. F, 11, 2475 (1981).

Durham, P.J., Pendry, J.B. and Hodges, C.H., Comput. Phys. Commun. 25, 193 (1982).

Durham, P.J., In the Electronic Structure of Complex Systems, eds., Phariseau, P. and Temmerman, W.M. (Plenum press, New york) (1984).

Durham, P.J. In : EXAFS. ed. Bianconi, A., Incoccia, L. and Stipcich, S., Berlin : Springer-Verlag (1983).

Ebert, H. Strange, P. and Gyorffy. B.L. J. Appl. Phys. 63, 3055 (1988).

Ecomomou, E.N. Green's function in quantum physics, Berlin, New york: Springer-Verlag (1979).

Eggarter, E. and Eggarter, T.P. Phys. Rev. B15, 2804 (1977).

Eichler, J. and De Barros. S. Phys. Rev. A32, 789 (1985).

Eisenberger, P. and Reed. W.A. Phys. Rev. A5, 2085 (1972).

Eisenberger, P. and Reed. W.A. Phys. Rev. A9, 3237 (1974).

Eisenberger, P. and Lengeler, B. Phys. Rev. B22, 3551 (1980).

Eisenberger, P. Pltzman. P.M. and Winick, H. Phy. Rev. B13, 2377 (1976).

Elder, F.R. Gurewitsch, A.M. Langmuir R.V. and Pollack, H.D. Phys. Rev. 71, 829 (1947).

Fano. U. Phys. Rev. 178. 131 (1969).

Faulkner, J.S. and Stocks. G.M.. Phys. Rev. B21, 3222 (1980).

Faulkner, J.S. Prog. Mat. Sci. 27. 3 (1982).

Fock, V. Z. Phys. 98, 145 (1935).

Gell-Mann, M. and Goldberger M.L. Phys. Rev. 96, 1433 (1954).

Genoud, P. Singh, .K. J. Phys. Condens. Mat. 1, 5363 (1989).

Greaves, G.N. Durham, P.J. Quinn, P. and Diakun, G. Nature 294, 139 (1981).

Grobman, W.D. Eastman, D.E. and Freeouf, J.L. Phy. Rev. B12, 4405 (1975).

Grotch, H. Kazes, E. Bhatt. G. and Owen, D.A. Phys. Rev A27, 243 (1983).

Gyorffy, B.L. and Stott, M.J. in D.J. Fabian and L.M. Watson, Eds., Band Structure Spectroscopy of Metals and Alloys. Academic Press, London (1973).

Hasegawa, H. J. Phys. C14, 2793 (1981).

Heald, S.M. and Stern, E.A. Phys. Rev. B16, 5549 (1977).

Hodges, L. Ehrenreich, H. and Lang, N.D. Phys. Rev. 152, 505 (1966).

Holt, R.S. Cooper, M.J. and Leak. K.R. J. Phys. E. 11, 68 (1978).

Holt, R.S. Ph.D thesis, University of Warwick (1978).

Holt, R.S. Cooper, M.J. Dubard. J.L. Forsyth, J.B. Jones, T.L. and Knights, K. J. Phys. E. 39, 541 (1979).

Holt, R.S. and Cooper, M.J. Nucl. Instrum. and Meths. 213, 447 (1983).

Itoh, F. Sakurai, M. Sugawa. T. Susuki, K. Sakai, N. Ito, M. Moa, O. Shiotani, N. Tanaka, Y. Sakurai, Y. Nanao. S. Kawata, H. Amemiya, Y. and Ando, M. Rev. Sci. Instrum. 60, 2402 (1989).

Jackson, J.D. Classical Electrodynamics, Ch.14 New york Wiley 848 (1975).

Jauch, J.M. and Rohrlich, F. The theory of photons and electrons (Berlin: Springer-Verlag) (1955).

Kakahashi, Y. J. Mag. Mag. 37. 189 (1983).

Kappler, H. Ann. Phys., Lpz. 27. 129 (1936).

Kim, K.J. Nucl. Instr. and Meths. 219, 425 (1984).

Kim. K.J. In the X-ray Data Booklet, Lawrence Berkeley Laboratory California (1986). Klein, O. and Nishina. Y. Z. Phys. 52, 853 (1929).

Kubo, Y. and Asano, S. Phys. Rev. B42, 4431 (1990).

Kulipanov, G.N. Skrinskii, A.N. Sov. Phys. Usp. 20(7), 559 (1977).

Laundy, D. Nucl. Instrum. Methods A290, 248 (1990).

Lawrence, P.J. and Rossiter. P.L. J. Phys. F16, 543 (1986).

Lederer, C.M. Hollander, J.M. and Perlman, I. Table of isotopes 6th ed. wiley Publication, New york. (1967).

Lee, P.A. and Pendry. J.B. Phy. Rev. B11, 2795 (1975).

Lee, P.A., Citrin, P.H., Eisenberger. P. and Kincaid, B.M. (1981).

Lienard, A. L'Eclairage Elec. 16. 5 (1898).

Lipps. F.W. and Tolhoek. H.A. Physica, 20, 89 (1954) ibid 20, 395 (1954).

Lovesey, S.W. J. Phys. C20. 5625 (1987).

Lovesey, S.W. Portugal. Phys. 19. 81 (1988).

Lovesey, S.W. Physica Scripta 44. 51 (1991).

Manninen, S. and Paakkari, T. Phys. Fenn. 9, 129 (1974).

Manninen, S. Suortti. P. Cooper. M.J. Chomilier, J. and Loupias, G. Phys. Rev. B34, 8351 (1986).

McWeeny, R. and Coulson, C.A. Proc. Phys. Soc. A62, 509 (1949).

Messiah, A. Quantum Mechanics. Ch. XXI North-Holland, Amsterdam, (1981).

Mills, D.M. Phys. Rev. B36. 6178 (1987).

Mogensen, O. and Petersen. K. Phys. Lett. A30, 542 (1969).

Moon, R.M. Koehler. W.C. Cable. J.W. and Child. H.R. Phys. Rev. B5, 997-1015

(1972).

Moruzzi, V.L. Jarack, J.F. and Williams, A.R. calculated Electronic Properties of Metals Pergamon. New york (1978).

Muller, J.E. and Schaich, W.L., Phys. Rev. B27, 6489 (1983).

Munoz, M.C., Gyorffy, B.L. and Verhuyck, K. J. Phys. F: Metal Phys. 13. 1847 (1983).

Natoli. C.R. Kuntzler, F.W. Misemer, D.K. Doniach, S. Phys. Rev. A22, 1104 (1980).

Nigh, H.E. Legvold, S. and Speeding, F.H. Phys. Rev. 132. 1092-1097 (1963).

Paakkari, T. Manninen. S.O. and Berggren, K.F. Phys. Fenn. 10, 207 (1975).

Paatero, P. Manninen, S. and Paakkari, T. Phil. Mag. 30, 1281 (1974).

Pattison, P. Hansen, N. K. Schneider, J.R. Chem. Phys. 59. 231 (1981).

Pauli, H.C. and Raff, V. Comput. Phys. Comm. 9, 392 (1975).

Pellegreni, C. Ann. Rev. Nucl. Sci. 22, 1 (1972).

Philips, W.C. and Weiss. R.J. Phys. Rev. 120, 790 (1968).

Pinski, F.J. Staunton, J.B. Gyorffy, B.L. Johnson, D.D. and Stocks G.M. Phys. Rev. Lett. 56, 2096 (1986).

Platzman, P.M. and Tzoar. N. Phys. Rev. (1965).

Platzman. P.M. and Tzoar. N. Phys. Rev. B2, 3556 (1970).

Platzman, P.M. and Tzoar. N. J. Appl. Phys. 57, 3623 (1985).

Podolsky, B. and Pauling. L. Phys. Rev. 34, 109 (1929).

Poulter, J. and Staunton. J.B. J. Phys. F18, 1877 (1988).

Rennert, P. Carl, G. and Hergert, W. Phys. Stat. Sol. 120, 273 (1983).

Ribberfors, R. (a) Phys. Rev. B12, 2067 and (b) B12, 3136 (1975).

Roeland, L.W. et al. J. Phys. F5. No. 12, L233 (1975).

Rolason, A. Ph.D thesis, University of Warwick (1984).

Ross, P.A. and Kirkpatrick, H.A. Phys.Rev. 45, 223 (1934).

(1984).

Sakai, N. and Ono, K. Phys. Rev. Letts. 37, 351 (1976).

Sakai, N. and Ono, K. J. Phys. Soc. Japan 42, 770 (1977).

Sakai, N. Terashima. O. and Sekizawa, H. Nucl. Instr. and Meths. 221, 419 Sakai,

N. J. Phys. Soc. Japan 56, 2477 (1987).

Sakai, N. and Sekizawa, H. Phys. Rev. B36, 2164 (1987).

Sakai, N. Siotani, N. Itoh. F. Mao. O. Ito, M. Kawata. H. Amemiya, Y. and Ando,

M. J. Phys. Soc. Japan 58. 265 (1989).

Sakai, N. Siotani, N. Ito, M. Itoh. F. Kawata, H. Amemiya, Y. Ando, M. Yamamoto,

S. and Kitamura, H. Rev. Sci. Instrum. 60, 1666 (1989).

Sakai, N. Tanaka, Y. Itoh. F. Sakurai, H. Kawata. H. and Iwazumi, T. Photon Fac-

tory Activity Report. Proposal Number 90-228 (1990).

Schwinger, J.S. Phys. Rev. 75. 1912 (1949).

Schutz, G. Wagner. W. Wilhelm. W. Wagner, W. Kienle, P. Zeller, R. Frahm, R.

Materlik, G. Phys. Rev. Letts. 58. 737 (1987).

Schutz, G. Knulle, M. Wienke. R. Wilhelm, W. Wagner, W. Kieule, P. and Frahm,

R. Z. Phys. B. Condens. Matter (W.G) 1, 67 (1988).

Schutz, G. Frahm, R. Mautner. P. Wienke, R. Wagner, W. Wilhelm, W. Kienle, P.

(a) Phys. Rev. Letters 22.2620 (1989).

Schutz, Wienke, R. Wilhelm. W. Wagner, W. Frahm, R. and Kienle, P. (b) Physica

B 158, 284 (1989).

Schutz, G. Physica Scipta. T29. 172 (1989).

Slater, C. and Koster, G.F. Phys. Rev. 94, 1498 (1954).

Stark, R.W. and Falicov, L.M. Phys. Rev. Letts. 19, 795 (1967).

Staunton, J.B. Johnson, D.D. and Gyorffy, B.L. J. Appl. Phys. 61 (8), 3693 (1987).

Stenhaut, O.L. and Goodrich, R.G. Phys. Rev. B1, 4511 (1970).

Steinsvoll, O., Shirane. G., Nathan, R., Blume, M., Alperin, H.A. and Pickart, S.J. Phys. Rev. 161, 499 (1967).

Stern, E.A., Sayers, D.E. and Lytle, F.W. Phys. Rev. B11, 4836 (1975).

Sunderarajan, V. and Kanhere. D.G. (private communication) (1990).

Suortti, P. Phys. Stat. Sol. (b) 92. 259 (1979).

Tawil, R.A. and Callaway, J. Phys.Rev. A15, 1015 (1973).

Templeton, D.H. and Templeton. L.K. J.Appl. Cryst. 21, 151 (1988).

Timms, D.N. Brahmia. A. Collins. S. Collins, S.P. Cooper, M.J. Holt, R.S. Kane, P.P. Clark, G. Laundy. D. J. Phys. F 18, L57-L61 (1988).

Timms, D.N. Brahmia. A. Cooper. M.J. Collins, Hamouda, S. Laundy, D. Kilbourne, C. and Saint Lager, M.C. J. Phys. Condens. Matter 2, 3427 (1990).

Timms, D.N. Ph.D Thesis. University of Warwick (1989).

Tomboulian, D.H. US AEC NP- 5803 (1955).

Tomboulian, D.H. and Hartman. P.L. Phys. Rev. 102, 1423 (1956).

Trammel, G.T. Phys. Rev. 92. 1387 (1953).

Urbain, G. Weiss, P. and Trombe. F. Comptes Rendus, 200, 2132 (1935).

Vanderlaan, G. Thole. B.T. Sawatzky, G.A. Goedkoop, J.B. Fuggle, J.C. Esteva, J.M. Karnatak, R. Remeika. J.P. and dabkowska, H.A. Phy. Rev. B34, 6529 (1986).

Wakoh, S. and Kubo. Y. J. Magn. Magn. Mat. 5, 202 (1977).

Weiss, P. J. Phys. 6, 667 (1907).

Weyrich, W. Phy. Chem. 79. 1085 (1975).

Wheatly, J.C., Huiskamp, W.J., Diddens, A.N. Steenland, M.J. and Tolhoek, H.A. Physica, 21, 841 (1955).

Williams, B.G. (ed) Compton Scattering (New York: McGraw-Hill) (1977).

Wimmer, E. Krakauer, M. Weinert, M. and Freeman, A.J. Phys. Rev. B24, 864, (1981)

Winick, H. and Bienenstock. A. Annu. Rev. Nucl. Part. Sci. 28, 33 (1978).

Zachriasen, W. H. Theory of X-ray Diffraction in crystals, Dover Publications, New York (1967).